Surface-enhanced Raman scattering (SERS) for detection in immunoassays: applications, fundamentals, and optimization

by

Jeremy Daniel Driskell

A dissertation submitted to the graduate faculty

in partial fulfillment of the requirements for the degree of

DOCTOR OF PHILOSOPHY

Major: Analytical Chemistry

Program of Study Committee:
Marc D. Porter, Major Professor
R. S. Houk
Victor Shang-Yi Lin
Patricia A. Thiel
Surya Mallapragada

Iowa State University

Ames, Iowa

2006

Copyright © Jeremy Daniel Driskell, 2006. All rights reserved.

Graduate College
Iowa State University

This is to certify that the doctoral dissertation of

Jeremy Daniel Driskell

has met the dissertation requirements of Iowa State University

Marc D. Porter

Major Professor

For the Major Program

TABLE OF CONTENTS

ACKNOWLEDGEMENTS

This dissertation is a compilation of my successful work at Iowa State University that was only possible with the support of the many people in my life, and I would like to express my appreciation. First, I would like to thank Marc Porter for giving me the guidance to succeed and the freedom to grow. You have taught me so much, most notably, that this was about the journey not the finish line. I will try to remember these words of wisdom and apply them throughout my life. I want to express many thanks to Bob Lipert for always having an open door, for providing endless guidance and insight, for constant encouragement, and for sharing his brilliance. I would also like to thank Becky Staedtler for knowing, well, everything. You were always available to offer advice on all matters, and you were very much appreciated.

I would like to thank the many past and present members of the Porter Group. In particular I would like to acknowledge the Raman subgroup (Bob Lipert, Hye-Young Park, Jill Uhlenkamp, Betsy Yakes, and Deepak Dibya) for constructive criticism and helping generate ideas. Many thanks to Adam Bergren and Grant Edwards for some great discussions and heated debates on the outrageous ideas that didn't make it into this thesis, but nonetheless, helped me develop the critical thinking skills displayed in this thesis. I am especially grateful for the numerous mini-office meetings with colleagues, Rachel Millen and Karen Kwarta for some of the more practical research discussions which directly led to many of the results and explanations presented in this thesis. Additional thanks to Karen for playing such a special role in my life both as a colleague and even more importantly as a

friend. Your assistance throughout my academic career and our many conversations over coffee, research and otherwise, helped me succeed and maintain sanity.

I have had the unique opportunity of collaborating with two scientists at the National Animal Disease Center, Julia Ridpath and John Neill. I would like to thank them for helping build such a successful relationship that led to great research, for having the patience to teach an analytical chemist some biology, and for showing faith in our group by providing financial support. I would also like to thank Chris Schoen at Concurrent Analytical for providing us with many funding opportunities that supported much of this research.

Many thanks to my parents, Dan and Gerry Driskell, for their support in every sense of the word. No matter how far away I have been you are always there for me. Although cliché, one of the most important lessons you taught me, which certainly applied to this phase in my life, is to always give 100% because you only get out of life what you put into it. I must thank my brother, Blake, for keeping me in touch with and entertained by the outside world that I seemed to forget about from time to time. I would also like to thank the rest of my family at home, especially Danny and Susie Seib, for supporting me, understanding my long absence, and for sending me pictures (typically of good food and great times) to remind me of what I'm missing at home. Thanks also to my in-laws; Ken, Ann, Kelley, Meme, and Papa; for treating me as one of your own.

Finally, to my wife, Elizabeth, thank you for your unconditional love and support. Thank you for supporting my desire to attend Iowa State and following me. Thank you for sharing my enthusiasm when I came home with linear calibration curve and cheering me up when the nanoparticles "crashed"...again. You made this possible and life enjoyable. Thank you.

This work was performed at Ames Laboratory under Contract No. W-7405-Eng-82 with the U.S. Department of Energy. The United States Government has assigned the DOE Report number IS-T 2819 to this thesis.

IS-T 2819

CHAPTER 1. GENERAL INTRODUCTION

Dissertation Organization

Immunoassays have been utilized for the detection of biological analytes for several decades. Many formats and detection strategies have been explored, each having unique advantages and disadvantages. More recently, surface-enhanced Raman scattering (SERS) has been introduced as a readout method for immunoassays, and has shown great potential to meet many key analytical figures of merit. This technology is in its infancy and this dissertation explores the diversity of this method as well as the mechanism responsible for surface enhancement. Approaches to reduce assay times are also investigated. Implementing the knowledge gained from these studies will lead to a more sensitive immunoassay requiring less time than its predecessors.

This dissertation is organized into six sections. The first section includes a literature review of the previous work that led to this dissertation. A general overview of the different approaches to immunoassays is given, outlining the strengths and weaknesses of each. Included is a detailed review of binding kinetics, which is central for decreasing assay times. Next, the theoretical underpinnings of SERS is reviewed at its current level of understanding. Past work has argued that surface plasmon resonance (SPR) of the enhancing substrate influences the SERS signal; therefore, the SPR of the extrinsic Raman labels (ERLs) utilized in our SERS-based immunoassay is discussed.

Four original research chapters follow the Introduction, each presented as separate manuscripts. Chapter 2 modifies a SERS-based immunoassay previously developed in our group, extending it to the low-level detection of viral pathogens and demonstrating its versatility in terms of analyte type. Chapter 3 investigates the influence of ERL size, material composition, and separation distance between the ERLs and capture substrate on the SERS signal. This chapter links SPR with SERS enhancement factors and is consistent with many of the results from theoretical treatments of SPR and SERS. Chapter 4 introduces a novel method of reducing sample incubation time via capture substrate rotation. Moreover, this work led to a method of virus quantification without the use of standards. Chapter 5 extends the methodology developed in Chapter 4 to both the antigen and ERL labeling step to perform assays with improved analytical performance in less time than can be accomplished in diffusion controlled assays. This dissertation concludes with a general summary and speculates on the future of this exciting approach to carrying out immunoassays.

Literature Review

Traditional Immunoassays

Immunoassays are a class of analytical methodology that relies on the interaction of an antibody with its target antigen. This methodology was developed in the early 1960's for monitoring insulin,[1] and at that time its impact on the biological sciences was largely unappreciated. Breakthroughs in analytical readout technologies with improved sensitivity, coupled with immunoassay formats, facilitated the detection of lower levels of biochemically important molecules and led to significant clinical chemistry and medical discoveries. Today, immunoassays are routinely used in veterinary and human health diagnostic labs for early disease diagnosis and treatment in an effort to prevent the spread of contagious diseases and decrease the length of hospitalization.[2] Immunoassays have also been applied to food safety[3-5] and environmental analysis,[6-11] and have more recently been called upon to help fight the war against bioterrorism.[12] Further optimization of immunoassays in terms of sensitivity, specificity, speed, and throughput will likely generate more breakthroughs in all branches of science. Gaining further insights into fundamental and technical aspects of immunoassays has therefore been the focus of many research groups.

The antibody is the principal component in all immunoassays. Antibodies are proteins in the immunoglobulin (Ig) class, produced *in vivo* and can be further classified into the subgroups IgG, IgA, IgM, IgD, and IgE.[13, 14] All of the work presented in this dissertation employ IgG antibodies. Immunoglobulins are a special type of protein that possess binding sites specific for a target antigen. X-ray crystallographic studies suggest that the binding site of the antibody, or the paratope, is approximately 2 x 2 x 1 nm.[13] The specificity of the interaction between the binding site and the epitope, the portion of the antigen that is recognized by the paratope, results from complementary physical shape and charge. It has been estimated that >600 $Å^2$ of the epitope is buried in the paratope upon binding. Electrostatic, hydrophobic, hydrogen, and Van der Waals interactions stabilize the antibody-antigen complex at 15-22 amino acid points of contact on the antibody.[13] These forces lead to typical equilibrium constants for the reaction between the antibody and antigen to form the complex (i.e., antibody-antigen affinity constants) ranging from 10^7 to 10^{12} M^{-1}.[14] Collectively, it is the specificity of the antibody binding site and the strong affinity of the antibody-antigen complex that we exploit as analytical chemists.

In general, immunoassay formats can be divided into two categories, competitive and noncompetitive. Competitive immunoassays rely on the competition between a labeled analyte (i.e, tracer) and the sample analyte for a limited number of antibody binding sites.

After incubation, the concentration of the tracer (bound or free) is measured and related to the sample concentration. Noncompetitive immunoassays rely on an excess of antibody to effectively drive exhaustive binding of the analyte to the antibody-antigen complex. The complex is then quantified and related to antigen concentration. This complex is often measured with the use of a tracer (labeled secondary antibody) which binds to another epitope on the bound antigen. Each of these formats is illustrated in Figure 1.

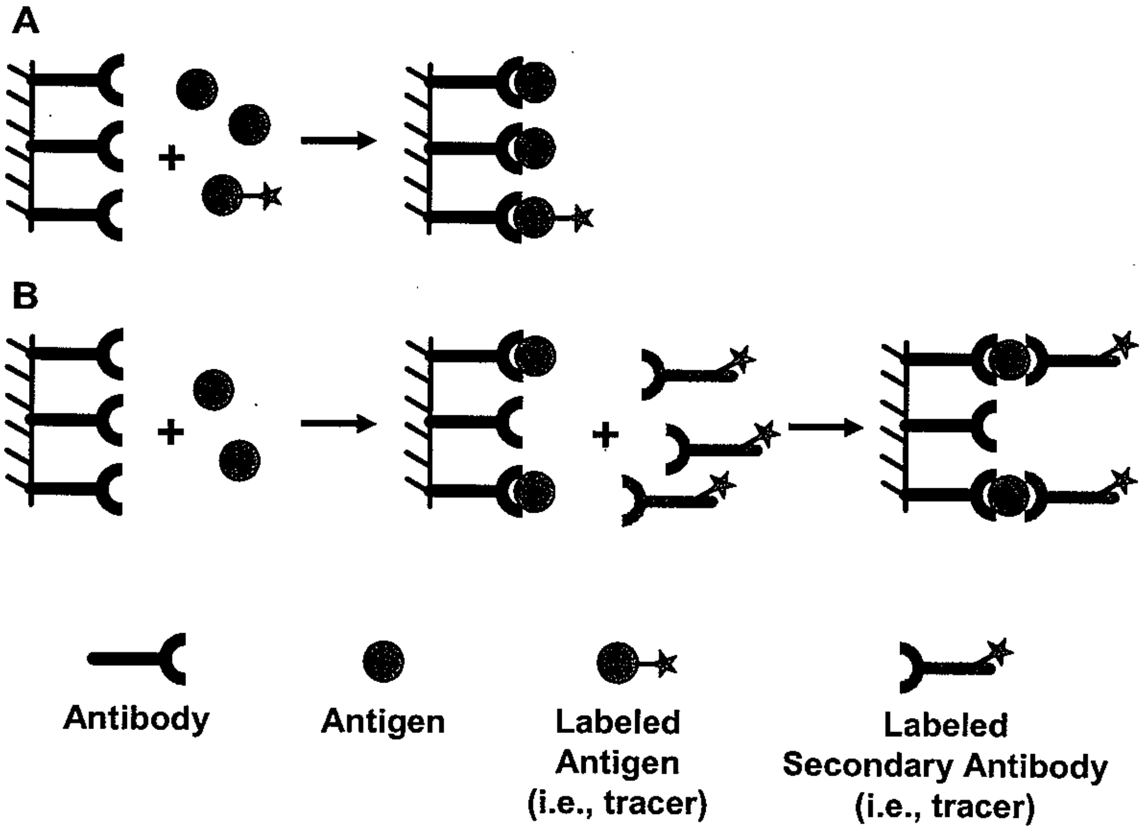

Figure 1. (A) Competitive and (B) Noncompetitive immunoassay formats.

Theoretical assessment of detection limits for each of the immunoassay configurations can be conducted using typical values for the immunocomplex binding affinity and other contributing parameters. The detection limit in a competitive immunoassay is governed by the affinity constant and the error in the measurement. This is because lower analyte concentrations result in greater tracer binding in a typical competitive assay, yielding higher signals. Thus, the brightness of the label is not a significant factor for the detection of low concentrations. It is the variation in this high signal that is important, as the signal uniformity increases, the ability to detect a small decrease in signal increases. Moreover, large binding affinity constants ensure that the analyte preferentially binds to the antibody over the tracer. Assuming the highest possible binding affinity ($K_a = 10^{12}$ M^{-1}) and a 1% variation in the blank signal, the detection limit in a competitive immunoassay is ~10^{-14} M.[13, 15]

The detection limit in a noncompetitive assay is controlled by not only the affinity constant and experimental error but also by the detectability of the tracer and nonspecific binding of the labeled secondary antibody. In this format, an analytical signal should only be obtained when analyte is present; thus, low levels of analyte yield low signals. Therefore, the drive to detect even lower levels an antigen continues to push the development of brighter labels. Nonspecific binding of a tracer to a capture antibody in the absence of analyte will trigger an undesirable response. If nonspecific binding occurs, the tracer can affect the detectable signal at low analyte concentrations and result in the inability to distinguish analyte generated signal (i.e., specific binding of the tracer to the analyte) from erroneous signal (i.e., nonspecific adsorption). Thus, higher analyte concentrations are required to generate a statistically significant signal from that of the background. A great deal of effort has been placed on decreasing nonspecific binding by the use of surfactants, to decrease nonspecific protein-protein interactions, and blocking agents, in the case of a solid phase immunoassay to reduce nonspecific tracer-solid phase interactions. Assuming a K_a of 10^{12} M^{-1}, a 1% deviation in the blank signal, and a 1% level of nonspecific binding, the detection limit can be two orders of magnitude lower than a competitive assay.[13, 15] Unlike a competitive assay, however, the noncompetitive assay can be improved with better secondary labels and a decrease in nonspecific binding.

Quantification of the immunocomplex in both the competitive and noncompetitive formats typically requires the separation of the antibody-antigen complex from labeled, unreacted antibodies in solution. Although it is possible for the immunoreaction to trigger a change in the signal of some tracers, thereby allowing separation-free quantification of the complex, this type of readout is less common.

A convenient method to separate free and bound reactants is to immobilize the bound form on a solid phase and wash away unreacted immunoreagents. Traditional solid phases for antibody or antigen immobilization include plastic microtiter plates, polymer beads, and membranes.[13] Immobilization to these substrates usually relies on hydrophobic or hydrophilic adsorption, although covalent attachment can be achieved with functionalized surfaces. A thorough list of traditional solid phases, modes of immobilization, and performance has been compiled by Diamandis and Chrostopoulos.[13]

Gold and glass substrates are among the more recent examples of substrates that serve as solid phases for immunoassays. Gold surfaces can be chemically modified by the spontaneous adsorption of thiols and disulfides.[16-18] The monolayer precursors are selected such that the functional moiety of the ω-terminus of the monolayer will react and covalently bind to antibody or antigen molecules.[19-24] Similarly, silanes can be used to modify glass surfaces to impart a particular functionality that will covalently bind proteins.[25-27]

Several readout methods have been developed to quantify the antibody-antigen immunocomplex after separation of the free and bound tracer. Established analytical labels for tracers include radioactive isotopes, enzymes, fluorophores, and chemiluminescent labels.[13, 14, 28-30] While these readout techniques have been extensively studied and have found routine use in immunoassays, each has unique strengths and weaknesses.

Radioactive isotopes were once the most heavily used label for tracers in immunoassays. Radioimmunoassays rely on the disintegration of unstable radioisotopes covalently grafted onto a tracer antibody or antigen. The counted radiation can be either a β–particle or a γ–ray, although γ-emitters are preferred due to greater activities and simpler instrumentation for detection. Further, radioactive decay is not affected by environmental factors such as pH or ionic strength and low radioactive backgrounds in biological matrices, which facilitate high sensitivity, led to the success of these assays. The most commonly employed isotopic label is the γ–emitter, ^{125}I. The use of other isotopes as labels has been explored in an effort to find isotopes which emit unique emission spectra. This development would allow the use of multiple labels to simultaneously detect multiple analytes; however, isotopic labels emit over a broad energy range. Thus, multi-analyte detection with distinctive isotopic labels always results in interference due to overlapping spectra.[31] Moreover, health hazards associated with radioisotope exposure has led to the diminished use of radioimmunoassays.[32, 33]

Enzymes were introduced in the 1970's as an alternative to radioisotope labels[34, 35] and currently rank as the most widely used label in immunoassays.[13] In an enzyme-linked immunosorbant assay (ELISA), the enzyme is conjugated to an antibody or antigen tracer, and following the immunoreaction and separation steps, a substrate which reacts with the enzyme is added to the reaction vessel. The product of the enzyme-substrate reaction is then quantified with a variety of methods, including visual assessment, colorimetry, fluorimetry, luminometry, and electrometry.[13, 14] In addition to the great flexibility in enzyme and readout choice, ELISA offers the advantage of high sensitivity due to the inherent amplification resulting from the high turnover rates of enzymes. Horseradish peroxidase and alkaline phosphatase are two of the most popular enzyme labels because of their high turnover numbers.

There are, however, some disadvantages with enzymatic labels. First, enzymes are large molecules with small diffusion coefficients. The large size translates to slow diffusion rates of the tracer and long sample incubation times are required. The macromolecular properties of the enzyme resemble those of antibodies which are favorable for adsorption to solid phases or sticking to the protein modified substrate. This propensity places enzymatic labels at a greater risk of nonspecifically binding to a solid phase than small molecule labels and can result in high backgrounds causing the limit of detection to suffer. Enzymes are also sensitive to environmental conditions such as pH, ionic strength, and temperature, which may alter their activity and this environmental dependence is typically an undesirable characteristic for a label. In some special cases the binding of an antigen to an enzyme-labeled antibody causes conformational changes in the enzyme, inhibiting its activity and serving as a basis for monitoring immunocomplexes without a separation step of the free and labeled reagents.[36]

Multiplexing is another challenge for enzyme-based assays. As described above, the enzyme-substrate products typically result in a color change or emitted radiation and are readout spectroscopically. The challenge is finding multiple enzyme-substrate systems that generate products without overlapping spectra for the simultaneous identification of multiple antigens.

Fluorescent and chemiluminescent labels were introduced and developed shortly after the breakthroughs with enzymes and are now commonly used in immunoassays due to the improved sensitivity of luminescence compared to spectrophotometric methods. Much like enzymes, fluorescent (e.g., fluoresceins, rhodamines, etc.) and chemiluminescent (e.g., luminol) labels are sensitive to their local environments and can be used to monitor the formation of the antibody-antigen complex without a separation step. These labels are also employed in solid phase immunoassays in which free label is washed away from the complexed label. The major shortcoming of fluorescence readout is interference from background signal from scattering and fluorescence of the sample, substrate, cuvette, or instrument hardware (i.e., lenses). Attempts to overcome this limitation with time-resolved fluorescence measurements and labels with long-lived fluorescence, such as lanthanide chelates, have proven successful.[28] Like the products from enzyme labels, the emission spectra from many fluorophores is broad. However, since the fluorophore is immobilized on the solid phase rather than free to diffuse in solution like enzyme-substrate products, spatial addressing of multiple antibodies allows the use of a single fluorescent label in a multiplexed assay. In this case, the location identifies the antigen, with the fluorescence intensity then functioning in quantitation. The challenges with this approach lie both in the high throughput microfabrication of many unique addresses and hardware to "read" each address.

Approaches to Improve Immunoassay Performance: Readout Techniques

Immunoassays must be improved to meet the ever increasing demands for greater sensitivity, lower detection levels, greater speed, and higher throughput sought by diagnostic laboratories and bioterrorism prevention agencies. Advancements in readout technologies and development of methods to increase the rate of antibody-antigen binding are central to meeting these challenges. Numerous novel readout techniques have been reported in the literature recently, including surface plasmon resonance,[37-42] quantum dots,[43-51] microcantilevers,[52-54] and surface-enhanced Raman scattering.[55-70] Each of these techniques is in its infancy but holds great potential for increasing throughput and improving sensitivity.

Surface plasmon resonance (SPR) is a technique that detects refractive index changes at a metal substrate surface and methods have been developed to successfully apply SPR to immunoassay readout. SPR is a surface-sensitive, label-free method of monitoring and quantifying the complexation of an immobilized antibody with its target analyte. Moreover, this technique can be employed to follow the formation of such complexes in real-time. SPR measurements can be configured in three ways, scanning angle, scanning wavelength, and imaging, all of which require monitoring the intensity of reflected light on a metal/dielectric interface.[37] Detectable limits of 10^{-9} to 10^{-13} M have been achieved with SPR readout, but the greatest benefits include real-time monitoring, increased throughput via imaging configurations, and reduced assay time with the elimination of a labeling step.[38] However, SPR measurements can be compromised by fluctuations in refractive index that arise from uncontrolled temperature variations or mismatches in sample and buffer refractive indexes in flowing solutions, both of which can be misleading with respect to the association or dissociation of the antibody-antigen complex.[71]

Quantum dots (QDs) have also been explored as an alternative to traditional organic dye labels used in luminescence-based immunoassays.[43-51] QDs are luminescent semiconductor nanocrystals, the most popular being zinc sulfide-capped cadmium selenide (CdSe-ZnS core-shell). QDs have been reported to have 20 times the intensity, 100 times the stability against photobleaching, and one-third the emission width of organic fluorophores such as rhodamine.[51] These attributes make QDs very attractive as labels in immunoassays. As an example, ZnS-CdSe core-shell QDs have been utilized for the detection of the food born pathogen, *Escherichia coli* O157:H7 (*E. coli*).[50] This assay resulted in a detectable range of 10^3 to 10^7 CFU/mL, 100 times better than the FITC fluorescence-based assay. The work of Hahn, et al., demonstrated the ultimate in sensitivity with the visualization of a single *E. coli* cell labeled with QDs.[49]

Another attraction of QDs stems from the ability to fine tune their emission spectra by changing the particle sizes, facilitating the production of many unique labels. Coupled with the narrow emission band of a QD, multiplexed assays have proven successful.[47] One of the challenges associated with the incorporation of QDs into assays is the lack of a universal method for coating QDs with protein.[47] QDs have an inherent hydrophobic nature that is imparted by capping agents used during synthesis and limits biocompatibility. Hydrophobicity reversal is achieved via cap exchange or amphiphilic encapsulation; however, issues related to stability against aggregation and reproducibility of QD-biomolecule ratios have been encountered. Efforts are being made to develop a universal protocol for bioconjugation that address these issues.[44-47]

Another promising label-free method of monitoring immunoreactions employs a functionalized microcantilever.[52-54] In this type of assay, the antibody is immobilized on a cantilever, and its oscillation frequency is monitored. The mass changes that results from antigen binding shifts the resonance frequency of the oscillating cantilever. The frequency shift is extremely sensitive to changes in mass and assay results have suggested that detection of a single baculovirus is possible.[54] The label-free nature and real-time monitoring capability, in addition to its sensitivity, make this an appealing technology. Moreover, advances in microfabrication will facilitate multiplexed detection with an array of uniquely modified microcantilevers. However, before this method receives widespread recognition, limitations such as irreproducible biorecognition coatings and long-term drift of cantilever bending must be overcome.[53]

Surface-enhanced Raman scattering, which is the subject of this dissertation, has recently been explored as a readout method for immunoassays on the basis of several intriguing attributes.[55-70] First, in contrast to normal Raman spectroscopy, SERS intensities have been shown to be comparable to those of fluorescence. Unlike fluorescence, however, Raman bands are much narrower (less than one nanometer half widths), reducing the likelihood of spectral overlap from multiple labels and facilitating simultaneous detection in a multiplexed assay without the need for addressing. Optimum excitation is also dictated by the enhancing substrate rather than the scattering molecule; thus, only a single excitation source is needed for multi-analyte detection. Raman scattering is also unaffected by its surrounding environment (e.g., pH, ionic strength, quenchers) resulting in a more stable and reproducible signal. Finally, Raman scatterers are photostable due to the extremely short liftetime of the excited state.

Several approaches have been taken to incorporate SERS into an immunoassay. The earliest work utilized a roughened silver capture antibody substrate to bind thyroid stimulating hormone.[60] In that work, the enhanced Raman signal of the label was monitored as a result of the enhancing substrate. Dou et al. developed an enzyme immunoassay in which the product of the enzyme-substrate reaction was Raman active.[59] The product was then adsorbed onto colloidal silver for SERS readout. The work of Zhang et al. successfully developed a label-free immunoassay relying on SERS for readout.[63] That work reported that the binding of calcium dipicolinate (CaDPA), a biomarker for bacillus spores, to a roughened silver substrate could be directly readout with the intrinsic scattering of CaDPA.

Our research laboratory has developed a new SERS-based immunoassay in a sandwich-type format which employs extrinsic Raman labels (ERLs).[56-58] ERLs are constructed by first coating a gold nanoparticle with a Raman reporter molecule. The gold colloid serves as an enhancing surface, while the Raman scatterer provides the signal for identification and quantification. Antibody is then covalently immobilized onto the modified nanoparticle to impart specificity. The resulting ERLs are used as tracers in a solid phase immunoassay.

This design has been successfully applied to the simultaneous, multiplexed detection of IgG protein[58] and the ultrasensitive detection of prostate specific antigen, a biomarker for prostate cancer.[57] Chapter 2 details this type of assay and demonstrates the universality of this approach and its ultra high sensitivity in an assay for the detection of feline calicivirus.

Approaches to Improve Immunoassay Performance: Increased Mass Transport

Research has also focused on immunoassay time reduction, but at a lower level of activity with respect to the quest for improvements in sensitivity. However, the improvement on assay speed is yet another key facet in the creation of highly effective immunoassays. It has been repeatedly shown that antibody-antigen recognition is extremely fast, and that the chief limitation arises from the mass transfer of antigen and/or label to the substrate.[72-76] Some experimental evidence for diffusion control of the immunoreaction include an observed: 1) decrease in the antibody-antigen binding rate with an increase in solution viscosity, 2) increase in the antibody-antigen binding rate with reaction mixture stirring, and 3) decrease in the antibody-antigen binding rate for an immobilized antibody compared to that of a solvated antibody in free solution.[72] These experimental findings have been supported by theoretical models describing solid phase immunoassay kinetics.[73, 74]

Drop application is the most common form of sample and label delivery to the sensing surface, and relies solely on diffusion for mass transport. This strategy translates into long assay times. Unfortunately, only a limited number of approaches have been explored to increase mass transport and capitalize on the rapid recognition rates of antibody-antigen coupling.[77-83] Two of the more promising methods include electric-field-driven assays[77, 78, 82, 83] and lateral-flow assays.[84-91] Electric-field driven assays take advantage of the charge on antigens and antibodies to attract them to a surface. The molecules can be manipulated electrophoretically through solution to specific locations in a microelectrode array[78, 82] or electroosmotically in microchannels.[83] This method has been utilized to perform assays with 1-min incubations steps; however, several parameters must be considered. For example, each molecule has a unique isoelectric point, and therefore a mobility that varies with pH. Moreover, transport will be influenced by the ionic strength of solution and size and shape of the microchanel.

Lateral-flow, or immunochromatographic, assays have received a great deal of attention and have already been incorporated into many commercial systems.[84-91] Lateral-flow assays employ a porous membrane, typically nitrocellulose, as a solid phase with a localized region of immbolized capture antibody. Capillary forces facilitate the flow of sample and label solutions through the membrane where the antigen and tracer are extracted and concentrated in the capture zone. This type of assay has been used to monitor drugs, toxins, hormones, proteins, and pathogens.[86] The popularity of this "dip-stick" configuration lies in its ease of use, speed, and portability. Despite the widespread use of this technology in the health care industry, it suffers from certain inadequacies. First, these assays are only semi-quantitative and signal saturation is common. Additionally, most lateral-flow assays are limited to single analyte detection; tests for multiple antigens must be run serially with individual test strips, which can require large sample volumes.

To overcome the mass transfer limitation of solid phase immunoassays and the weaknesses encountered by many of the newly developed methods to increase mass transport, Chapters 4 and 5 introduce rotation-induced flux. In these chapters, the capture substrate is controllably rotated to increase antigen and label flux to the capture surface, thereby reducing assay incubation times.

Theoretical Origins of Surface-Enhanced Raman Scattering

Raman spectroscopy is a vibrational spectroscopy involving the inelastic scattering of incident photons by a molecule.[92] The incident photon induces an oscillating dipole in the molecule which acts as a source of scattered radiation. Most of the scattering occurs at the same frequency as the incident source and is termed Rayleigh scattering. However, a finite probability exists that the molecule will accept energy, equal to that of a vibronic transition to a higher energy state, resulting in scattered radiation that is shifted in frequency from the incident frequency. It is worth noting that not all vibrations are Raman-active; only a vibration that results in a nonzero change in polarizability at the equilibrium position of the normal vibration is Raman active. Traditional Raman spectroscopy is inefficient and Raman intensities are only about 10^{-6} of the incident intensity. Even with extremely intense excitation sources (i.e., lasers) Raman spectroscopy is incapable of low-level detection for quantitative analysis.

In 1974, Fleishman and co-workers observed unexpectedly high Raman signal for pyridine adsorbed onto anodized silver electrodes.[93] At that time, this finding was attributed to a large number of adsorbates on the rough surface due to increased surface area. In 1977, work by Jeanmaire and Van Duyne[94] and Creighton and Albrecht[95] showed that observed intensities could not be explained by an increase in the number of adsorbates. This conclusion was the beginning of surface-enhanced Raman scattering (SERS).

Several more experiments immediately followed revealing experimental parameters that impact enhancement and they have been summarized by Schatz.[96] Key observations included the dependence of enhancement on surface preparation (i.e., roughness) and the dielectric property of the substrate (e.g., silver, gold, copper, etc.) while molecular identity was found to be less of a factor on enhancement. These experimental findings initiated several investigations into the theoretical underpinnings of the surface-enhancement mechanism.[96-111] To fully exploit SERS in analytical chemistry, enhancement must be optimized and this will only be realized through a complete comprehension of the enhancing mechanism.

While theoretical advances in the mechanistic underpinnings of SERS continue, there are still several shortfalls and conflicting models. It is, however, generally viewed that the enhancement arises from both electromagnetic and chemical interactions between the adsorbate and substrate. The chemical enhancement theory is perhaps more controversial, but is believed to be due to a resonant charge-transfer state between the adsorbate and substrate.[106, 107, 111] The electromagnetic theory, on the other hand, is consistent with the dependence of SERS on the roughness and dielectric properties of the substrate and attempts to explain enhancement due to changes in the localized field experienced by the adsorbate at the enhancing substrate surface. Of the two, the electromagnetic theory has been more thoroughly studied.[96-105, 108-110] Surface enhancement factors have been measured to be on the order of 10^6 to 10^8, with chemical enhancement responsible for factors of 10-100 and electromagnetic mechanisms contributing factors of 10^5 to 10^6. Because the electromagnetic mechanism is recognized as the most significant pathway for enhancement, the historical development of this theory is briefly presented.

The intensity of Raman scattering is proportional to the square of the electric field experienced by the scattering molecule. There are two explanations for an enhanced local electric field on a conductive surface: 1) image charge effects[99, 112, 113] and 2) excitation of surface plasmons.[96, 97, 101, 108, 110]

Image field theory was first developed by King et al.[112] and Efrima and Metiu[113] to explain SERS dependencies on the excitation source, dielectric constant of the adsorbate and surface, electrode potential, scattering angle, and polarization. Qualitatively, the incident radiation induces a dipole oscillation, μ_{ind}, in the adsorbate, which leads to an oscillating image dipole, μ_{image}, in the conductive surface just below the adsorbate. The image dipole has an electric field associated with it, E_{image}, which adds constructively to $E_{incident}$ to increase the overall field felt by the adsorbate. This model is depicted in Figure 2.

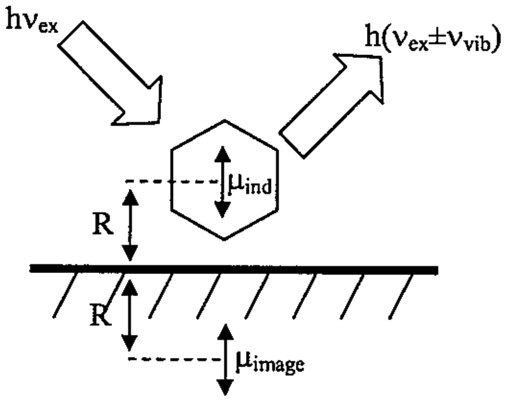

Figure 2. Illustration of the induced dipole, μ_{ind}, in an adsorbate and its image dipole, μ_{image}, formed in the metal substrate. The hexagon represents the adsorbate and R is the separation distance between the adsorbate and the metal surface.

A mathematical model for the image field theory was derived with the following assumptions: 1) the adsorbate is a point dipole, 2) dielectric constants are independent of the wavelength of $E_{incident}$, 3) a sharp surface boundary of electron density exists, and 4) chemisorption effects are negligible. Given these conditions, the SERS enhancement factor (*EF*) can be calculated by Equation 1[99]

$$EF = \frac{G}{\left[1 - \frac{\gamma\alpha_0}{4R^3}\right]^4} \qquad (1)$$

where G is a geometric factor based on incident angles and Fresnel coefficients, α_0 is the adsorbate polarizability, R is the adsorbate to image plane separation distance, and γ is given by Equation 2

$$\gamma = \frac{(\varepsilon_M - \varepsilon_A)}{(\varepsilon_M + \varepsilon_A)\varepsilon_A} \qquad (2)$$

where ε_M is the dielectric constant of the metal substrate and ε_A is the dielectric constant of the adsorbate. In general, G plays a rather insignificant role in determining the value of EF since its maximum value is 30 when the incident angle is optimized at ~60°. The value of R, α_0, and the dielectric functions contribute much more to the magnitude of EF. While the parameter α_0 and the dielectric functions can be accurately estimated, the value of R is largely uncertain because of unknown adsorbate-metal complex geometry and unknown location of μ_{ind} within the molecule. Therefore, a wide range of enhancement factors have been calculated (10^3-10^6) and this has led to conflicting views as to the contribution of the image field effect to the overall enhancement factor.

The local field experienced by the molecule can be raised dramatically by excitation of the surface plasmons of the enhancing substrate. When the incident light is resonant with the plasmon frequency, conduction electrons collectively oscillate, increasing the polarizability of the surface and the localized field. The influence of the surface plasmon on SERS enhancement was first described by Moskovits.[97] This initial rationalization has since been modified by Kerker et al,[101] Gersten and Nitzan,[102] Creighton,[108] and Schatz.[96] Of these works, the theoretical development by Schatz is the most advanced for an adsorbate on a metal spheroid and is briefly discussed below.

The derivation for calculations of the localized electric field at a surface began by defining a simple model system, which consists of a single metal spheroid that is small compared to the wavelength of incident light and is coated with adsorbate molecules. Maxwell's equations were evaluated at the incident frequency, ω, to calculate the electric field at the adsorbate at ω, $E(\omega)$. The electric field at the frequency of the Raman scattering mode can also be calculated by similar treatment but evaluated at the scattered frequency, ω'. Thus, the SERS enhancement factor is proportional to $[E(\omega)]^2[E(\omega')]^2$. By assuming that the spheroid is small in comparison to the wavelength of incident light and by ignoring image charge effects, Maxwell's equations can be replaced by the LaPlace equation, which is more easily solved.

Given these boundary conditions, and assuming an applied electric field E_0 along the major axis of a spheroid, the mean-square electric field at the spheroid surface is given by Equation 3

$$\left\langle \left| E^2 \right| \right\rangle = E_0^2 \left\{ \left| 1-\zeta \right|^2 + \frac{2\,\mathrm{Re}(1-\zeta)\zeta\eta^2}{Q_1(\zeta_0^2)\left(\xi_0^2-\eta^2\right)} + \frac{\zeta^2\eta^2}{Q_1(\xi_0)^2(\xi_0^2-1)\left(\xi_0^2-\eta^2\right)} \right\} \qquad (3)$$

where ζ is given by Equation 4

$$\zeta = \frac{(\varepsilon_i - \varepsilon_0)}{(\varepsilon_i + \chi\varepsilon_0)} \qquad (4)$$

In this case, ε_i is the dielectric constant inside the metal, ε_0 is the dielectric constant outside the metal, and χ varies from a value of 2 for a sphere to infinity for a rodlike surface asperity and is defined as

$$\chi = -1 + \frac{1}{Q_1(\xi_0)(\xi_0^2 - 1)} \qquad (5)$$

In Equations 3 and 5, ξ_0 is given by

$$\xi_0 = \frac{1}{\left(1 - \frac{a^2}{b^2}\right)^{1/2}} \qquad (6)$$

where $2a$ equals the minor axis and $2b$ is the major axis of the spheroid, and Q_1 is the Legendre function (Equation 7).

$$Q_1(\xi_0) = \left(\frac{1}{2}\xi_0\right)\ln\left(\frac{\xi_0+1}{\xi_0-1}\right) - 1 \qquad (7)$$

The spherical coordinate, η, in Equation 3 specifies location on the surface (e.g., $\eta = \pm 1$ at the spheroid tips) and relates to the polar angle θ.

$$\eta = \cos\theta\left[\frac{(\xi_o^2 - 1)}{\xi_0^2 - \cos^2\theta}\right]^{1/2} \qquad (8)$$

The electric field is greatest at the tips of the spheroid and has led to electromagnetic enhancement descriptions of the "lightning rod" effect.[103] That theory is somewhat misleading, however, because it only represents enhancement of a single adsorbate at the tip rather than the average enhancement provided by the particle over all locations on the surface. This distinction is a particularly important point for systems in which the surface of the particle is fully coated with adsorbates. Schatz developed a modified form of Equation 3 to consider the field over all η and determine the average field at the surface and the average SERS enhancement factor (Equation 9).[110]

$$\langle|E^2|\rangle = E_0^2\left\{|1-\zeta|^2 + \frac{2\,\mathrm{Re}(1-\zeta)\zeta}{Q_1(\xi_0)} + \frac{|\zeta|^2}{Q(\xi_0)(\xi_0^2-1)}\right\}\left(\frac{-(\xi_0^2-1)^{1/2} + \xi_0^2\sin^{-1}\left(\frac{1}{\xi_0}\right)}{(\xi_0^2-1)^{1/2} + \xi_0^2\sin^{-1}\left(\frac{1}{\xi_0}\right)}\right) \qquad (9)$$

The electric field at the surface in Equation 9 is maximized as ζ increases, or when $\mathrm{Re}(\varepsilon_i + \chi\varepsilon_0)$ approaches zero and $\mathrm{Im}(\varepsilon_i)$ is small. Assuming that ε_i can be described by the Drude expression, this situation occurs when the incident frequency matches the resonance frequency of the surface plasmon.[96] It should be noted that the plasmon resonance for a sphere is often defined as the condition in which the real component of the complex dielectric function is equal to -2 and the imaginary component is very small. This definition is consistent with that presented here given that $\chi = 2$ for a sphere and $\varepsilon_0 = 1$ for air.

A detailed analysis of these equations also suggests that the mean-square electric field is independent of the spheroid size for a fixed ratio of b/a. However, it is known experimentally that particle size is a factor, and this discrepancy is an inadequacy of the theory. The dielectric property of very small particles changes due to surface scattering,[114] while induced dipoles in large particles suffer from radiation damping[115] and dynamic depolarization effects.[116] Schatz presents modifications to Equation 9 to correct for all of these effects.

Surface scattering is a phenomenon which occurs when the particle size is smaller than the mean free path of the conduction electrons and electrons are scattered from the particle surface. As a consequence of surface scattering, the surface plasmon band broadens and damps out. The plasmon width can be quantifiably corrected by first invoking the Drude expression

$$\varepsilon_{free} = 1 - \frac{\omega_p^2}{\omega(\omega + i\gamma)} \qquad (10)$$

where ω_p is the bulk plasmon frequency and γ is the width of the plasmon resonance. For the case of a small particle, γ consists of both bulk and surface contributions and is given by

$$\gamma = \gamma_{bulk} + \frac{\upsilon_f}{L_{eff}} \qquad (11)$$

where υ_f is the Fermi velocity of the electrons and L_{eff} is the effective average scattering distance which is dependent upon particle shape. L_{eff} has been previously expressed in its entirety,[96] but reduces to $L_{eff} = a = b$ for a sphere and $L_{eff} = (16/3\pi)a$ for $b >> a$. For noble and alkali metals, surface scattering significantly modifies ε_{free}, and therefore the mean-square electric field, for spheroids smaller than ~20 nm.

For the case of a larger spheroid, radiation damping arises from secondary radiation from the induced dipole in the particle. The radiation emitted from different locations on the particle surface can also undergo destructive interference and is called dynamic depolarization. These effects can be quantified as a correction factor, D, that is used to rescale the induced dipole

$$D = \left(\frac{1}{1 - \frac{2}{3} i k^3 \alpha_0 - \frac{k^2 \alpha_0}{b}} \right) \qquad (12)$$

where

$$k = \frac{\varepsilon_0^{1/2} \omega}{c} \qquad (13)$$

and c is the speed of light. The k^3 term in Equation 12 corrects for radiation damping and the k^2 term corrects for dynamic depolarization effects. For spheroids smaller than ~1/10 of the wavelength of light, the dynamic depolarization term dominates while for larger particles radiation damping dominates; both effects cause the plasmon resonance to broaden and shift to longer wavelengths.

By substituting Equations 10 and 12 into Equation 9, the average electric field experienced by an adsorbate on a metal nanoparticle can be accurately described. The advances over earlier models include consideration of the particle dielectric constant, average field over the entire surface of the particle, surface scattering, radiation damping and dynamic depolarization effects.

It is important to remember that largest SERS enhancement occurs when $[E(\omega)]^2[E(\omega')]^2$ maximizes. Thus, the electric field at both the incident frequency and scattered frequency must be considered. Therefore, maximum SERS enhancement is obtained when the surface plasmon resonance frequency optimally couples to both the incident (ω) and scattered (ω') frequencies. Collectively, theory and experiments have provided compelling evidence that this situation occurs when the surface plasmon resonance peak is midway between the excitation and scattered frequency, provided that the plasmon resonance is Lorentzian shaped.[117-121] However, surface plasmon resonance may not be the only contributing factor to enhanced fields. High local fields in nanoparticle pores,[118] near sharp edges,[122-124] between coupled particles,[125-131] and between coupled particles and substrates[124, 126, 132-136] may contribute to surface enhancement in addition to the large fields provided by plasmon resonance. More studies are clearly necessary to further develop our understanding of the origin of SERS and this is the motivation for the work presented in Chapter 3.

Surface Plasmon Resonance

The previous section led to the important conclusion that the peak location of the surface plasmon resonance (SPR) of the enhancing substrate has a significant impact on the enhancement factor in a SERS experiment. Therefore, it is critical to understand the parameters influencing SPR so substrates can be designed and optimized for SERS enhancement through SPR manipulation.

The simplest SPR model is developed for a single isolated particle.[137] For particles smaller than the wavelength of incident light, all interactions are expected to be surface interactions and bulk properties are not observed. The electrons in these materials are then free to travel throughout the material and are subject to the influence of an electromagnetic field. At a particular frequency, an incident electric field causes a collective oscillation of the electrons in resonance with the field frequency, resulting in a standing wave. This resonance frequency is dependent upon particle size, shape, and the dielectric functions of the particle and surrounding medium. A convenient method of measuring the resonant excitation of the plasmon oscillation is absorption and scattering spectroscopy.[138]

Theoretical calculations of extinction spectra were first performed by Mie for spherical nanoparticles by solving Maxwell's equations and later developed to include ellipsoidal particles by Gan.[137, 139] Surface plasmon resonance can now be numerically calculated for any geometry using the discrete dipole approximation (DDA).[122] In the DDA method, a particle of any shape is represented as N polarizable points in a cubic lattice. The induced polarization of each point (P_i) is given by

$$P_i = \alpha_i \bullet E_{loc}(r_i) \qquad (14)$$

where α_i is the polarizability of the i^{th} element centered at r_i and $E_{loc}(r_i)$ is the local electric field at position i. It is important to note that $E_{loc}(r_i)$ is the sum of the incident field and all other dipoles in the particle. The induced polarization of each individual element is then considered to determine the overall induced polarization of the entire particle.

These models indicate that as particle size increases, the surface plasmon resonance is shifted to longer wavelengths. Calculations also reveal that as the spherical particle grows anisotropically to become rodlike, two SPR peaks are expected, one for traverse oscillation and the other for longitudinal oscillation. Moreover, an increase in the surrounding dielectric shifts the surface plasmon resonance to longer wavelengths. These models support the experimental findings.

The surface plasmon resonance is significantly shifted when two particles approach one another to within a few diameters.[138] This effect represents a coupling of the induced dipoles in each particle. A similar approach to the DDA method has been developed to model the polarizability of a nanoparticle dimer or cluster.[140] Like the DDA model, the polarization at a single point is calculated considering the incident electric field and the dipole fields of neighboring points. However, unlike the DDA model in which an individual particle is represented by several point dipoles, each point represents an individual particle in the aggregate. This model, consistent with experimental observations, reveals that coupling of particles results in a red shift and broadening of the SPR. This red shift in the SPR peak (i.e., color change) upon aggregation is the basis for many analytical applications, such as DNA hybridization-induced colloidal assembly.[141]

The SPR of a nanoparticle is also significantly affected when brought into close proximity of a flat metallic substrate. Much like the particle-particle coupling, an image of the induced particle dipole (and multipoles) is produced in the underlying conductive substrate. The coupling of the image dipole with the nanoparticle dipole results in a shift of the SPR to longer wavelengths. The SPR of this system has been modeled by Okamoto and Yamaguchi[142] using the polarizabilities tabulated with the methods of Aravind[143] and Wind.[144] This and related works have established experimentally and through modeling that the location of the SPR depends on the particle size, shape, spacing, and dielectric functions of the particle, underlying metal film, and ambient.[130, 136, 142, 145, 146] Understanding how variations in these parameters influence the SPR in this system is particularly important for optimization of a SERS-based analytical assay employing Raman-active nanoparticles as labels for analyte bound to a gold substrate. SPR calculations, as well as a detailed experimental investigation into this system, are presented in Chapter 3.

Models that underscore parameters influencing SPR, coupled with SERS theory that demonstrates the dependence of the enhancement factor on SPR, have led to a great deal of focus on developing SPR tunable substrates for optimized SERS measurements. Grating-type substrates[147] and metal coated SiO_2 posts,[148] as well as nanoparticle arrays fabricated via nanosphere[121, 131, 146, 149] and electron beam[120, 150] lithography have been utilized as SERS substrates. These fabrication techniques allow precise control over nanoparticle size, shape, and spacing, factors that can be used to manipulate the SPR. It is imperative that more research efforts, like those listed above and that presented in Chapter 3, be carried out to understand how to capitalize on the systematic control of SPR in order to increase SERS enhancement factors and to optimize the utility of a SERS-based analytical systems.

Dissertation Overview

Based on the themes introduced above, this dissertation describes the development, application, and optimization of a SERS-based solid phase immunoassay. Each of the following chapters is presented as individual manuscripts that investigate differing aspects of a SERS-based immunoassay, including universal application, surface enhancement origins, and assay time reduction. Chapter 2 begins with the extension of a previously developed concept for a SERS-based assay. Multiple buffers, ionic strengths, and concentrations were systematically studied to develop an immunoassay protocol that can be generically applied to a wide range of analytes simply by swapping antibodies. This approach is demonstrated by the detection of feline calicivirus, the first virus detected utilizing this concept. The basis for the surface enhancement mechanism in our assay is investigated in Chapter 3. In an effort to overcome mass transfer limitations that arise in solid phase immunoassays, the concept of a rotating capture substrate is introduced to increase solution flux to the sensor surface, thereby reducing assay times. The prospect of rotation-induced flux was first investigated utilizing label-free detection of porcine parvovirus with atomic force microscopy and the results of these studies are presented in Chapter 4. Chapter 5 describes the efforts to define a protocol for the combination of increased assay speed utilizing a rotating substrate with the ultra sensitivity offered by SERS-based detection. This dissertation is concluded with a summation of the insights gained through these works and a discussion of the future prospects of these technologies.

References

(1) Yalow, R. S.; Berson, S. A. *Nature* **1959**, *184*, 1648-1649.

(2) Sokoll, L. J.; Chan, K. W. *Anal. Chem.* **1999**, *71*, 356R-362R.

(3) Clemente, A.; Chambers, S. J.; Lodi, F.; Nicoletti, C.; Brett, G. M. *Food Control* **2004**, *15*, 65-69.

(4) Sarter, S.; Zakhia, N. *Luminescence* **2004**, *19*.

(5) Liu, L.; Chen, F.-C.; Dorsey, J.; Hsieh, Y.-H. P. *J. Food Sci.* **2006**, *71*, M1-M6.

(6) Oubina, A.; Ballesteros, B.; Carrasco, P. B.; Galve, R.; Gascon, J.; Iglesias, F.; Sanvicens, N.; Marco, M.-P. In *Techniques and Instrumentation in Analytical Chemistry*; Barcelo, D., Ed.; Elsevier Science B. V.: Amsterdam, 2000; Vol. 21 (Sample Handling and Trace Analysis of Pollutants, pp 287-339.

(7) VanEmon, J. M.; Lopeze-Avila, V. *Anal. Chem.* **1992**, *64*, 79A-88A.

(8) Yu, Y.-Y.; Wang, Q.-E.; Zhuang, H.-S. *Anal. Lett.* **2006**, *39*, 937-946.

(9) Mauriz, E.; Calle, A.; Lechuga, L. M.; Quintana, J.; Montoya, A.; Manclus, J. J. *Anal. Chim. Acta* **2006**, *561*, 40-47.

(10) Mauriz, E.; Calle, A.; Montoya, A.; Lechuga, L. M. *Talanta* **2006**, *69*, 359-364.

(11) Hock, B.; Giersch, T.; Kramer, K. *Analusis* **1992**, *20*, 29-33.

(12) Chomel, B. B. *J. Vet. Med. Educ.* **2003**, *30*, 145-147.

(13) Diamandis, E. P.; Christoulos, T. K., Eds. *Immunoassay*; Academic Press: San Diego, CA, 1996.

(14) Edwards, R. *Immunoassay: An Introduction*; William Heinemann Medical Books: London, 1985.

(15) Jackson, T. M.; Ekins, R. P. *J. Immunol. Meth.* **1986**, *87*, 13-20.

(16) Porter, M. D.; Bright, T. B.; Allara, D. L.; Chidsey, C. E. D. *J. Am. Chem. Soc.* **1987**, *109*, 3559-3568.

(17) Bain, C. D.; Biebuyck, H. A.; Whitesides, G. M. *Langmuir* **1989**, *5*, 723-727.

(18) Zhong, C.-J.; Brush, R. C.; Anderegg, J.; Porter, M. D. *Langmuir* **1999**, *15*, 518-525.

(19) Wagner, P.; Hegner, M.; Kernen, P.; Zaugg, F.; Semenza, G. *Biophys. J.* **1996**, *70*, 2052-2066.

(20) Hermanson, G. T. *Bioconjugate Techniques*; Academic Press: San Diego, 1996.

(21) Duhachek, S. D.; Kenseth, J. R.; Casale, G. P.; Small, G. J.; Porter, M. D.; Jankowiak, R. *Anal. Chem.* **2000**, *72*, 3709-3716.

(22) Gooding, J. J.; Hibbert, D. B. *Trends Anal. Chem.* **1999**, *18*, 525-533.

(23) Dong, Y.; Shannon, C. *Anal. Chem.* **2000**, *72*, 2371-2376.

(24) Su, X.-L.; Li, Y. *Biosens. Bioelectron.* **2003**, *19*, 563-574.

(25) Gering, J. P.; Quaroni, L.; Chumanov, G. *J. Colloid Interf. Sci.* **2002**, *252*, 50-56.

(26) Zhang, C. X.; Liu, H. P.; Tang, Z. M.; He, N. Y.; Lu, Z. H. *Electrophoresis* **2003**, *24*, 3279-3283.

(27) Du, J.; Chen, B.; Zhang, C.; Xu, X.; Cheng, J.; Gao, F.; Lu, Z. *Sensors* **2005**, *5*, 250-257.

(28) Diamandis, E. P.; Christoulos, T. K. *Anal. Chem.* **1990**, *62*, 1149A-1157A.

(29) Kricka, L. J. *Pure Appl. Chem.* **1996**, *68*, 1825-1830.

(30) Monroe, D. *Anal. Chem.* **1984**, *56*, 920A-931A.

(31) Wians, F. H.; Dev, J.; Powell, M. M.; Heald, J. I. *Clin. Chem.* **1986**, *32*, 887-890.

(32) Gosling, J. P. In *Immunoassay: Laboraory Analysis and Clinical Application*; Gosling, J. P., Basso, L. V., Eds.; Butterworth-Heinemann: Boston, 1994, pp 1-30. .

(33) White, S. R.; Chiu, N. H. L.; Christoulos, T. K. *Methods* **2000**, *22*, 24-32.

(34) Engvall, E.; Perlmann, P. *Immunochem.* **1971**, *8*, 871-874.

(35) VanWeemen, B. K.; Schuurs, A. H. W. M. *FEBS Lett.* **1971**, *15*, 232-236.

(36) Jenkins, S. H. *J. Immunol. Meth.* **1992**, *150*, 91-97.

(37) Smith, E. A.; Corn, R. M. *Appl. Spectrosc.* **2003**, *57*, 320A-332A.

(38) Mullett, W. M.; Lai, E. P. C.; Yeung, J. M. *Methods* **2000**, *22*, 77-91.

(39) Lyon, L. A.; Musick, M. D.; Natan, M. J. *Anal. Chem.* **1998**, *70*, 5177-5183.

(40) Nelson, B. P.; Grimsrud, T. E.; Liles, M. R.; Goodman, R. M.; Corn, R. M. *Anal. Chem.* **2001**, *73*, 1-7.

(41) Miyashita, M.; Shimada, T.; Miyagawa, H.; Akamatsu, M. *Anal. Bioanal. Chem.* **2005**, *381*, 667-673.

(42) Gobi, K. V.; Kataoka, C.; Miura, N. *Sensor Actuator B* **2005**, *108*, 784-790.

(43) Sun, B.; Xie, W.; Yi, G.; Chen, D.; Zhou, Y.; Cheng, J. *J. Immunol. Meth.* **2001**, *249*, 85-89.

(44) Goldman, E. R.; Balighian, E. D.; Kuno, M. K.; Labrenz, S.; Tran, P. T.; Anderson, G. P.; Mauro, J. M.; Mattoussi, H. *Phys. Stat. Sol. B* **2002**, *229*, 407-414.

(45) Goldman, E. R.; Balighian, E. D.; Mattoussi, H.; Kuno, M. K.; Mauro, J. M.; Tran, P. T.; Anderson, G. P. *J. Am. Chem. Soc.* **2002**, *124*, 6378-6382.

(46) Goldman, E. R.; Anderson, G. P.; Tran, P. T.; Mattoussi, H.; Charles, P. T.; Mauro, J. M. *Anal. Chem.* **2002**, *74*, 841-847.

(47) Goldman, E. R.; Medintz, I. L.; Mattoussi, H. *Anal. Bioanal. Chem.* **2006**, *384*, 560-563.

(48) Tran, P. T.; Goldman, E. R.; Anderson, G. P.; Mauro, J. M.; Mattoussi, H. *Phys. Stat. Sol. B* **2002**, *229*, 427-432.

(49) Hahn, M. A.; Tabb, J. S.; Krauss, T. D. *Anal. Chem.* **2005**, *77*, 4861-4869.

(50) Su, X.-L.; Li, Y. *Anal. Chem.* **2004**, *76*, 4806-4810.

(51) Chan, W. C. W.; Nie, S. *Science* **1998**, *281*, 2016-2018.

(52) Wu, G.; Datar, R. H.; Thundat, K. M. H.; Cote, R. J.; Majumdar, A. *Nature Biotechnol.* **2001**, *19*, 856-860.

(53) Grogan, C.; Raiteri, R.; O'Connor, G. M.; Glynn, T. J.; Cunningham, V.; Kane, M.; Charlton, M.; Leech, D. *Biosens. Bioelectron.* **2002**, *17*, 201-207.

(54) Llic, B.; Yang, Y.; Craighead, H. G. *Appl. Phys. Lett.* **2004**, *85*, 2604-2606.

(55) Butler, J. E. *J. Immunoassay* **2000**, *21*, 165-209.

(56) Driskell, J. D.; Kwarta, K. M.; Lipert, R. J.; Porter, M. D.; Neill, J. D.; Ridpath, J. F. *Anal. Chem.* **2005**, *77*, 6147-6154.

(57) Grubisha, D. S.; Lipert, R. J.; Park, H.-Y.; Driskell, J.; Porter, M. D. *Anal. Chem.* **2003**, *75*, 5936-5943.

(58) Ni, J.; Lipert, R. J.; Dawson, B.; Porter, M. D. *Anal. Chem.* **1999**, *71*, 4903-4908.

(59) Dou, X.; Takama, T.; Yamaguchi, T.; Tamamoto, H.; Ozaki, Y. *Anal. Chem.* **1997**, *69*, 1492-1495.

(60) Rohr, T. E.; Cotton, T.; Fan, N.; Tarcha, P. J. *Anal. Biochem.* **1989**, *182*, 388-398.

(61) Xu, S.; Ji, X.; Xu, W.; Li, X.; Wang, L.; Bai, Y.; Zhao, B.; Ozaki, Y. *Analyst* **2004**, *129*, 63-68.

(62) Mulvaney, S. P.; Musick, M. D.; Keating, C. D.; Natan, M. J. *Langmuir* **2003**, *19*, 4784-4790.

(63) Zhang, X.; Young, M. A.; Lyandres, O.; Duyne, R. P. V. *J. Am. Chem. Soc.* **2005**.

(64) Ansari, D. O.; Stuart, D. A.; Nie, S. *Proc. of SPIE* **2005**, *5699*, 82-90.

(65) Cao, Y. C.; Jin, R.; Mirkin, C. A. *Science* **2002**, *297*, 1536-1540.

(66) Faulds, K.; Smith, W. E.; Graham, D. *Anal. Chem.* **2004**, *76*, 412-417.

(67) Faulds, K.; Barbagallo, R. P.; Keer, J. T.; Smith, W. E.; Graham, D. *Analyst* **2004**, *129*, 567-568.

(68) Graham, D.; Mallinder, B. J.; Whitcombe, D.; Smith, W. E. *ChemPhysChem* **2001**, *12*, 746-748.

(69) Graham, D.; Mallinder, B. J.; Whitcombe, D.; Watson, N. D.; Smith, W. E. *Anal. Chem.* **2002**, *74*, 1069-1074.

(70) Cui, Y.; Ren, B.; Yao, J.-L.; Gu, R.-A.; Tian, Z.-Q. *J. Phys. Chem. B* **2006**, *110*, 4002-4006.

(71) Karlsson, R.; Falt, A. *J. Immunol. Meth.* **1997**, *200*, 121-133.

(72) Frackelton, A. R.; Weltman, J. K. *J. Immunol.* **1980**, *124*, 2048-2054.

(73) Stenberg, M.; Nygren, H. *J. Theor. Biol.* **1985**, *113*, 589-597.

(74) Stenberg, M.; Stiblert, L.; Nygren, H. *J. Theor. Biol.* **1986**, *120*, 129-140.

(75) Nygren, H.; Werthen, M.; Stenberg, M. *J. Immunol. Meth.* **1987**, *101*, 63-71.

(76) Myszka, D. G.; Morton, T. A.; Doyle, M. L.; Chaiken, I. M. *Biophys. Chem.* **1997**, *64*, 127-137.

(77) Heller, M. J.; Forster, A. H.; Tu, E. *Electrophoresis* **2000**, *21*, 157-164.

(78) Ewalt, K. L.; Haigis, R. W.; Rooney, R.; Ackley, D.; Krihak, M. *Anal. Biochem.* **2001**, *289*, 162-172.

(79) Glaser, R. W. *Anal. Biochem.* **1993**, *213*, 152-161.

(80) Hofmann, O.; Voirin, G.; Niedermann, P.; Manz, A. *Anal. Chem.* **2002**, *74*, 5243-5250.

(81) Johnstone, R. W.; Andrew, S. M.; Hogarth, M. P.; Pietersz, G. A.; McKenzie, I. F. C. *Mol. Immunol.* **1990**, *27*, 327-333.

(82) Yang, J. M.; Bell, J.; Huang, Y.; Tirado, M.; Thomas, D.; Forster, A. H.; Haigis, R. W.; Swanson, P. D.; Wallace, R. B.; Martinsons, B.; Krihak, M. *Biosens. Bioelectron.* **2002**, *17*, 605-618.

(83) Pribyl, M.; Snita, D.; Hasal, P.; Marek, M. *Chem. Eng. J.* **2004**, *101*, 303-314.

(84) Qian, S.; Bau, H. H. *Anal. Biochem.* **2003**, *322*, 89-98.

(85) Oku, Y.; Kamiya, K.; Kamiya, H.; Shibahara, Y.; Ii, T.; Uesaka, Y. *J. Immunol. Meth.* **2001**, *258*, 73-84.

(86) Chan, C. P. Y.; Sum, K. W.; Cheung, K. Y.; Glatz, J. F. C.; Sanderson, J. E.; Hempel, L.; Lehmann, M.; Renneberg, L.; Renneberg, R. *J. Immunol. Meth.* **2003**, *279*, 91-100.

(87) O'Keeffe, M.; Crabbe, P.; Salden, M.; Wichers, J.; Peteghem, C. V.; Kohen, F.; Pieraccini, G.; Moneti, G. *J. Immunol. Meth.* **2003**, *278*, 117-126.

(88) Fernandez-Sanchez, C.; McNeil, C. J.; Rawson, K.; Nilsson, O. *Anal. Chem.* **2004**, *76*, 5649-5656.

(89) Al-Yousif, Y.; Anderson, J.; Chard-Bergstrom, C.; Kapil, S. *Clin. Diagn. Lab. Immunol.* **2002**, *9*, 723-724.

(90) Slinger, R.; Milk, R.; Gaboury, I.; Diaz-Mitoma, F. *J. Clin. Microbiol.* **2004**, *42*, 3731-3733.

(91) Wittmann, C.; Bilitewski, U.; Giersch, T.; Kettling, U.; Schmid, R. D. *Analyst* **1996**, *121*, 863-869.

(92) Ingle Jr., J. D.; Crouch, S. R. *Spectrochemical Analysis*; Prentice Hall: Upper Saddle River, NJ, 1988.

(93) Fleischmann, M.; Hendra, P. J.; McQuillan, A. J. *Chem. Phys. Lett.* **1974**, *26*, 163-166.

(94) Jeanmaire, D. L.; VanDuyne, R. P. *J. Electroanal. Chem. Interf. Electrochem.* **1977**, *84*, 1-20.

(95) Albrecht, M. G.; Creighton, J. A. *J. Am. Chem. Soc.* **1977**, *99*, 5215-5217.

(96) Schatz, G. C. *Acc. Chem. Res.* **1984**, *17*, 370-376.

(97) Moskovits, M. *J. Chem. Phys.* **1978**, *69*, 4159-4161.

(98) Otto, A.; Timper, J.; Billmann, J.; Kovacs, G.; Pockrand, I. *Surf. Sci.* **1980**, *92*, L55-L57.

(99) Schatz, G. C.; VanDuyne, R. P. *Surf. Sci.* **1980**, *101*, 425-438.

(100) Wang, D.-S.; Chew, H.; Kerker, M. *Appl. Opt.* **1980**, *19*, 2256-2257.

(101) Kerker, M.; Siiman, O.; Bumm, L. A.; Wang, D.-S. **1980**.

(102) Gersten, J.; Nitzan, A. *J. Phys. Chem.* **1980**, *73*, 3023-3037.

(103) Gersten, J. I. *J. Chem. Phys.* **1980**, *72*, 5779-5780.

(104) Aravind, P. K.; Nitzan, A.; Metiu, H. *Surf. Sci.* **1981**, *110*, 189-204.

(105) Abe, H.; Manzel, K.; Schulze, W.; Moskovits, M.; DiLella, D. P. *J. Chem. Phys.* **1981**, *74*, 792-797.

(106) Persson, B. N. J. *Chem. Phys. Lett.* **1981**, *82*, 561-565.

(107) Adrian, F. J. *J. Chem. Phys.* **1982**, *77*, 5302-5314.

(108) Creighton, J. A. *Surf. Sci.* **1983**, *124*, 209-219.

(109) Kerker, M. *Acc. Chem. Res.* **1984**, *17*, 271-277.

(110) Zeman, E. J.; Schatz, G. C. *J. Phys. Chem.* **1987**, *91*, 634-643.

(111) Kambhampati, P.; Child, C. M.; Foster, M. C.; Campion, A. *J. Chem. Phys.* **1998**, *108*, 5013-5026.

(112) King, F. W.; VanDuyne, R. P.; Schatz, G. C. *J. Chem. Phys.* **1978**, *69*, 4472-4481.

(113) Efrima, S.; Metiu, H. *J. Chem. Phys.* **1979**, *70*, 1602-1613.

(114) Kraus, W. A.; Schatz, G. C. *J. Chem. Phys.* **1983**, *79*, 6130-6139.

(115) Wokaun, A.; Gordon,.J. P.; Liao, P. F. *Phys. Rev. Lett.* **1982**, *48*, 957-960.

(116) Meier, M.; Wokaun, A. *Opt. Lett.* **1983**, *8*, 581-583.

(117) Weitz, D. A.; Garoff, S.; Gramila, T. J. *Opt. Lett.* **1982**, *7*, 168-170.

(118) Oldenburg, S. J.; Jackson, J. B.; Westcott, S. L.; Halas, N. J. *Appl. Phys. Lett.* **1999**, *75*, 2897-2899.

(119) Kneipp, K.; Kneipp, H.; Itzkan, I.; Dasari, R. R.; Feld, M. S. *J. Phys. : Condens. Mat.* **2002**, *14*, R597-R624.

(120) Felidj, N.; Aubard, J.; Levi, G.; Krenn, J. R.; Hohenau, A.; Schider, G.; Leitner, A.; Aussenegg, F. R. *Appl. Phys. Lett.* **2003**, *82*, 3095-3097.

(121) Haynes, C. L.; Duyne, R. P. V. *J. Phys. Chem. B* **2003**, *107*, 7426-7433.

(122) Kelly, K. L.; Coronado, E.; Zhao, L. L.; Schatz, G. C. *J. Phys. Chem. B* **2003**, *107*, 668-677.

(123) Sherry, L. J.; CHang, S.-H.; Schatz, G. C.; VanDuyne, R. P. *Nano Lett.* **2005**, *5*, 2034-2038.

(124) Orendorff, C. J.; Gole, A.; Sau, T. K.; Murphy, C. J. *Anal. Chem.* **2005**.

(125) Reinhard, B. M.; Siu, M.; Agarwal, H.; Alivisatos, A. P.; Liphardt, J. *Nano Lett.* **2005**.

(126) Holland, W. R.; Hall, D. G. *Phys. Rev. B* **1983**, *21*, 7765-7768.

(127) Michaels, A. M.; Jiang, J.; Brus, L. *J. Phys. Chem. B* **2000**, *104*, 11965-11971.

(128) Xu, H.; Bjerneld, E. J.; Kall, M.; Borjesson, L. *Phys. Rev. Lett.* **1999**, *83*, 4357-4360.

(129) Jiang, J.; Bosnick, K.; Maillard, M.; Brus, L. *J. Phys. Chem. B* **2003**, *107*, 9964-9972.

(130) Wei, Q.-H.; Su, K.-H.; Durant, S.; Zhang, X. *Nano Lett.* **2004**, *4*, 1067-1071.

(131) Jensen, T. R.; Schatz, G. C.; Duyne, R. P. V. *J. Phys. Chem. B* **1999**, *103*, 2394-2401.

(132) Keating, C. D.; Kovaleski, K. K.; Natan, M. J. *J. Phys. Chem. B* **1998**, *102*, 9414-9425.

(133) Kim, K.; Lee, H. S. *J. Phys. Chem. B* **2005**.

(134) Zheng, J.; Zhou, Y.; Li, X.; Ji, Y.; Lu, T.; Gu, R. *Langmuir* **2003**, *19*, 632-636.

(135) Shchegrov, A. V.; Novikov, I. V.; Maradudin, A. A. *Phys. Rev. Lett.* **1997**, *78*, 4269-4272.

(136) Kim, K.; Yoon, J. K. *J. Phys. Chem. B* **2005**.

(137) Eustis, S.; El-Sayed, M. A. *Chem. Soc. Rev.* **2006**.

(138) Creighton, J. A. In *Surface Enhanced Raman Scattering*; Chang, R. K., Furtak, T. E., Eds.; Plenum Press: New York, 1982, pp 315-337.

(139) Bohren, C. F.; Huffman, D. R. *Absorption and Scattering of Light by Small Particles*; John Wiley & Sons, Inc.: New York, 1983.

(140) Lazarides, A. A.; Schatz, G. C. *J. Phys. Chem. B* **2000**, *104*, 460-467.

(141) Storhoff, J. J.; Elghanian, R.; Mucic, R. C.; Mirking, C. A.; Robert, L. L. *J. Am. Chem. Soc.* **1998**, *120*, 1959-1964.

(142) Okamoto, T.; Yamaguchi, I. *J. Phys. Chem. B* **2003**, *107*, 10321-10324.

(143) Aravind, P. K.; Metiu, H. *Surf. Sci.* **1983**, *124*, 506-528.

(144) Wind, M. M.; Vlieger, P. A. B. J.; Bedeaux, D. *Physica* **1987**, *143 A*, 164-182.

(145) Link, S.; El-Sayed, M. A. *J. Phys. Chem. B* **1999**, *103*, 8410-8426.

(146) Jensen, R. R.; Duval, M. L.; Kelly, K. L.; Lazarides, A. A.; Schatz, G. C.; Duyne, R. P. V. *J. Phys. Chem. B* **1999**, *103*, 9846-9853.

(147) Kahl, M.; Voges, E. *Phys. Rev. B* **2000**, *61*, 14078-14088.

(148) Liao, P. F.; Stern, M. B. *Opt. Lett.* **1982**, *7*, 483-485.

(149) Haynes, C. L.; Duyne, R. P. V. *J. Phys. Chem. B* **2001**, *105*, 5599-5611.

(150) Felidj, N.; Aubard, J.; Levi, G.; Krenn, J. R.; Schider, G.; Leitner, A.; Aussenegg, F. R. *Phys. Rev. B* **2002**, *66*, 245407.

CHAPTER 2: LOW-LEVEL DETECTION OF VIRAL PATHOGENS BY A SURFACE-ENHANCED RAMAN SCATTERING BASED IMMUNOASSAY

A paper published in *Analytical Chemistry* **2005**, 77, 6147-6154

Jeremy D. Driskell, Karen M. Kwarta, Robert J. Lipert and Marc D. Porter
Iowa State University, Institute for Combinatorial Discovery, Departments of Chemistry and of Chemical and Biological Engineering, Ames Laboratory-U.S. DOE, Ames, IA 50011-3020
John D. Neill and Julia F. Ridpath
Virus and Prion Diseases of Livestock Unit, National Animal Disease Center, United States Department of Agriculture, Ames, IA 50010

Abstract

The need for rapid, highly sensitive, and versatile diagnostic tests for viral pathogens spans from human and veterinary medicine to bioterrorism prevention. As an approach to meet these demands, a diagnostic test employing monoclonal antibodies (mAbs) for the selective extraction of viral pathogens from a sample in a chip-scale, sandwich immunoassay format has been developed using surface-enhanced Raman scattering (SERS) as a readout method. The strengths of SERS-based detection include its inherent high sensitivity and facility for multiplexing. The capability of this approach is demonstrated by the capture of feline calicivirus (FCV) from cell culture media that is exposed to a gold substrate modified with a covalently immobilized layer of anti-FCV mAbs. The surface-bound FCVs are subsequently coupled with an extrinsic Raman label (ERL) for identification and quantification. The ERLs consist of 60-nm gold nanoparticles coated first with a layer of Raman reporter molecules and then a layer of mAbs. The Raman reporter molecule is strategically designed to chemisorb as a thiolate adlayer on the gold nanoparticle, to provide a strong and unique spectral signature, and to covalently link a layer of mAbs to the gold nanoparticle. The last feature provides a means to selectivity tag substrate-bound FCV. This paper describes the development of the assay, which uses cell culture media as a sample matrix, and has a linear dynamic range of 1×10^6 to 2.5×10^8 viruses/mL and a limit of detection of 1×10^6 viruses/mL. These results reflect the findings from a detailed series of investigations on the effects of several experimental parameters (e.g., salt concentration, ERL binding buffer, and sample agitation), all of which were aimed at minimizing nonspecific binding and maximizing FCV binding efficiency. The performance of the assay is correlated with the number of captured FCV, determined by atomic force microscopy, as a means of method validation.

Introduction

The development of a versatile strategy for pathogen detection is central to human healthcare, veterinary medicine, and bioterrorism prevention.[1] In the area of viral pathogen detection, the most used techniques include electron microscopy, fluorescent antibody labeling of frozen tissue sections (FATS), ELISA, polymerase chain reaction (PCR), DNA hybridization, virus isolation, and serologic testing.[2] These methodologies, however, often lack the sensitivity, specificity, speed, cost, versatility, portability and/or throughput sought for such applications.

At present, two avenues are being heavily explored to overcome these limitations. One approach relies on the recognition of nucleic acid motifs. Reports have detailed strategies to reduce the analysis time for viral detection by PCR,[3, 4] and to increase sample throughput by PCR multiplexing.[5] The second approach, which has more historical precedence, utilizes the recognition of protein motifs. These assays take advantage of the documented specificity of antibody-antigen interactions, which facilitates method development and optimization. Several of these assays have also been coupled to novel readout technologies including immunoimaging atomic force microscopy (AFM),[6] immunosorbent scanning electron microscopy (SEM),[7, 8] fluorescence-based labeling[9] and antibody-modified microcantilevers.[10] These techniques have characteristics that address various weaknesses of the more conventional detection methods, including reductions in the limits of detection, which range from 10^5 viruses/mL for fluorescence[9] and microcantilever detection[10] to 10^8 viruses/mL for AFM detection.[6] This report introduces a protein-based readout technique that has the potential to increase sample throughput, decrease readout time, enhance portability, and lower the limit for virus detection.

One of the more recent readout techniques developed for immunoassays[11-18] and DNA detection[19-23] relies on surface-enhanced Raman scattering (SERS). As part of our interest in this area, Ni et al.[13] exploited the attributes of SERS for the concurrent analysis of different IgGs. That work employed extrinsic Raman labels (ERLs). ERLs consist of gold nanoparticles that are modified with both an intrinsically strong Raman scatterer and an antibody. The former takes advantage of the well-established enhancement of scatterers when coated on nanometer-sized gold particles,[24] whereas the latter imparts the specificity for a target analyte. We have demonstrated the sensitivity of this type of immunoassay by the low level (~1 pg/mL) detection of prostate specific antigen (PSA) in spiked human serum samples,[14] a limit of detection estimated to result from ~60 binding events when using 30-nm diameter gold nanoparticles. We have also shown that optimizing the nanoparticle diameter with respect to laser excitation wavelength can lead to the facile detection of single-digit binding events in the absence of nonspecific adsorption.[25, 26]

The work herein extends our SERS-based immunoassay to the direct, low level detection of intact pathogenic viruses, using feline calicivirus (FCV) as a model target and cell growth media as a mimic of a biological sample matrix. To our knowledge, there has been only one study to date on the utilization of SERS for virus antigen detection;[15] that work, however, detected only the capsid protein after it was detached from intact virus in a chip-based format that partially paralleled those in other reports.[11-14, 25]

FCV is a leading cause of upper respiratory infection in cats. FCV is a non-enveloped virus that has a capsid composed of 180 identical copies of a 76 kDa protein,[27] and a hydrated radius of 36 nm.[28] Moreover, FCV has strong morphological (size and shape) and genetic similarities to the human caliciviruses, noroviruses and saporviruses.[29] However, FCV and the human caliciviruses are not antigenically cross-reactive. Human caliciviruses are commonly associated with viral gastroenteritis, are extremely contagious, and have been identified as potential bioterrorism agents.[30, 31] The human caliciviruses are particularly difficult to study due to their inability to grow in cell culture, while FCV is readily propagated in vitro.[30, 31] Thus, FCV also serves as a simulant for the human caliciviruses.[32]

Scheme 1 illustrates the steps in our viral immunoassay. Briefly, a monoclonal antibody specific for FCV (anti-FCV mAb) is immobilized via succinimidyl ester chemistry to a gold-bound thiolate adlayer formed from dithiobis(succinimidyl propionate) (DSP). When FCV is present, the immobilized layer of anti-FCV mAb (capture substrate) specifically extracts available virus. The substrate is then incubated with ERLs that bind to captured FCV. The ERLs consist of 60-nm gold particles modified by exposure to 5,5'-dithiobis(succinimidyl-2-nitrobenzoate) (DSNB). The nitro group of the resulting thiolate adlayer provides an intense SERS signal, while the succinimide group acts as a coupling agent for tethering anti-FCV mAb to the nanoparticle. The quantity of FCV is determined by the spectral intensity of the symmetric nitro stretch ($\nu_s(NO_2)$) of the DSNB-derived coating, which is also correlated with the number of captured FCV by imaging with atomic force microscopy as a means of method validation. The following sections describe the findings from this investigation, including details related to assay optimization and the ability of our SERS-based methodology to detect FCV in cell growth media at ~1 x 10^6 viruses/mL.

Experimental

Reagents. Gold nanoparticles [60 nm (<8% variation in diameter), 2.6 x 10^{10} particles/mL] were purchased from Ted Pella. Octadecanethiol (ODT), sodium chloride, dithiobis(succinimidyl propionate) (DSP), phosphate buffered saline (PBS) packs (10 mM), bovine serum albumin (BSA) and Triton X-100 were received from Sigma. Poly(dimethyl siloxane) (PDMS) was obtained from Dow Corning. SuperBlock and borate buffer packs (50 mM) were acquired from Pierce. 5,5'-dithiobis(succinimidyl-2-nitrobenzoate) (DSNB) was synthesized according to a recent literature procedure.[14]

Anti-FCV monoclonal antibodies (anti-FCV 2D10-1C4), purified via a protein G column (Pro-Chem) to 99.9% purity, were provided as 1 mg/mL stock solutions by National Animal Disease Center (NADC; Ames, IA). Aliquots of FCV (NADC strain), suspended in cell culture media (MEM media, CRFK cells), were also supplied by NADC. The FCV concentration of the stock solution (5.0 x 10^8 viruses/mL) is reported as the 50% tissue culture infective dose ($TCID_{50}$), which was determined by the Reed-Muench method.[33] All dilutions of this stock were made with cell culture media.

Preparation of ERLs. ERLs are designed to: 1) provide a strong Raman signal; and 2) demonstrate immuno-specificity.[13, 14, 25] Furthermore, the colloidal suspension needs to be stable with respect to aggregation, and the suspending solution should be compatible with effective antigen-antibody binding. In earlier work,[14, 25] DSNB was synthesized to meet both attributes. Its symmetric nitro stretch has an intrinsically large Raman scattering cross section. Moreover, DSNB is bifunctional from a reactivity perspective. DSNB contains both a disulfide moiety, which chemisorbs as an adlayer of the corresponding thiolate to the surface of the gold nanoparticles, and a succinimidyl ester group, which couples to anti-FCV mAb via amide linkage.[34-36]

Prior to modifying with DSNB, the pH of the nanoparticle solution was adjusted to 8.5 by adding 40 µL of 50 mM borate buffer to a 1.0-mL solution of gold nanoparticles. This pH: 1) is above the pI of the mAb, which inhibits aggregation of the labeled nanoparticles; and 2) deprotonates the amines of the mAb, which favors the formation of an amide linkage by reaction with the succinimidyl ester of DSNB. After pH adjustment, 10 µL of 1 mM DSNB in acetonitrile were pipetted into the colloidal solution and mixed for 8 h. Next, 20 µg of anti-FCV mAb were added to the colloidal solution and allowed to react for 12 h. Flocculation tests indicated that this step effectively coated the suspended colloid.[37, 38]

The flocculation experiments, summarized by the extinction spectra in Figure 1, systematically varied the amount of anti-FCV mAb added to the colloidal solution and monitored aggregation upon the addition of NaCl. These experiments first pipetted 40 μL of borate buffer into 1000 μL of the as-received nanoparticle solution to adjust the pH to 8.5, followed by 100 μL of anti-FCV mAb solutions with different amounts (5-50 μg) and 100 μL of a concentrated NaCl solution to reach a final NaCl concentration of 150 mM (see below). At this point, the sample modified with 5 μg of anti-FCV mAb changed within a few minutes from a red to blue color, followed by the gradual appearance of a precipitate; all other samples appeared stable with respect to aggregation. After allowing all solutions to stand for 30 min, 200 μL of each solution were then diluted with 800 μL of deionized water in order to reduce the particle concentration for effective characterization by their extinction spectra.

As shown in Figure 1, the as-received particle solution has a strong extinction maximum at 535 nm that is consistent with the location of the plasmon resonance of isolated gold particles with an average diameter of 60 nm.[39] The loss of particles from the solution modified with 5 μg of anti-FCV mAb is further evident by the large decrease in the magnitude of the plasmon band, noting that the decrease in extinction solely from dilution should be only ~25%. The broadening and shift to longer wavelengths is also diagnostic of aggregate formation. The changes upon addition of larger quantities of anti-FCV are in reasonable agreement with expectations from dilution, and are an indication of stable colloidal solutions. Moreover, there was no observable precipitate for samples stored for several weeks. All subsequent procedures therefore modified the particles by addition of 20 μg of mAbs in order to minimize consumption.

To stabilize the ERLs and to block unreacted succinimidyl esters, the colloidal solution was modified by the addition of 10% BSA in 2 mM borate buffer (100 μL) for 6 h. The suspension was then centrifuged at 2000*g* for 10 min to remove any excess DSNB, mAb and other residual materials. After decanting the clear supernatant, the loose red sediment was resuspended in 1.0 mL of 2 mM borate buffer containing 1% BSA. The centrifugation/resuspension cycle was repeated twice for thorough removal of excess reagents. The final volume of the resuspension buffer was varied to control the nanoparticle concentration, a step that included the addition of the appropriate volume of 1.5 M NaCl to yield a final NaCl concentration of 150 mM (see below). As a final step, the labeled nanoparticles were passed through a 0.22-μm syringe filter (Costar) to remove any large aggregates.

Capture Substrate Preparation. Template stripped gold (TSG)[40] served as the capture substrate because its low roughness factor facilitated AFM imaging of the virus for protocol development and assay validation.[41] TSG was prepared by resistively evaporating ~250 nm of gold (99.9% purity) at a rate of 0.1 nm/s onto a 4-inch p-type silicon [111] wafer (University Wafer) with an Edwards 306A resistive evaporator. Glass microscope slides were cut into 1 x 1 cm squares and ultrasonically bathed in diluted Contrad 70 (Micro, Cole-Parmer), deionized water, and ethanol, each for 30 min. The clean glass chips were affixed to the gold-coated wafer with 2-part epoxy (Epoxy Technology) and cured at 150 °C for 1.75 h.

The glass chips were then gently detached from the silicon wafer, which removes the sandwiched gold film, to yield a smooth gold surface on the topside of the glass chip.

The TSG chips were exposed for ~30 s to an ODT-soaked PDMS stamp with a 3-mm hole cut in its center, rinsed with ethanol, and dried under a stream of high purity nitrogen.[42-44] The ODT-based adlayer formed a hydrophobic barrier for localizing reagents in a confined sample area, which minimized the consumption of antibody and virus solutions. The substrate was then submerged in a 0.1 mM ethanolic DSP solution for ~12 h, rinsed with ethanol, and dried under a stream of high purity nitrogen. This step formed a DSP-based adlayer at the center of the substrate, i.e., the area not inked by ODT in the stamping process.

Anti-FCV mAb (20 μL, 100 μg/mL), diluted in 50 mM borate buffer (pH 8.5), was applied to the sample area for 8 h in a humidity chamber. This step forms a capture antibody layer by coupling through the terminal succinimidyl ester of the DSP-derived monolayer.[34-36] The substrate was rinsed by its immersion in three separate solutions of 10 mM PBS (2.25 mL). Next, 20 μL of SuperBlock blocking buffer were pipetted onto the sample area and then rinsed with 10 mM PBS after a 12-h exposure.

The capture substrate was exposed to 20 μL aliquots of virus, diluted in cell culture media, for 8 h at room temperature in a humidity chamber and then rinsed with 2 mM borate buffer containing 1% BSA and 150 mM NaCl. The target FCV was captured directly from a freeze/thaw lysate of cultured cells. The captured viruses were then exposed to the labeled nanoparticles for ~12 h at room temperature in a humidity chamber. These incubations were performed either with 20 μL of labeled nanoparticles (5.2×10^{10} particles/mL) under stagnant conditions or with 1.0 mL of labeled nanoparticles (1.3×10^{10} particles/mL) in a 24-well plate on a shaker (New Brunswick) with agitation (90 rpm). The substrates were rinsed with

2 mM borate buffer (150 mM NaCl and 1% BSA) before drying with a stream of high purity nitrogen gas and measuring the SERS signal.

Instrumentation. (i) SERS Measurements. The Raman spectra were collected with a NanoRaman I fiber-optic-based Raman system (Concurrent Analytical), a portable, field-deployable instrument. The light source was a 30 mW, 632.8 nm He-Ne laser. The spectrograph consisted of an f/2.0 Czerny-Turner imaging spectrometer (6-8 cm^{-1} resolution) and a Kodak 0401E CCD thermoelectrically cooled to 0 °C. The incident laser light was focused to a 25-μm spot size on the substrate at normal incidence using an objective with a numerical aperture of 0.68; the power at the sample was ~3 mW. The same objective was used to collect the scattered radiation. All spectra were acquired with a 1-s integration.

(ii) Atomic Force Microscopy (AFM). Substrates containing captured viruses were imaged utilizing a MultiMode NanoScope IIIa SFM (Digital Instruments) equipped with a 150-μm scanner. The AFM was operated in TappingMode, imaging 5 x 5 μm areas at a scan rate of 1.5 Hz. The setpoint oscillation amplitude was set to 80% of the free oscillation amplitude. The cantilevers were n(+)-silicon TESP probes (Nanosensors) with a length of 118 μm, a width of 27-29 μm, thickness of 3.6-4.5 μm, a spring constant of 32-70 N/m, and a resonant frequency of 327-421 kHz. The viruses in each image were enumerated manually.

Results and Discussion

Preliminary Findings. Initial attempts to detect FCV with SERS readout employing the labeling protocol developed in our immunoassay for PSA[14] proved only marginally successful. AFM studies revealed that while the capture substrate effectively extracted a high number of FCV from spent culture media, the strength of the signal from the ERLs after completing the labeling step was barely above background. There were two plausible origins for this observation. One, the ERLs failed to couple to the surface-bound FCV at a detectable level. Two, the composition of the solution employed in the ERL binding step (2 mM tris buffer, pH 7.6) triggered the loss of captured FCV by degrading the antigen-antibody interaction.

As a consequence, we re-examined the preparation of the ERLs and the solutions employed in several of the assay steps in an effort to both optimize the labeling step in the immunoassay and to minimize nonspecific ERL binding. Based on our earlier experiences in using ERLs,[13, 14, 25] four factors were manipulated and tested: ionic strength of the rinsing buffers and ERL solution, binding buffer of the ERLs, blocking buffer, and surfactant additives in the ERL solution. The following sections present the key results from the optimization investigations, including ionic strength, binding buffer, and agitation, while the evaluation of blocking agents and surfactants are summarized in the supporting information. The final section details the performance and validation of the optimized assay, and briefly draws comparisons to other assay formats.

Effect of Ionic Strength. AFM-based characterizations of the capture substrate after FCV binding, which will also be employed in a subsequent section for assay validation, revealed that the stability of the virus-antibody complex was sensitive to the composition of the solutions used in the rinse steps. Studies, for example, indicated that prolonged exposure to deionized water led to a dramatic reduction in the number of captured viruses. These findings suggested that the low responses in the initial assay attempts reflect a disruption of the virus-antibody interaction in low ionic strength media and the subsequent loss of FCV from the capture substrate. While reasonable to suspect the need for a high ionic strength labeling solution because the antibodies are grown under physiological conditions (i.e., 150 mM NaCl), our work with PSA did not exhibit a strong sensitivity to ionic strength.

The influence of ionic strength on the amount of captured FCV is shown by the AFM images (5 x 5 μm) in Figure 2. These samples were prepared by exposing the capture substrates to 20 μL of stock FCV solution (5.0 x 10^8 viruses/mL). The substrates were then: 1) soaked for ~12 h in 2 mM borate buffer (pH 8.5) of varied NaCl concentration (1 to 150 mM); 2) rinsed with the same soaking solution; 3) gently and quickly rinsed with deionized water and 4) imaged with AFM. As is evident, the images reveal the presence of nanometrically-sized objects that have a surface concentration affected by ionic strength. These objects have a size and shape consistent with the footprint for FCV after drying, which yields particles of ~22 nm in diameter. Smaller, irregularly sized objects are also detected and are ascribed to cell debris and other components in the spent cell culture medium. The presence of captured FCV is supported by a more exacting analysis of the AFM data, which is presented later when validating the SERS-based assay.

The dependence on ionic strength, plotted as the number of captured viruses in a 25-μm^2 image against NaCl concentration (see supporting information) reveals that the number of FCVs bound to the substrate plateaus at ~1000 viruses/25 μm^2 when the salt concentration reaches ~10 mM. In contrast, lower ionic strength solutions resulted in fewer bound viruses.

This result supports the hypothesis that the composition of the ERL solution (2 mM tris) led to the loss of captured FCV in the preliminary experiments. However, the ERLs prepared using our earlier procedures rapidly aggregated upon the addition of 150 mM NaCl. As a consequence, we next focused on determinations of the conditions necessary to stabilize the ERLs in high ionic strength solution, with the goal to enable usage of ERLs suspended in buffers containing 150 mM NaCl in order to match physiological conditions. Systematic studies of nanoparticle centrifugation rate, mAb concentration added to the nanoparticles, the addition of BSA to the nanoparticles, and the pH at which the mAbs coat the nanoparticles led to successful preparation of non-aggregated ERLs in 150 mM NaCl. The results of these studies indicated that using optimum conditions, including a centrifugation rate of 2000g, mAb concentration of 20 µg, BSA concentration of 1%, and pH of 8.5 for mAb adsorption, the ERLs are stable in 150 mM NaCl.

Optimization of ERL Binding Buffer. The next series of experiments examined the effect of the pH of the ERL binding buffer. These experiments reflected possible differences in labeling effectiveness by recognizing that the pH of the borate buffer is alkaline of that used in many immunoassays, which are often designed to closely match physiological conditions. However, ERLs suspended in borate buffer (pH 8.5) were stable in high ionic strength solutions for several weeks, whereas aggregation in phosphate buffer became apparent within ~24 h after the final resuspension step. Similar to the flocculation study in Figure 1, the instability became apparent first by a gradual change in the color of the suspension from red to blue, followed by the appearance of a precipitate and a marked decrease in the extinction at 540 nm. Moreover, a series of flocculation studies indicated that it was the pH and not the identity of the buffer that dictated the stability of the ERLs. Nevertheless, the short-term stability of ERLs in phosphate buffer permitted tests of the influence of pH in the labeling step.

Figure 3 shows the SERS spectra comparing the effect of borate buffer (pH 8.5) to PBS (pH 7.4), both containing 150 mM NaCl and 1% BSA. First, two capture substrates were exposed to a 2.5 x 10^8 viruses/mL solution of FCV. After rinsing, one sample was treated with the borate-buffered ERLs and the other was dosed with the PBS-buffered ERLs. Two more substrates, serving as controls, were exposed to blank cell culture media before treatment with one of the two buffered solutions of ERLs.

The SERS spectra reveal the presence of the ERLs, and have features (e.g., the symmetric nitro stretch, $\nu_s(NO_2)$, at 1336 cm^{-1} and an aromatic ring mode at 1558 cm^{-1}) consistent with the DSNB-derived adlayer. Furthermore, comparisons of the $\nu_s(NO_2)$-intensities yield two additional conclusions. First, the intensity for the samples exposed to FCV (Figure 3A) is nearly three times larger when treated with ERLs in borate buffer compared to those incubated with ERLs in PBS. Second, the intensity of the control (Figure 3B) in PBS is nearly twice that in borate buffer. The borate buffer is therefore more effective at promoting the binding of the ERLs to captured FCV and at minimizing the extent of nonspecific ERL adsorption, potentially translating to a sixfold improvement in the detection limit. We suspect that the pH of PBS is close to the pI of anti-FCV mAb, which would lead to particle aggregation and a larger background signal for the blank. The remainder of these investigations therefore employed the borate buffer.

Effect of Agitation. The last of the key optimization efforts explored the utility of agitating the ERL solution during its incubation with the substrate. Agitation should lower the tendency of ERLs to settle out on the substrate, which would increase the probability of nonspecific binding. For effective agitation, the volume of the ERL solutions was increased to 1.0 mL and the entire substrate was submerged in the resulting suspension.

To this end, the capture substrates were first exposed to either FCV solutions (2.5 x 10^8 viruses/mL) or blank culture media. The substrates were then rinsed and incubated with 1.0-mL solutions of ERLs on a rotary shaker (90 rpm). Importantly, results showed that the intensity of the $\nu_s(NO_2)$ for the FCV-treated substrates was 23000-25000 cts/s, which is similar to that when performing the assay with 20 µL of ERLs under static conditions. The value of agitation becomes evident, however, when examining the signals for the blank samples. The signal from the blank samples is only 525-570 cts/s with agitation, while under static conditions the intensities ranged from 2000 to 5000 cts/s. These results suggest a fourfold to tenfold improvement in the detection limit with the addition of agitation.

SERS-Based Immunoassay of FCV. The results from the optimization studies were employed to design an effective procedure for an immunoassay for FCV. Capture substrates coated with anti-FCV mAbs were incubated with FCV solutions that were diluted in cell culture media to concentrations ranging from 5.0×10^5 to 2.5×10^8 viruses/mL. Representative SERS spectra for each FCV concentration, collected with a 1-s integration time, are shown in Figure 4. We have also carried out a parallel AFM investigation as a means to cross-correlate the SERS responses with the number of captured viruses. A portion of the AFM results are shown in Figure 5. These results, however, are only for captured viruses; this reflects difficulties in reliably imaging virus-bound ERLs after rinsing thoroughly with water to remove the residue that remained when drying samples rinsed with solutions containing a high salt content.[45]

The SERS results in Figure 4 show an increase in the response of the spectral features diagnostic of the ERLs as FCV levels increase. The spectrum for the blank indicates the presence of a small but readily detectable level of nonspecific ERL binding. These responses also qualitatively follow the evolution of the AFM images in Figure 5 in that the number of captured viruses increase as the concentration of FCV increases. Moreover, the cross-sectional plot confirms the capture of FCV, which has a size of ~22 nm after extensive drying. We note that the differences between the size of the viruses based on its height with respect to its lateral dimension arise from tip convolution effects which can distort the lateral dimension of an imaged object.[46]

Figure 6 summarizes both sets of characterizations in the form of dose-response curves. The SERS data plots the $\nu_s(NO_2)$ intensity. In this plot, each data point is the average signal of five measurements from different locations on the same substrate and the standard deviations are represented by the error bars. The plot is linear over approximately three orders of magnitude. Though not shown, the response plateaus at a virus concentration of 2.5 x 10^8 viruses/mL. The limit of detection, defined as the concentration of FCV that yields a response equal to the blank signal plus three times the standard deviation of the blank, was determined to be 1 x 10^6 viruses/mL.

Finally, a comparison of the two different plots in Figure 6 provides a basis for validation of the SERS data. As is evident, the number of captured FCV, which was extrapolated from 25 μm^2 images to 500 μm^2 to approximate the area sampled in the SERS experiments, also undergoes a linear increase with concentration. The correlation between the two plots shows that for every captured virus, the SERS response is ~3 counts/s. The noise in the blank measured by SERS is 70 counts/s; therefore a signal of 210 counts/s above background is defined as the limit of detection. The correlation between the SERS signal and AFM data suggest that SERS signal at the limit of detection arises from the presence of ~70 captured viruses. In other words, we have the capability of detecting less than one hundred binding events, which is of immense value to the ultra-low level detection of viral pathogens and many other immunodiagnostic areas.

Conclusions

This report is the first demonstration of the low level detection of an intact viral pathogen in a sandwich immunoassay format based on a SERS readout method. This method, resulting in a limit of detection of 10^6 viruses/mL, is therefore competitive with other methods viral assays, such as fluorescence and microcantilevers, which have limits between 10^5 and 10^8 viruses/mL. Moreover, a SERS-based readout has greater facility in multiplexing for multi-virus detection. However, to fully realize this potential, approaches (e.g., operation at physiological temperatures[47] and modes to increase mass transfer[48]) are needed in order to reduce the time for both incubation steps. Experiments to this end are planned. We are also beginning to further investigate details related to the enhancement mechanism with respect to the possible plasmon coupling of the ERLs with the underlying gold substrate, along with the use of in situ AFM imaging to quantify the binding stoichiometry between the ERLs and captured viruses.

Acknowledgments

This work was supported through a grant from USDA-NADC and by the Institute for Combinatorial Discovery of Iowa State University. Jeremy Driskell would like to acknowledge the support of the Mary K. Fassel and Velmer A. Fassel Fellowship. The Ames Laboratory is operated for the U.S. Department of Energy by Iowa State University under contract W-7405-eng-82.

References

(1) Chomel, B. B. *J. Vet. Med. Educ.* **2003**, *30*, 145-147.

(2) Yoon, K.-J.; Department of Veterinary Diagnostic and Production Animal Medicine, College of Veterinary Medicine, Iowa State University: Ames, IA, 2004.

(3) Helps, C.; Lait, P.; Tasker, S.; Harbour, D. *J. Virol. Methods* **2002**, *106*, 241-244.

(4) Helps, C.; Harbour, D. *J. Virol. Methods* **2003**, *109*, 261-263.

(5) Sykes, J. E.; Allen, J. L.; Studdert, V. P.; Browning, G. F. *Vet. Microbiol.* **2001**, *81*, 95-108.

(6) Nettikadan, S. R.; Johnson, J. C.; Mosher, C.; Henderson, E. *Biochem. Biophys. Res. Comm.* **2003**, *311*, 540-545.

(7) Kjeldsberg, E. *J. Virol. Methods* **1986**, *14*, 321-333.

(8) Zheng, Y. Z.; Hyatt, A.; Wang, L.-F.; Eaton, B. T.; Greenfield, P. F.; Reid, S. *J. Virol. Methods* **1999**, *80*, 1-9.

(9) Donaldson, K. A.; Kramer, M. F.; Lim, D. V. *Biosens. Bioelectron.* **2004**, *20*, 322-327.

(10) Llic, B.; Yang, Y.; Craighead, H. G. *Appl. Phys. Lett.* **2004**, *85*, 2604-2606.

(11) Rohr, T. E.; Cotton, T.; Fan, N.; Tarcha, P. J. *Anal. Biochem.* **1989**, *182*, 388-398.

(12) Dou, X.; Takama, T.; Yamaguchi, T.; Tamamoto, H.; Ozaki, Y. *Anal. Chem.* **1997**, *69*, 1492-1495.

(13) Ni, J.; Lipert, R. J.; Dawson, B.; Porter, M. D. *Anal. Chem.* **1999**, *71*, 4903-4908.

(14) Grubisha, D. S.; Lipert, R. J.; Park, H.-Y.; Driskell, J.; Porter, M. D. *Anal. Chem.* **2003**, *75*, 5936-5943.

(15) Xu, S.; Ji, X.; Xu, W.; Li, X.; Wang, L.; Bai, Y.; Zhao, B.; Ozaki, Y. *Analyst* **2004**, *129*, 63-68.

(16) Mulvaney, S. P.; Musick, M. D.; Keating, C. D.; Natan, M. J. *Langmuir* **2003**, *19*, 4784-4790.

(17) Zhang, X.; Young, M. A.; Lyandres, O.; Van Duyne, R. P. *J. Am. Chem. Soc.* **2005**.

(18) Ansari, D. O.; Stuart, D. A.; Nie, S. *Proc. of SPIE* **2005**, *5699*, 82-90.

(19) Cao, Y. C.; Jin, R.; Mirkin, C. A. *Science* **2002**, *297*, 1536-1540.

(20) Graham, D.; Mallinder, B. J.; Whitcombe, D.; Smith, W. E. *ChemPhysChem* **2001**, *12*, 746-748.

(21) Graham, D.; Mallinder, B. J.; Whitcombe, D.; Watson, N. D.; Smith, W. E. *Anal. Chem.* **2002**, *74*, 1069-1074.

(22) Faulds, K.; Smith, W. E.; Graham, D. *Anal. Chem.* **2004**, *76*, 412-417.

(23) Faulds, K.; Barbagallo, R. P.; Keer, J. T.; Smith, W. E.; Graham, D. *Analyst* **2004**, *129*, 567-568.

(24) Kneipp, K.; Kneipp, H.; Itzkan, I.; Dasari, R. R.; Feld, M. S. *J. Phys.: Condens. Matter* **2002**, *14*, R597-R624.

(25) Park, H.-Y.; Lipert, R. J.; Porter, M. D. *Proc. SPIE* 2004; 464-477.

(26) Orendorff, C. J.; Gole, A.; Sau, T. K.; Murphy, C. J. *Anal. Chem.* **2005**, *77*, 3261-3266.

(27) Gillespie, J. H.; Scott, F. W. *Adv. Vet. Sci. Comp. Med.* **1973**, *17*, 163-200.

(28) Murphy, F. A.; Gibbs, E. P. J.; Horzinek, M. C.; Studdert, M. J. *Veterinary Virology*, 3 ed.; Academic Press: San Diego, 1999.

(29) Green, K. Y.; Ando, T.; Balayan, M. S.; Berke, T.; Clarke, I. N.; Estes, M. K.; Matson, D. O.; Nakata, S.; Neill, J. D.; Studdert, M. J.; Thiel, H. J. *J. Infect. Dis.* **2000**, *181*, S322-S330.

(30) Atmar, R. L.; Estes, M. K. *Clin. Microbiol. Rev.* **2001**, *14*, 15-37.

(31) James A. Baker Institute for Animal Health College of Veterinary Medicine Cornell University, 2004.

(32) Bidawid, S.; Malik, N.; Adegbunrin, O.; Sattar, S. A.; Farber, J. M. *J. Virol. Methods* **2003**, *107*, 163-167.

(33) Reed, L. J.; Muench, H. *Am. J. Hyg.* **1938**, *27*, 493-497.

(34) Wagner, P.; Hegner, M.; Kernen, P.; Zaugg, F.; Semenza, G. *Biophys. J.* **1996**, *70*, 2052-2066.

(35) Jones, V. W.; Kenseth, J. R.; Porter, M. D.; Mosher, C. L.; Henderson, E. *Anal. Chem.* **1998**, *70*, 1233-1241.

(36) Duhachek, S. D.; Kenseth, J. R.; Casale, G. P.; Small, G. J.; Porter, M. D.; Jankowiak, R. *Anal. Chem.* **2000**, *72*, 3709-3716.

(37) Geoghegan, W. D.; Ackerman, G. A. *J. Histochem. Cytochem.* **1977**, *25*, 1187-1200.

(38) Geoghegan, W. D. *J. Histochem. Cytochem.* **1988**, *36*, 401-407.

(39) Creighton, J. A. In *Surface Enhanced Raman Scattering*; Chang, R. K., Furtak, T. E., Eds.; Plenum Press: New York, 1982, pp 315-337.

(40) Stamou, D.; Gourdon, D.; Liley, M.; Burnham, N. A.; Kuik, A.; Vogel, H.; Duschl, C. *Langmuir* **1997**, *13*, 2425-2428.

(41) Kwarta, K. M.; Driskell, J. D.; Neill, J.; Ridpath, J.; Porter, M. D. *Manuscript in preparation.*

(42) Kumar, A.; Whitesides, G. M. *Appl. Phys. Lett.* **1993**, *63*, 2002-2004.

(43) Chen, C. S.; Mrksich, M.; Huang, S.; Whitesides, G. M.; Ingber, D. E. *Biotech. Prog.* **1998**, *14*, 356-363.

(44) Libioulle, L.; Bietsch, A.; Schmid, H.; Michel, B.; Delamarche, E. *Langmuir* **1999**, *15*, 300-304.

(45) Note: The dried reside that remains after a rinse with 150 mM NaCl upon completion of the ERL binding step inhibits the ability to image the presence of virus-bound ERLs by AFM. The problem persists even when reducing the NaCl concentration to 10 mM (see Figure 2). Other attempts to overcome this problem have so far proven unsuccessful. For example, while rinsing carefully with pure water does not result in the loss of captured viruses, the same process apparently leads to the loss of a significant fraction of virus-bound ERLs. We do not yet understand the origin of the loss.

(46) Montelius, L.; Tegenfeldt, J. O. *Appl. Phys. Lett.* **1993**, *62*, 2628-2630.

(47) Johnstone, R. W.; Andrew, S. M.; Hogarth, M. P.; Pietersz, G. A.; McKenzie, I. F. C. *Molec. Immunol.* **1990**, *27*, 327-333.

(48) Glaser, R. W. *Anal. Biochem.* **1993**, *213*, 152-161.

Figure Captions

Figure 1. UV-visible extinction spectra of colloidal gold (60 nm) before and after mixing with anti-FCV mAb (5-50 μg) for 1 h, followed by exposure to 150 mM NaCl.

Figure 2. AFM micrographs (5 x 5 μm) of FCV bound to an anti-FCV mAb capture substrate. These images were obtained after a 12-h exposure of capture substrates to a 5 x 10^8 viruses/mL solution in cell culture media and subsequent soaking for ~12 h in 2 mM borate buffer that also contained (A) 1, (B) 5, (C) 10, or (D) 150 mM NaCl.

Figure 3. SERS spectra for substrates labeled with ERLs suspended in borate buffer and phosphate buffer: (A) 2.5 x 10^8 viruses/mL in cell culture media and (B) blanks (i.e., cell culture media only) exposed to labeled nanoparticles in 2 mM borate buffer (pH 8.5) or 10 mM phosphate buffer (pH 7.4). Both buffers contained 150 mM NaCl and 1% BSA.

Figure 4. Results from the SERS-based immunoassay detection of FCV. SERS spectra (1-s integration) measured for various FCV concentrations: a) blank (cell culture media only), b) 5.0 x 10^5, c) 5.0 x 10^6, d) 5.0 x 10^7, e) 1.0 x 10^8, f) 2.5 x 10^8 viruses/mL. The spectra are offset for visualization.

Figure 5. AFM micrographs (5 x 5 μm) of FCV bound to capture substrates at three different concentrations. The images represent the number of FCV bound after exposure to a

virus solution of (A) 3×10^8, (B) 5×10^7, (C) 0 viruses/mL (blank cell culture media) (D) cross-sectional plot of line shown in (A).

Figure 6. Dose-response curves for SERS-based (circles) and AFM-based (squares) detection of FCV in cell culture media. The SERS calibration curve is constructed with the intensity of the nitro band at 1336 cm^{-1}. The SERS assays were run on duplicate samples, with each data point representing the average signal for five measurements from different locations on the same sample. Each AFM data point is the average number of FCV bound from five samples with five images per sample; the error is smaller than the data point.

Scheme 1

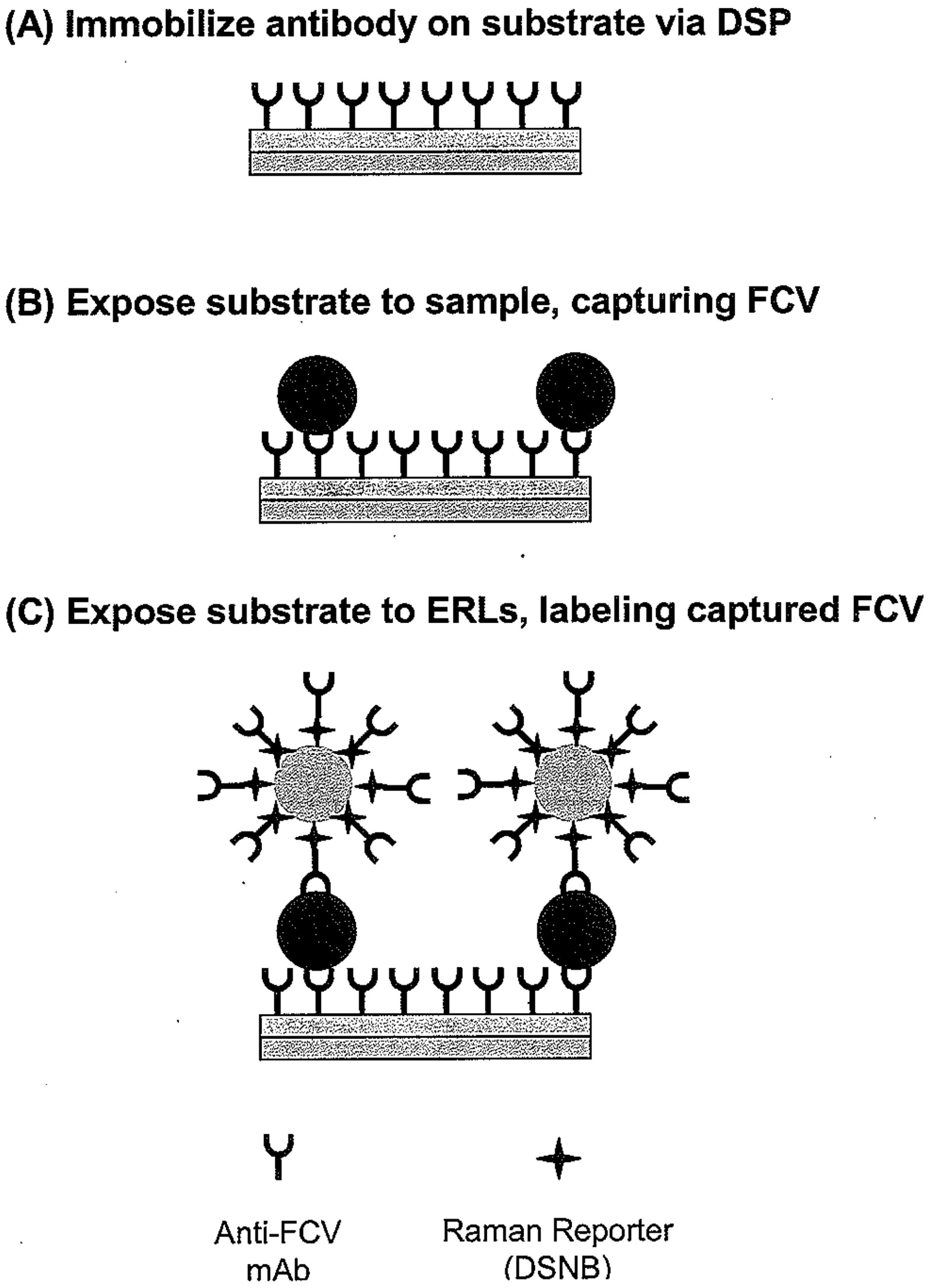
(A) Immobilize antibody on substrate via DSP
(B) Expose substrate to sample, capturing FCV
(C) Expose substrate to ERLs, labeling captured FCV
Anti-FCV mAb
Raman Reporter (DSNB)

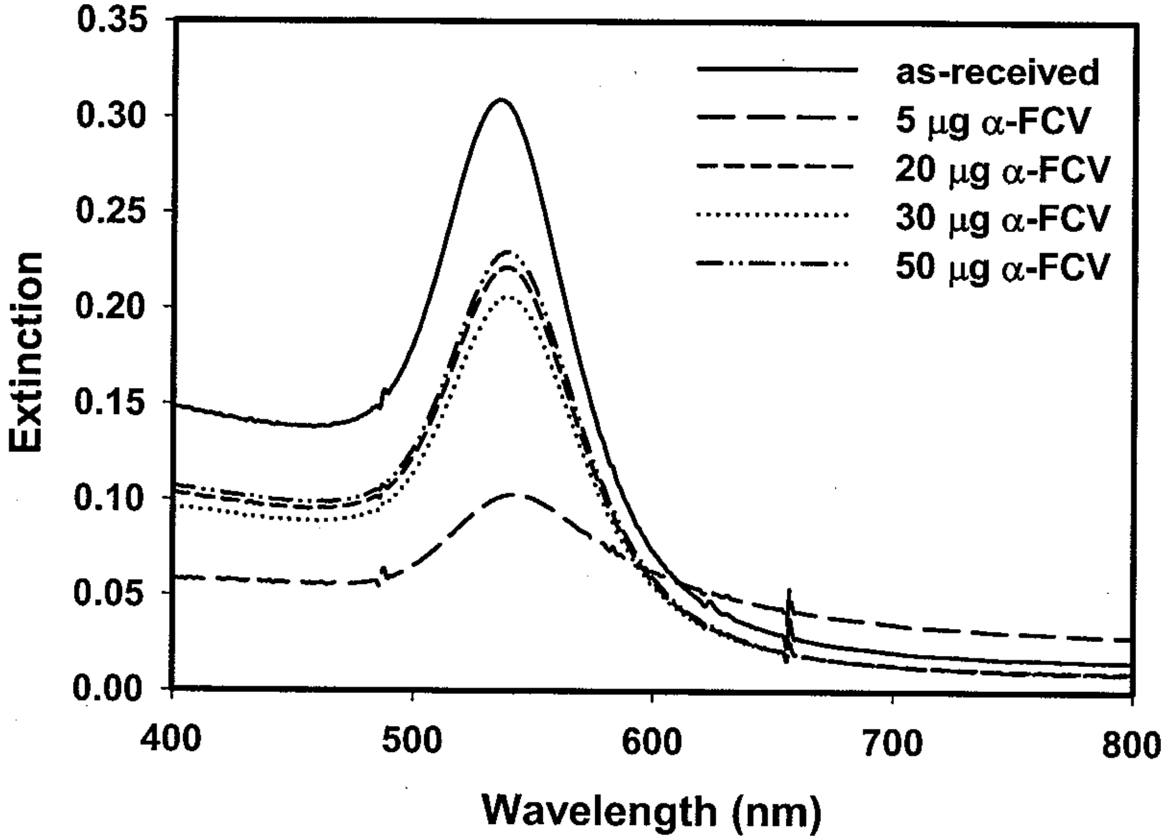
0.35
0.30
0.25
0.20
0.15
0.10
0.05
0.00
Extinction
400
500
600
700
800
Wavelength (nm)
as-received
5 μg α-FCV
20 μg α-FCV
30 μg α-FCV
50 μg α-FCV

Figure 1

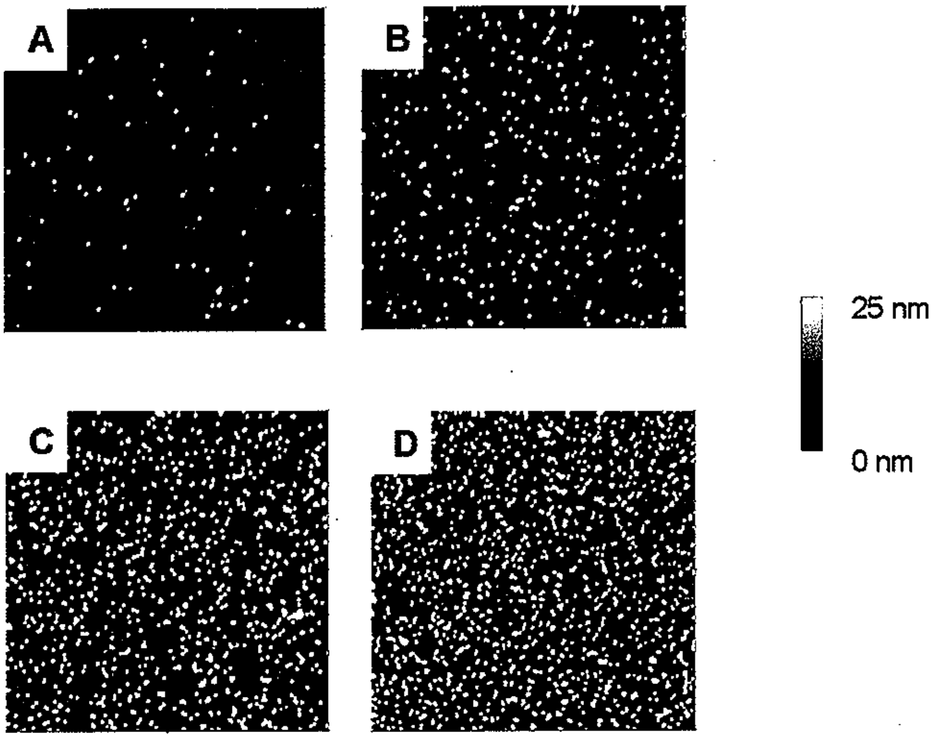

Figure 2

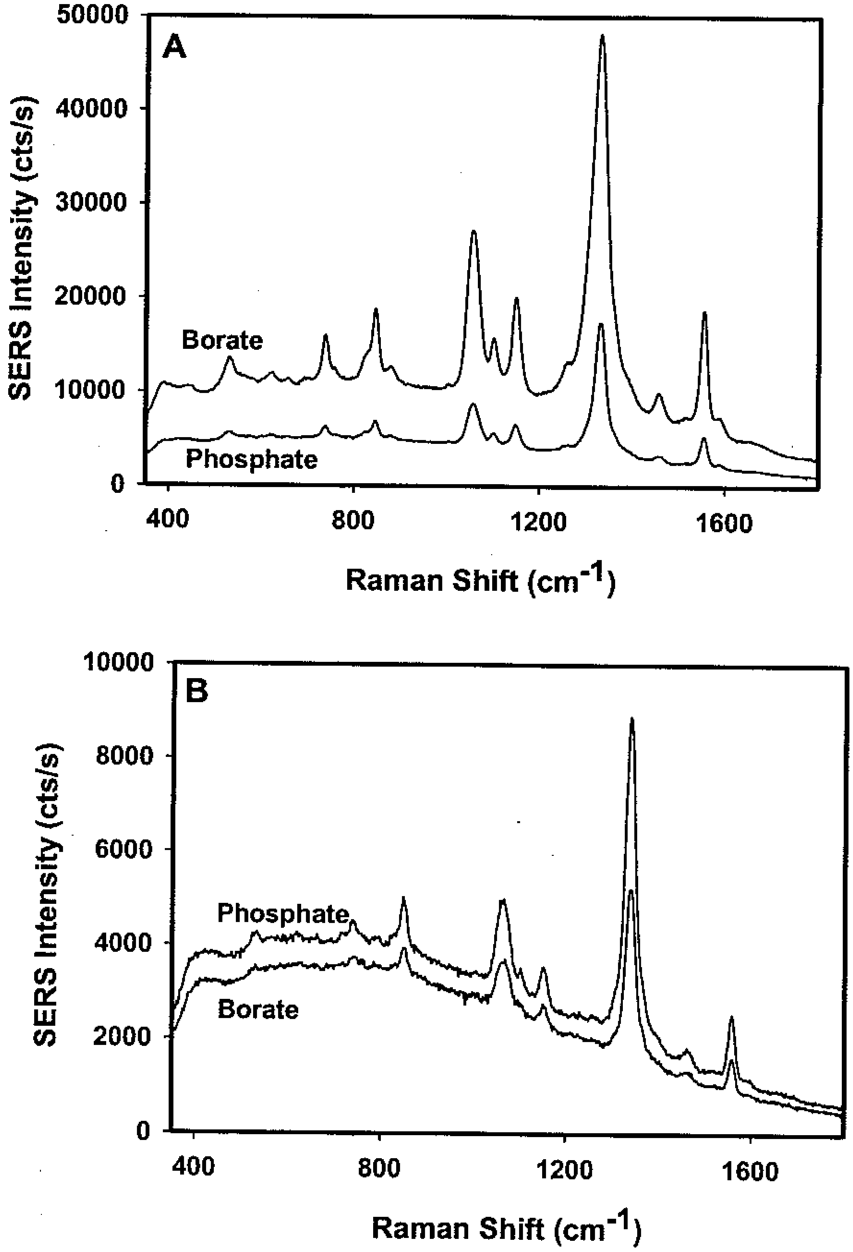
A
50000
40000
30000
20000
10000
0
SERS Intensity (cts/s)
Borate
Phosphate
400
800
1200
1600
Raman Shift (cm-1)
B
10000
8000
6000
4000
2000
0
SERS Intensity (cts/s)
Phosphate
Borate
400
800
1200
1600
Raman Shift (cm-1)

Figure 3

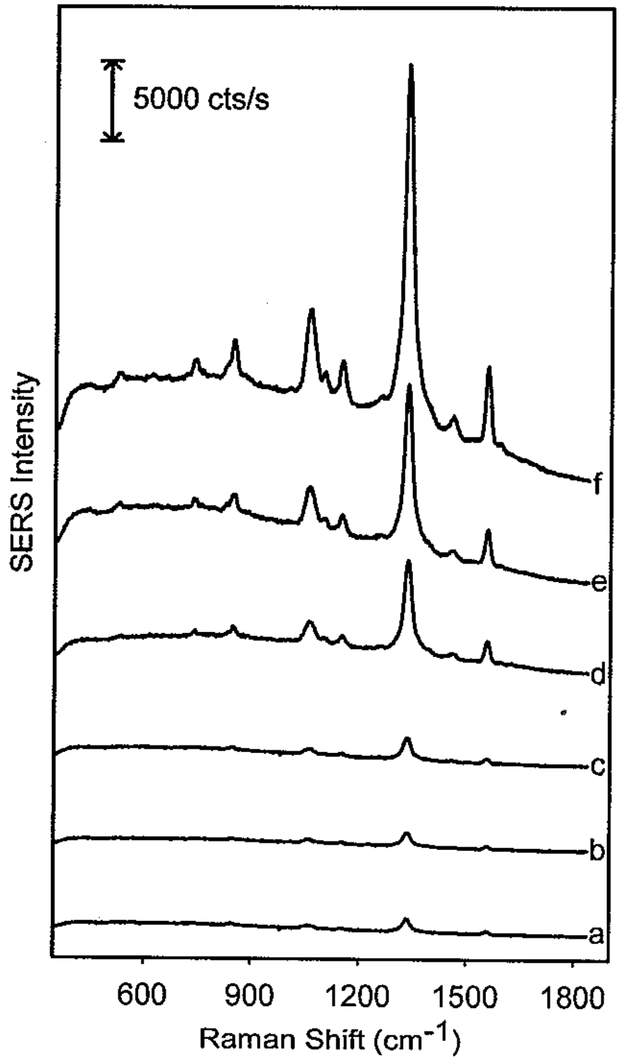
5000 cts/s
SERS Intensity
f
e
d
c
b
a
600
900
1200
1500
1800
Raman Shift (cm^{-1})

Figure 4

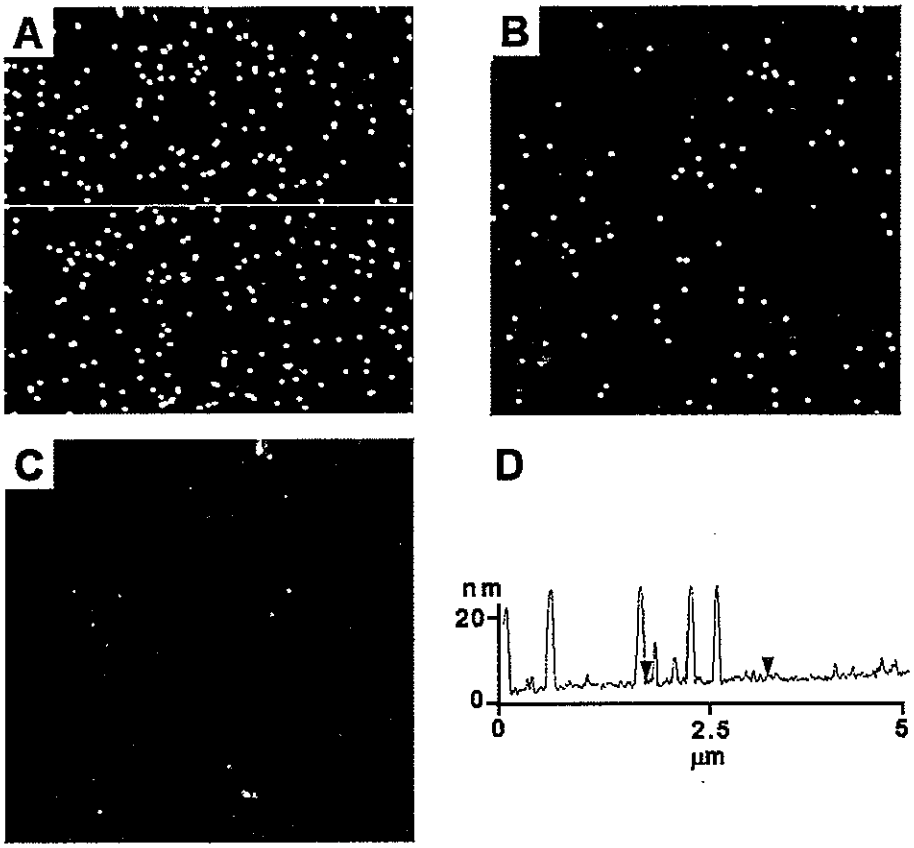

Figure 5

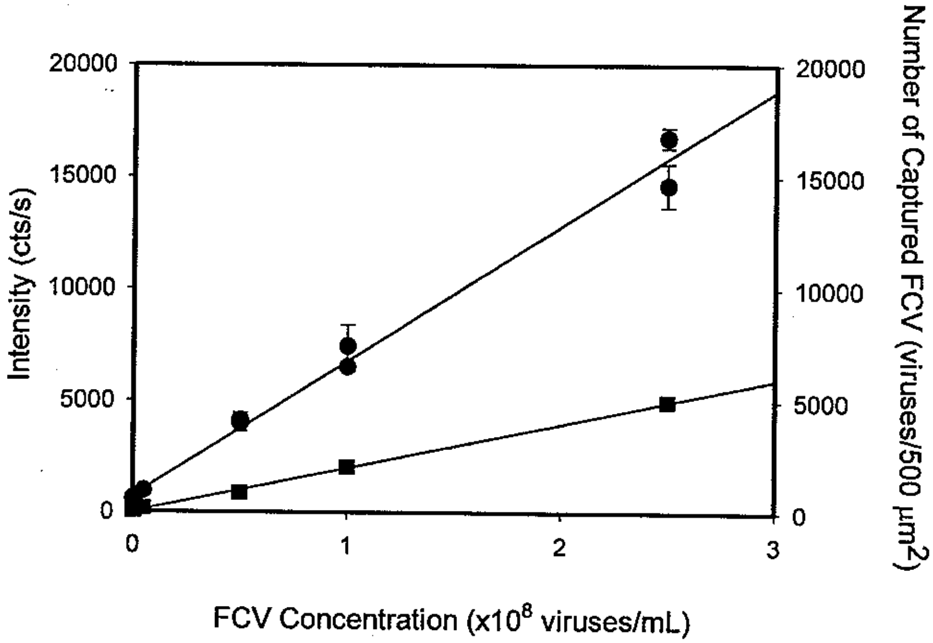
Intensity (cts/s)
20000
15000
10000
5000
0
Number of Captured FCV (viruses/500 μm^2)
20000
15000
10000
5000
0
0
1
2
3
FCV Concentration (x10^8 viruses/mL)

Figure 6

Supporting Information

Effect of Ionic Strength. The dependence on ionic strength is detailed further in Figure S-1, which plots the number of captured viruses in a 25-μm^2 image against NaCl concentration. Figure S-1 reveals that the number of FCVs bound to the substrate plateaus at ~1000 viruses/25 μm^2 when the salt concentration reaches ~10 mM. No significant differences in the number of captured viruses were found using higher salt concentrations. In contrast, lower ionic strength solutions resulted in fewer bound viruses.

Evaluation of Blocking Agents. In an effort to minimze the covalent attachment of the labeling antibody on the ERL to any unreacted succinimidyl esters remaining after capture antibody immobilization, three commonly used blocking agents were tested as "capping" additives: SuperBlock, StartingBlock and 1% BSA in 50 mM borate buffer (pH 8.5). SuperBlock and StartingBlock have a pH of 7.4. For this evaluation, different capture substrates were incubated with 20 µL of one of the blocking buffers, followed by exposures to cell culture media (without FCV) and to ERLs. Figure S-2 shows the spectroscopic results of this experiment. The blank signal was the lowest using SuperBlock and the largest using StartingBlock.

The same set of tests was carried out with the ERLs. The use of both SuperBlock and StartingBlock resulted in the irreversible aggregation of the ERLs, which is ascribed to the pH-induced instability found when attempting to suspend the particles in phosphate buffer. As a result, the ERLs were blocked with the 1% BSA solution, whereas the capture substrates were treated with SuperBlock.

Effect of Triton X-100 and Other Surfactants. The surfactants Triton X-100, Tween 20, and Tween 80 were also added to the ERL suspension in an effort to limit nonspecific binding between the mAbs of the capture substrate and ERLs. A portion of these results is presented by the SERS spectra in Figure S-3. Capture substrates were exposed to either a 2.5 x 10^8 viruses/mL solution of FCV or to blank cell culture media. The samples were then incubated with 20 μL of ERLs in 2 mM borate buffer (1% BSA, 150 mM NaCl) with or without 0.1% Triton X-100. Interestingly, while showing a clear difference in backgrounds, the strength of the SERS signal from the blank was marginally affected by the presence of Triton X-100, as shown in Figure S-3A. Figure S-3B, however, reveals that the ERL intensity was significantly lower for samples with captured viruses when Triton X-100 was used. This difference is ascribed to the affect of the surfactant on the capsid of the virus. The capsid of FCV is composed of 180 identical proteins that act as the selective recognition sites for mAb coupling. We believe that the surfactant disrupts the structure of the capsid, effectively denaturing the tertiary structure of the binding sites on the virus.

Other surfactants, such as Tween 20 and Tween 80, were also examined. In these cases, unfortunately, the addition of the surfactant lowered the surface tension of the ERL solution to a level sufficient to completely wet both the mAb capture address and the ODT confinement layer used for droplet localization. This spreading lead to an unacceptable degradation in the reproducibility of the assay and no further tests with surfactants were conducted.

Effect of Agitation and Optimization of Nanoparticle Concentration. For effective agitation, the volume of the ERL solutions was increased to 1.0 mL and the entire substrate was submerged in the resulting suspension. The disadvantage of using a large volume of nanoparticles is the increase in reagent consumption. Therefore, several dilutions of labeled nanoparticles were tested to determine the minimum concentration of nanoparticles necessary to saturate the captured FCV.

To this end, the capture substrates were first exposed to either FCV solutions (2.5×10^8 viruses/mL) or blank culture media. The substrates were then rinsed and incubated with 1.0-mL solutions of ERLs at varying concentrations (1.04×10^9 to 2.6×10^{10} ERLs/mL) on a rotary shaker (90 rpm). Figure S-4 plots the results from two trials; the error bars represent the standard deviation of the signal obtained from different locations on the same sample. Although exhibiting small differences between the two trials, the intensity of the $\nu_s(NO_2)$ for the FCV-treated substrates undergoes a gradual increase with increasing ERL concentration. The response reaches a maximum at $\sim 1.3 \times 10^{10}$ ERLs/mL, which corresponds to 23000-25000 cts/s. Importantly, the signal from the blank samples is much lower than that of the FCV-treated samples, reaching a maximum of only 525-570 cts/s at a concentration of 1.3×10^{10} ERLs/mL.

In comparison, the typical signal obtained under static conditions for FCV samples (2.5×10^8 viruses/mL) when performing the assay with 20 μL of ERLs (5.2×10^{10} ERLs/mL) is also ~25000 cts/s. This response is similar to that obtained with a larger volume (1.0 mL) of diluted nanoparticles (1.3×10^{10} ERLs/mL) with agitation. The value of agitation becomes evident, however, when examining the signals for the blank samples under static conditions, which ranged from 2000 to 5000 cts/s. Agitation therefore resulted in a significant decrease in the response from nonspecific binding. Agitation also improved the reproducibility of replicate assays. Since the blank signal showed only a weak dependence on ERL concentration, the overall reduction in the background is a direct consequence of sample agitation.

Supporting Figure Captions

Figure S-1. Dependence of the number of captured FCV on NaCl concentration. The data were obtained by imaging 5 x 5 μm areas of samples after exposure to 2 mM borate buffer and varied concentrations of NaCl for ~12 h. Each data point represents the average FCV density from five images and the error bars represent the standard deviations.

Figure S-2. SERS spectra demonstrating the influence of blocking buffer on the SERS response from the nonspecific binding of nanoparticles to blank substrates.

Figure S-3. SERS spectra demonstrating the influence of Triton X-100 on the binding of the ERLs to the capture substrates. (A) Blanks and (B) 2.5 x 10^8 viruses/mL exposed to ERLs in 2 mM borate buffer that contained 150 mM NaCl or 150 mM NaCl and 0.1% Triton X-100.

Figure S-4. SERS intensities of $\nu_s(NO_2)$ as a function of ERL concentration. The samples were exposed to 1.0 mL of ERLs under agitation. The results form two trials are plotted and the error bars represent the standard deviation of the signal obtained from different locations on the same sample.

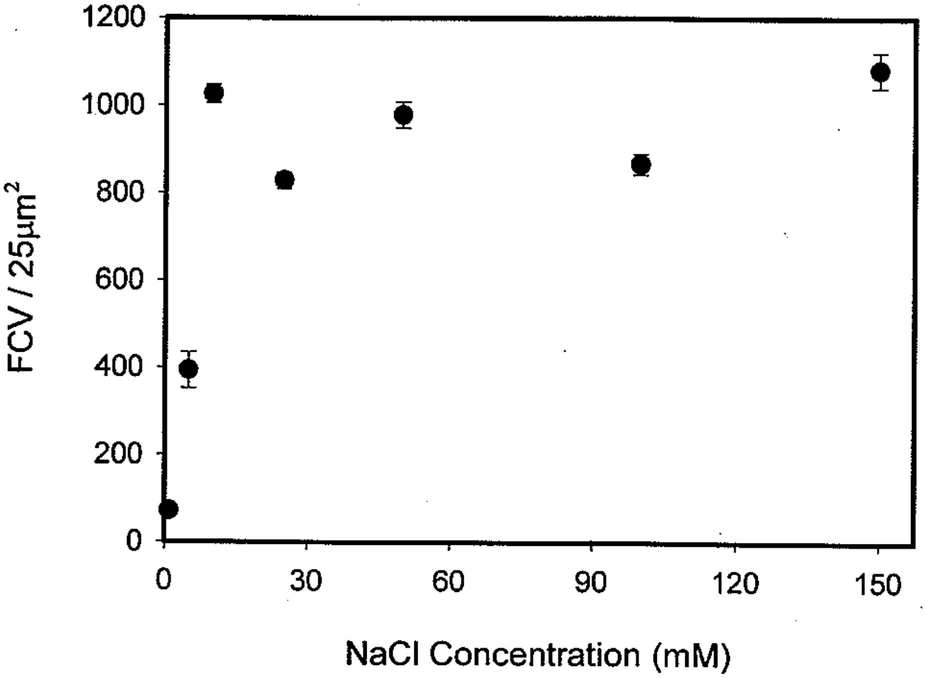
1200
1000
800
600
400
200
0
FCV / 25μm^2
0
30
60
90
120
150
NaCl Concentration (mM)

Figure S-1

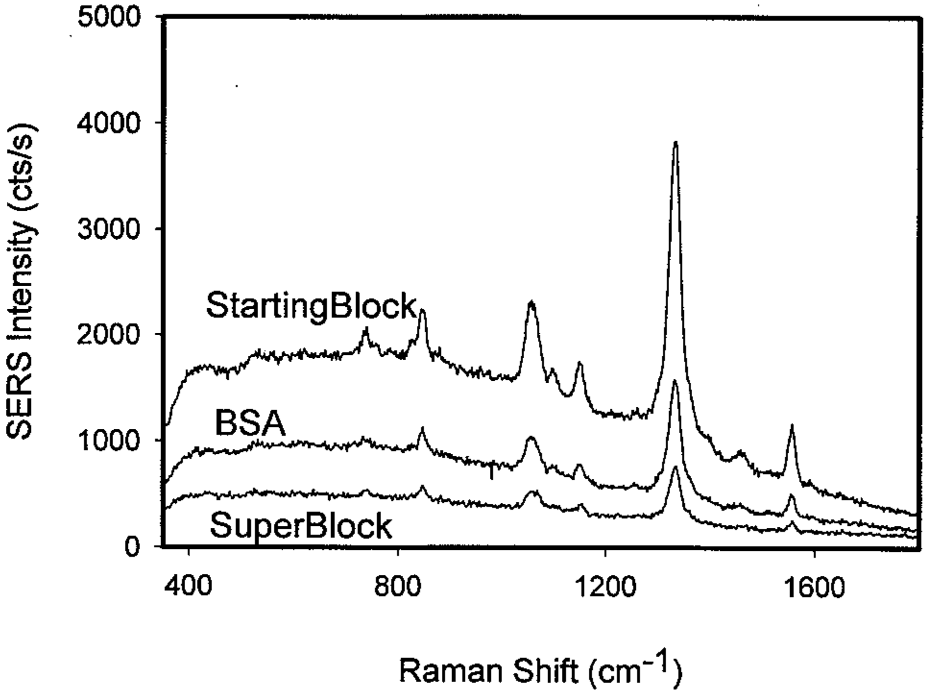
SERS Intensity (cts/s)
5000
4000
3000
2000
1000
0
StartingBlock
BSA
SuperBlock
400
800
1200
1600
Raman Shift (cm-1)

Figure S-2

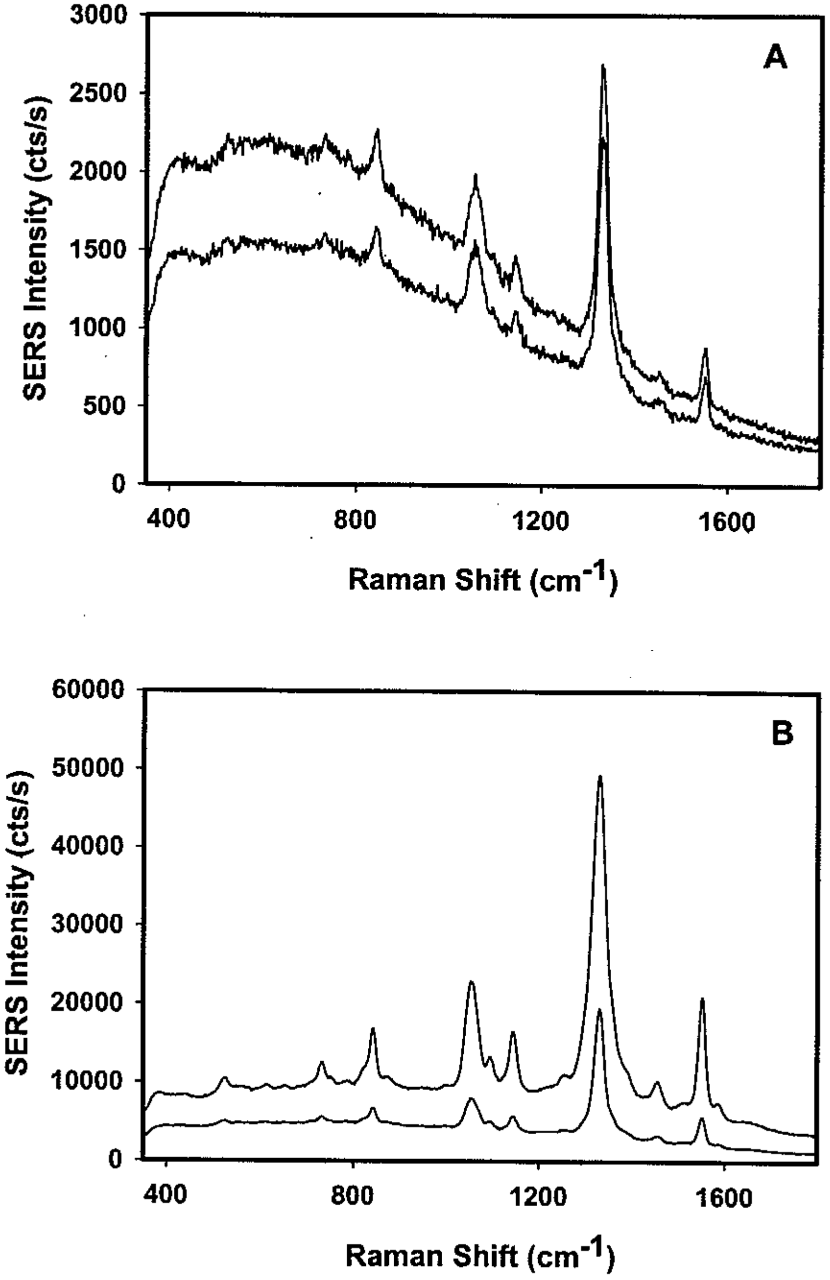
A
SERS Intensity (cts/s)
3000
2500
2000
1500
1000
500
0
400
800
1200
1600
Raman Shift (cm^{-1})
B
SERS Intensity (cts/s)
60000
50000
40000
30000
20000
10000
0
400
800
1200
1600
Raman Shift (cm^{-1})

Figure S-3

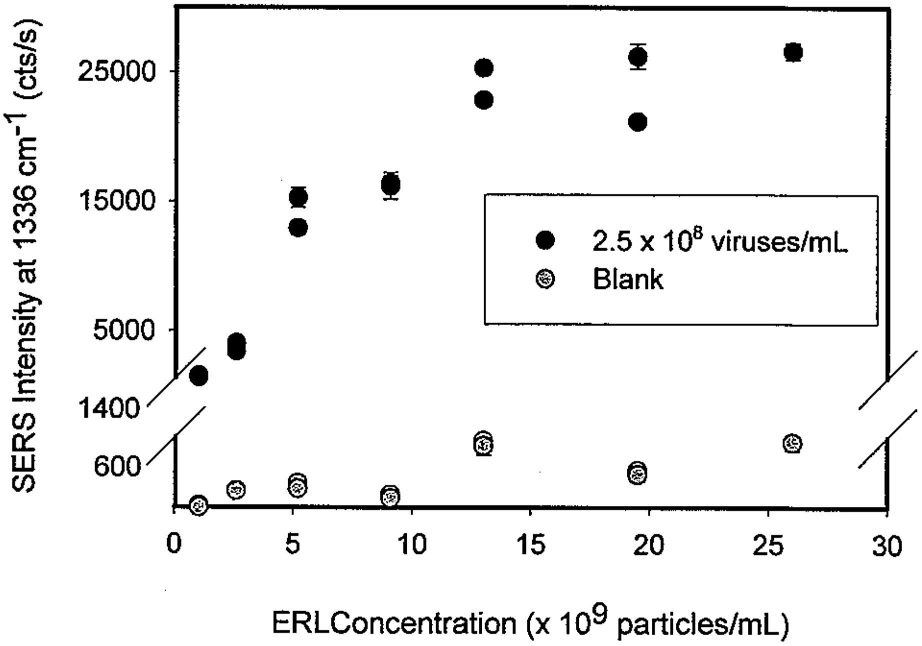
SERS Intensity at 1336 cm^{-1} (cts/s)
25000
15000
5000
1400
600
0
5
10
15
20
25
30
ERLConcentration (x 10^{9} particles/mL)
● 2.5 x 10^{8} viruses/mL
◎ Blank

Figure S-4

CHAPTER 3: LABELED GOLD NANOPARTICLES IMMOBILIZED NEAR METALLIC SUBSTRATES: SYSTEMATIC INVESTIGATION OF SURFACE PLASMON RESONANCE AND SURFACE-ENHANCED RAMAN SCATTERING

A paper submitted to *Journal of Physical Chemistry B*

Jeremy D. Driskell, Robert J. Lipert, and Marc D. Porter

Iowa State University, Institute for Combinatorial Discovery, Departments of Chemistry and of Chemical and Biological Engineering, Ames Laboratory-U.S. DOE, Ames, IA 50011-3020

Abstract

This paper systematically investigates the influence of an underlying metallic substrate (i.e., gold and silver) on the surface plasmon resonance (SPR) of labeled gold nanoparticles, from both experimental and theoretical perspectives, and the concomitant impact on the surface-enhanced Raman scattering (SERS) signal from the labels. These experiments employ nanoparticles of varied sizes (30-100 nm) that are coated with a bifunctional Raman scatterer composed of: 1) a disulfide for chemisorption to the nanoparticle surface; 2) a succinimidyl ester for formation of a covalent linkage to an amine-terminated self-assembled monolayer on the underlying substrate; and 3) an aryl nitro group with an intrinsically strong Raman active vibrational mode. This approach allows facile systematic assessments of how variations in nanoparticle size, substrate composition, and the

gap between the nanoparticle and substrate affect the SPR of the bound particles. Both UV-VIS transmission and reflection absorption (incident angle of 58°) spectroscopy are used to characterize the effect of each of these parameters on SPR. These results are then correlated with SERS enhancement factors that were determined by accounting for particle surface concentrations, which were measured by atomic force microscopy, and the absolute number of labels, which were calculated based on the surface area of each of the different-sized particles. All SERS spectra were collected at an incident angle of 58° with respect to the surface normal. As expected, the SPR for particles in solution red shifts with increasing particle size. More importantly, the SPR moves to even longer wavelengths as the size of immobilized particles increases, and as the gap between the immobilized particle and substrate decreases. The red shift is also greater for a gold nanoparticle tethered to a gold substrate compared to a silver substrate. A theoretical model for the extinction of a particle above a flat substrate, corrected for surface scattering, radiation damping, and dynamic depolarization is also briefly detailed. SPR results calculated with the model are consistent with the shifts observed in the SPR position for each of the manipulated experimental variables. The largest SERS enhancement factors are found for samples with an SPR maximum (λ_{max}) between the wavelengths for laser excitation (633nm) and the Raman band for the symmetric nitro stretch of the particle coating (690 nm). As an example, an order of magnitude in the SERS enhancement factor is gained for a 60-nm particle immobilized 1.2 nm above a gold substrate (SPR λ_{max} = 657 nm) compared to that for a 30-nm particle (SPR λ_{max} = 596 nm).

Introduction

Surface modified gold nanoparticles have recently been developed to function as analytical reagents in ultra sensitive bioassays based on surface enhanced Raman scattering (SERS).[1-15] In our laboratory, antigens captured by antibody-modified gold surfaces are detected using Raman reporter-labeled gold nanoparticles. These particles, which we have termed extrinsic Raman labels (ERLs), are prepared by the sequential immobilization of an intrinsically strong Raman scatterer, followed by that of a molecular recognition moiety (i.e., antibody). ERLs with 30-nm diameter gold particles were originally employed.[3, 7] However, we have recently shown that larger diameter particles (e.g., 60 nm) lead to lower limits of detection.[12, 13] In view of the widespread interest in this assay strategy,[1-15] it is of fundamental and technological importance to gain insights into the mechanism that leads to this observation.

Although not fully understood at a quantitatively predictable level, the majority of the enhancement in SERS originates from large local electric fields at surfaces with nanometer-sized asperities that arise from excitation of surface plasmons.[16] Many studies have therefore focused on the development of theories that can be used in conjunction with experimental techniques that manipulate the surface plasmon resonance (SPR) at roughened substrates in order to determine the underpinning relationships between SPR and SERS.[17-26] The combined weight of these efforts has firmly established that the location of the SPR depends on the size, shape, spacing, and composition of the nanometric features, as well as the dielectric properties of the surrounding medium.[27-30]

As noted, a great deal of effort has been placed on the development of substrates that allow facile manipulation of the parameters that influence SPR in order to develop and refine our understanding of the relationship between SPR and SERS. Early work was performed with colloids,[17, 18] island films,[19, 20] grating-type substrates,[21] and metal coated SiO_2 posts.[22] More recently, nanoparticle arrays fabricated with nanosphere lithography[23, 24, 28, 31] and electron beam lithography[25, 26] have been utilized. These approaches, to varying degrees, have been applied to probe the theoretical links between SPR and SERS. This work has shown that the coupling of the localized fields between nanostructures not only results in an amplified field between the asperities, but also shifts the localized surface plasmon resonance to longer wavelengths, both of which have a profound influence on the SERS enhancement factor.[31-38]

The conduction electrons in bulk smooth metal films can also be excited to generate propagating electromagnetic waves at the surface called surface plasmon polaritons. Much like the interparticle interactions, surface plasmon polaritons can couple to the surface plasmons of nearby nanoparticles, shifting and enhancing the resulting electromagnetic field.[33, 39-44] Theoretical treatments indicate that the SPR for such systems will be strongly dependent on nanoparticle-substrate spacing and substrate composition, in addition to nanoparticle size, shape, composition, and dielectric constant of the ambient.[45-47] At present, however, there is limited experimental evidence to directly support these predictions.[47]

This paper introduces and applies a model system for the experimental investigation of the influence of the dielectric properties of the underlying substrate and spacing between the nanoparticle and substrate on the SPR of the nanoparticle. We then examine these findings within the context of extended theoretical treatments,[46, 47] which consider the effects of surface scattering, radiation damping, and dynamic depolarization. To this end, gold nanoparticles labeled with a bifunctional Raman-active self-assembled monolayer are captured using a functionalized self-assembled monolayer on a gold or silver substrate. The monolayer on the substrate acts as a coupling agent and as a spacer to control the gap between the particle and substrate. This methodology therefore enables a systematic assessment and comparisons to theoretical predictions of the impact of particle size, the separation between the substrate and particle, and the composition of the substrate on SPR by using UV-VIS reflection spectroscopy. These results are then correlated with measured SERS enhancement factors that were evaluated considering particle surface concentrations, determined using atomic force microscopy (AFM), and the number of scatterers, approximated by the particle surface area. This paper concludes with a discussion of the relationship between the wavelength of the SPR maximum and SERS enhancement factor and its implication for designing an optimized SERS-based analytical assay.

Experimental

Reagents. Gold colloids with nominal diameters of 30 (2.0×10^{11} particles/mL), 50 (4.5×10^{10} particles/mL), 60 (2.6×10^{10} particles/mL), 80 (1.1×10^{10} particles/mL), and 100 nm (5.6×10^{9} particles/mL) were purchased from Ted Pella. The vendor-specified dispersity of the particle size was less than 8%. N-hydroxysuccinimide (NHS), 1,3-dicyclohexylcarbodiimide (DCCD), 5,5′-dithiobis(2-nitrobenzoic acid) (DNBA), Triton X-100, and 2-aminoethanethiol hydrochloride (AET) were obtained from Aldrich. 11-Amino-1-undecanethiol hydrochloride (AUT) was acquired from Dojindo Laboratories. Borate buffer packs (50 mM) were purchased from Pierce Biotechnology, and diluted as needed. The synthesis of 5,5′-dithiobis(succinimidyl-2-nitrobenzoate) (DSNB) is described elsewhere.[7]

Preparation of Substrates. Template-stripped gold and template-stripped silver were used as substrates because their low roughness factors facilitated enumeration of particle surface concentration by AFM. These substrates were prepared by the resistive evaporation of ~300 nm of gold (99.9% purity) or silver (99.9% purity) onto a 4-in p-type silicon [111] wafer (University Wafer) at a rate of 0.1 nm/s with an Edwards 306A metal evaporator. Glass microscope slides were cut into ~1 x 2 cm chips and cleaned by sonicating in dilute surfactant solution (Micro, Cole-Parmer), deionized water, and ethanol, each for 30 min. The clean glass chips were bonded to the gold- or silver-coated silicon wafer using two-part epoxy immediately upon removal from the evaporator. The epoxy was then cured at 150°C for 2 h and allowed to cool. The glass chips were then carefully detached from the silicon wafer, exposing a smooth (RMS roughness ~0.6 nm) gold or silver surface.

Monolayers were formed by immersing a gold or silver substrate in a 1.0 mM AET or AUT ethanolic solution for 8-12 h. The substrates were then removed from the thiol solution, rinsed with ethanol, and dried with a stream of high purity nitrogen.

Preparation of Raman Reporter-Labeled Gold Nanoparticles. DSNB was used as the Raman reporter molecule due to the large intrinsic Raman scattering cross-section of its symmetric NO_2 stretch and its bifunctional reactivity. DSNB forms a thiolate coating on the gold nanoparticles through cleavage of its disulfide moiety, while its succinimidyl ester functional group can react with primary amines to form an amide linkage. The bifunctionality is of particular importance for immobilizing the nanoparticles to amine-modified substrates.

Each set of particles was modified by a multi-step procedure. First, 1.0 mL of gold colloid solution was centrifuged at 2000*g* for 10 min, the supernatant discarded, and the nanoparticles resuspended in 1.0 mL of 2 mM borate buffer (pH 8.5) containing 0.1% Triton

X-100. Following resuspension, 100 µL of a 1.0 mM DSNB solution in acetonitrile was added to the colloid suspension and the mixture reacted for 8-12 h. Next, excess DSNB was removed by centrifuging at 2000*g* for 10 min and decanting the supernatant. The product was again resuspended in 2 mM borate buffer (pH 8.5) containing 0.1% Triton X-100. The centrifugation/resuspension process was performed a total of three times for thorough removal of excess DSNB. The surfactant aided the dissolution of DSNB and the stability of the colloidal suspension without inhibiting the immobilization of the particles to the amine-modified substrates. The concentration and pH of the buffer used for resuspension reflect conditions requisite to avoid particle aggregation and to ensure the presence of deprotonated amines on the modified substrate for reaction with the DSNB-labeled nanoparticles.

The Raman reporter-labeled nanoparticles were passed through a 0.22-µm syringe filter to remove aggregates. The thiolate coated substrates were then fully immersed in the labeled nanoparticles and allowed to react for 8-12 h. Finally, the prepared substrates were rinsed with deionized water and dried with a stream of high purity nitrogen.

Instrumentation. (i) SERS Measurements. Raman spectra were collected with a NanoRaman I (Concurrent Analytical). This instrument is equipped with a 632.8 nm He-Ne laser with an incident power of 30 mW. The spectrograph has a resolution of 6-8 cm^{-1} and consists of an f/2.0 Czerny-Turner imaging spectrometer. The CCD (Kodak 0401E) is thermo-electrically cooled to 0°C. SERS spectra of the Raman-reporter labeled nanoparticles, after their immobilization on a substrate, were obtained by focusing the laser light on the surface at an angle of incidence 58° from the surface normal, using an objective with a 6.1-mm focal length and a numerical aperture of 0.40. The irradiated area on the surface is ~ 4000 µm^2. The same objective was used to collect the scattered light. The SERS spectra of the nanoparticle suspensions were obtained with the same instrument by focusing the laser light into a quartz cuvette. All spectra were integrated for 1 s.

(ii) UV-VIS Spectroscopy. UV-VIS extinction spectra were collected in an external reflection mode with a Hewlett-Packard 8453 spectrophotometer. Spectra were obtained with *p*-polarized, *s*-polarized, or unpolarized light incident at ~58° with respect to the surface normal, and integrated for 0.5 s at a resolution of 1 nm. The results are presented as $-\log(R/R_0)$, where R is the reflectance of the sample substrate and R_0 is the reflectance of an uncoated template-stripped gold or template-stripped silver reference substrate. In most cases, the experimentally determined extinction spectra are presented after normalization with respect to their individual extinction maximum.[31] This approach arises from two factors. First, the substrates are smaller than the light beam (1.5 cm) and not uniform in size, which led to sample-to-sample variability in the amount of reflected light. Second, we did not attempt to control the surface concentration of the immobilized nanoparticles. These factors resulted in the inability to interpret the magnitude of extinction as due only to differences in SPR. There is, however, no effect on the position of the extinction maximum, and the use of normalization facilitates comparisons of peak positions.

(iii) AFM Imaging. The nanoparticle surface concentration on each substrate was measured with a Dimension AFM (Digital Instruments). The AFM was operated in TappingMode at a scan rate of 1.5 Hz, maintaining a constant setpoint oscillation amplitude at 80% of the free amplitude. The n(+)-silicon TESP probes (Nanosensors) used for imaging were 118 μm long, 27-29 μm wide, and 3.6-4.5 μm thick, with a spring constant of 32-70 N/m and a resonant frequency of 327-421 kHz.

Images (5 x 5 μm) were collected on five different areas of each sample, with the number of nanoparticles in each image enumerated manually and then averaged for each sample. There was no indication of aggregation of labeled particles dispersed in solution, based on the UV-VIS extinction spectra. Moreover, there was no evidence for particle aggregation in the AFM images.

Theory

Earlier approaches to the calculation of the polarizability of a nanosphere above a flat substrate of semi-infinite thickness employed the dipole approximation.[47] This calculated polarizability was then used to model an extinction spectrum. However, results showed that higher-order multipoles must be considered in order for the calculated polarizability of the particle to be reliable in predictions of the experimentally observed extinction spectrum.[47] Both Aravind and Wind each developed methods to solve the Laplace equation for this system that includes the effects of multipoles.[45, 46] Both models give identical solutions, but utilize different coordinate systems. The key points of Wind's model are briefly described.

According to Wind's model, the polarizability of the nanoparticle is influenced by the dielectric functions of the ambient, underlying substrate, and nanoparticle; the nanoparticle radius; the nanoparticle-substrate separation; and the incident angle of the radiating source. In addition, the polarizability of a nanoparticle above a substrate is dependent upon the polarization of the incident light. That is, an electric field polarized perpendicular to the substrate will induce an image charge distribution of the bound particle in the substrate that is in phase with that induced in the nanoparticle. The resulting image charge will increase the polarization of the particle. When the incident field is polarized parallel to the surface, however, the image charge is opposed to the induced charge distribution of the nanoparticle and therefore reduces the polarization of the particle.

As a starting point, we calculated extinction spectra for gold nanoparticles suspended in close proximity to a flat gold substrate using Wind's method to determine polarizability. However, those results did not agree well with the experimental observations. Work with isolated spherical particles has shown that surface scattering effects,[48] radiation damping, and dynamic depolarization[49] must be considered to account for size effects. In search of better agreement between experimental and theoretical results for our system, we have incorporated these corrections for size effects into Wind's method. We found that for the size of particles used in our studies (30-100 nm), surface scattering effects are small, and the correction factor is dominated by consideration of radiation damping and dynamic depolarization.

Results and Discussion

1. Measurements of the SPR for Immobilized Gold Nanoparticles. The above model predicts that particle size (*r*), gap distance (*d*), and dielectric functions of the nanoparticle (ε_3), substrate (ε_2), and ambient (ε_1) will all have an effect on the extinction spectrum of immobilized nanoparticles. In this section, we explore the role of these factors and demonstrate control over SPR by experimentally varying *r*, *d*, and ε_3. The experimental results are then compared to predictions by the model.

1.1 Effect of Nanoparticle Immobilization and Size on SPR. Figures 1-3 present a series of experimental spectra that begins to reveal the plasmon interactions between the immobilized gold nanoparticles and the underlying gold substrate. Each spectrum in Figures 1 and 2 is normalized with respect to its maximum extinction to highlight the wavelength shifts. The extinction spectra of the five sizes of DSNB-labeled gold nanoparticles, all suspended in borate buffer (pH 8.5), are shown in Figure 1. The extinction maxima undergo a red shift from 529 to 565 nm as the nanoparticle diameter increases from 30 to 100 nm. These shifts follow expectations of the wavelength dependence of SPR on particle size.[50] The peak widths are also observed to increase with particle diameter, which in addition to the effects of dynamic depolarization and radiation damping, results from a greater absolute size distribution for larger particles.

Figure 2 shows the *p*-polarized extinction spectra for the same set of DSNB-labeled gold nanoparticles after immobilization on gold substrates that were previously modified with an AET spacer and then dried under a stream of high purity nitrogen. The observed relationship between nanoparticle size and the wavelength of the extinction maximum for the immobilized nanoparticles follows the same trend found for the suspended nanoparticles. Further comparisons of the two sets of spectra reveal a much larger red shift in the extinction maximum for each size of immobilized nanoparticles. As a consequence of immobilization, the extinction maxima move from 596 to 755 nm as the particle diameter increases from 30 to 100 nm. Immobilization therefore shifts the extinction maximum of the 30-nm particles by almost 70 nm. The change is even more dramatic upon immobilization of the 100-nm particle, ~190 nm.

These shifts are only observed when the incident light is *p*-polarized. As shown in Figure 3, there is no detectable shift in the extinction spectra collected for the same samples with *s*-polarized light. The feature at ~530 nm in Figure 3 is also observed in Figure 2, where it results from the component of the *p*-polarized light that is parallel to the surface. We further note that this band arising from the parallel component of the electric field is blue shifted for the immobilized particles compared to that of the suspended particles because of differences in the dielectric constant of the surrounding media (air vs. water).

The above findings support the existence of a strong coupling interaction between the polarized nanoparticle irradiated with *p*-polarized light and the image charge formed in the underlying gold substrate. This interaction results in a large shift in the plasmon resonance of the system. Since the electric field for *s*-polarized light is in the plane of the substrate, the induced image charge opposes that of the particle and markedly dampens polarization.

1.2 Effect of Gap Distance on SPR. The above results show that coupling between a nanoparticle and a smooth gold surface in close proximity can have a dramatic effect on the SPR of the gold nanoparticles and that particle size can serve as a potential control parameter to vary SPR. Moreover, theory predicts that the location of the SPR maximum is extremely sensitive to nanometric differences in the separation between the substrate and nanoparticle. To test this prediction, the particle-substrate separation, *d*, was varied by using AET and AUT, which form gold-bound thiolates with different chain lengths. As such, a DSNB-labeled nanoparticle bound to the substrate via AET yielded a gap of ~1.2 nm, while that bound to the substrate via AUT gave a gap of ~2.3 nm; both values are based simply on CPK modeling (Harvard Apparatus) and include both the thickness of the spacer and DSNB.

Unpolarized UV-VIS spectra comparing 60-nm DSNB-labeled nanoparticles immobilized on a gold substrate with AET and AUT are shown in Figure 4. The spectrum for the particle suspension is included, a situation analogous to an infinite gap.[51] The 60-nm nanoparticle has an extinction maximum at 539 nm in solution, 611 nm when bound to AUT, and 657 nm when linked to AET. The red shift is therefore 71 nm when the nanoparticles are brought to within 2.3 nm of the surface and increases an additional 46 nm when the gap is reduced by 1.1 nm. Red shifts were also observed for the same reduction in gap distance with each of the different sizes of nanoparticles. These results are summarized as part of Table 1. We therefore find that the SPR for this system is very sensitive to the gap distance, which further supports the existence of nanoparticle-substrate coupling given that greater changes in SPR are detected as the separation decreases. Thus, gap distance, like nanoparticles size, can serve as another parameter for manipulation of SPR.

1.3 Effect of Substrate Material on SPR. Theoretical models also indicate that SPR of a nanoparticle suspended over a flat substrate is dependent upon the dielectric function of the substrate. To experimentally probe this prediction, the gap between the particle and substrate was held effectively constant by using an AET monolayer for particle immobilization, but the underlying substrate is switched from gold to silver. It is known, however, that the thiolate chain tilt is ~30° on gold and ~10° on silver,[52] which would translate to gaps of 1.2 nm and 1.3 nm, respectively. Figure 5 shows the resulting UV-VIS spectra, collected using unpolarized incident light and normalized with respect to their extinction maximum, for 60-nm DSNB-labeled gold nanoparticles. In both cases, there is a strong shift in the extinction maximum to longer wavelengths with respect to that at 539 nm for the nanoparticle suspension. The extinction maximum for a 60-nm nanoparticle on silver appears at 617 nm, whereas that on gold is at 657 nm. The shift at gold is therefore ~40 nm larger than at silver. The same types of dependencies were found for each size of tested nanoparticles (Table 1); the extinction peak for a given nanoparticle size and gap distance is located at longer wavelengths when bound to a gold substrate compared to a silver substrate. Thus, the choice of substrate is a third method of controllably tuning SPR.

2. Calculation of the Extinction Spectra of Immobilized Gold Nanoparticles.

Extinction spectra were calculated, as discussed above, to investigate the expected influences of nanoparticle size, nanoparticle-substrate separation, and substrate material and for comparison to our experimental findings. The polarizability was calculated using the first 40 terms in the infinite series solution to Wind's model[53] and corrected for radiation damping and dynamic depolarization.[49] The values for the wavelength dependent dielectric function of the nanoparticles were taken from literature,[54] interpolated to 1-nm increments, and corrected for surface scattering effects.[55] However, a determination of a value for the dielectric constant of the ambient (ε_1) proved difficult because the particles were coated with a thiolate monolayer and separated from the substrate by another thiolate monolayer. Our approach was to test various values for ε_1, which would then represent a single effective dielectric constant incorporating the contribution of the thiolate layers for the system in which 30-nm particles are immobilized on a gold substrate via AET, and surrounded by air. This empirical approach established that an ε_1 of 1.21, a value that reasonably lies between those of air and condensed hydrocarbon phase, produced similar predicted and measured locations of the plasmon resonance peak. This value of ε_1 was then employed in the calculations for all our systems, using the vendor-specified sizes for the nanoparticles, the CPK modeled gap distance, and an incident angle of 58°.

First, the influence of immobilizing gold nanoparticles on a gold substrate was studied for particle diameters ranging from 30 to 100 nm, by calculating the extinction spectra shown in Figure 6. This set of calculations was performed for only the *p*-polarized contribution of the incident electric field to the extinction efficiency, a gap distance of 1.2 nm to mimic the effect of the AET spacer, and the dielectric function of gold for the underlying substrate and immobilized nanoparticles. The calculated spectra reveal that the SPR peak shifts to longer wavelengths as the particle diameter increases, which tracks with the experimental findings. Moreover, as summarized by the inset in Figure 6, the calculated extinction maxima closely match those that were experimentally measured. The calculated magnitude of extinction also undergoes a strong size dependence by increasing with particle size. However, a comparison of these results with measured values cannot be made due to experimental limitations already discussed. We add that the experimentally measured extinction peaks are broader than predicted with this model; this is likely due to a distribution of nanoparticle sizes and shapes.

We next investigated the theoretical prediction of the influence of the gap distance on the extinction spectra. An example set of calculated extinction spectra is shown in Figure 7. These calculations were performed using both the *p*-polarized and *s*-polarized contributions to the extinction efficiency to facilitate comparisons to the experimental data obtained using an unpolarized light beam. The spectra computations paralleled those used to construct the plots in Figure 6, except that values of 1.2 and 2.3 nm for the nanoparticle-substrate separation were used to account for and compare the contributions of the AET and AUT linkages. The calculated extinction band is red shifted for the 1.2-nm gap compared to the 2.3-nm gap by 48 nm. This difference agrees well with the 46-nm shift observed experimentally. Agreements within ~10 nm were also found for the other sizes of nanoparticles (Table 1).

The last set of calculations probed the difference in the SPR for nanoparticles immobilized on a gold versus a silver substrate and the resulting spectra are given in Figure 8. The calculations were again performed using both the *p*-polarized and *s*-polarized contributions to the extinction efficiency, a nanoparticle diameter of 60 nm, a nanoparticle-substrate gap of 1.2 nm or 1.3 nm to reflect differences in alkane chain tilt angles,[52] and the dielectric function of a gold or silver substrate. Based on differences in the dielectric functions of the substrate, the results predict a red shift for nanoparticle immobilization on a gold substrate compared to that on a silver substrate, which agrees with the experimental data (Table 1).[56]

3. Optimizing SERS Enhancement Factors of Immobilized Gold Nanoparticles.

One of the critical mechanistic underpinnings for SERS is the enhancement of the electric field at the surface of the nanoparticle. The SERS gain is maximized when the surface plasmon resonance couples to the electric fields generated at both the wavelength of the excitation source (λ_{ex}) and that of the scattered radiation (λ_{sc}). This coupling is optimized when the surface plasmon resonance wavelength is centered between λ_{ex} and λ_{sc}.[16, 19, 26, 57] DSNB, which is used to coat the gold nanoparticles, has the following Raman-active bands: a symmetric nitro stretch at 1336 cm^{-1}, a nitro scissoring vibration at 851 cm^{-1}, an aromatic ring mode at 1566 cm^{-1}, and an overlap of the N-C-O succinimidyl stretch with an aromatic ring mode at 1079 cm^{-1}.[7] Of these modes, the nitro stretch at 1336 cm^{-1} is the most intrinsically intense feature and is used for comparisons of SERS enhancement factors. The laser source excites the samples at 632.8 nm (λ_{ex}); thus, the position for the Stokes shifted nitro stretch is 690 nm (λ_{sc}). We therefore hypothesized that a surface plasmon resonance located at ~660 nm will maximize the enhancement factor. To test this theory, the following sections vary the parameters found to influence SPR in Section 2 and measure the SERS signal in an effort to make connections between SPR and SERS enhancement.

3.1 Effect of Nanoparticle Immobilization and Nanoparticle Size on the SERS Enhancement Factor. No observable Raman signal is obtained from DSNB-labeled nanoparticles with diameters of 30 to 100 nm for suspensions at the as-prepared concentrations (2.0 x 10^{11} to 5.6 x 10^{9} particles/mL). These concentrations correspond to the presence of an estimated 2500 to 84000 particles in the laser focal volume.[58] As shown below, this number of particles is similar to the number of immobilized particles irradiated in the ~4000 μm^2 focused laser beam, however, the immobilized particles give rise to a strong SERS signal. This result is consistent with expectations since the λ_{max} for the SPR of the suspended nanoparticles ranges from 529 to 565 nm, and very little coupling to λ_{ex} (633 nm) and λ_{sc} (690 nm) occurs.

Binding the nanoparticles to gold substrates greatly affects the SERS signal. Figure 9 shows the raw SERS spectra for DSNB-labeled nanoparticles, 30 to 100 nm in diameter, that are immobilized on an AET-coated gold substrate. Strong SERS responses that are consistent with the various vibrational modes of DSNB are observed in each instance. While it at first appears that the 80-nm nanoparticles give the largest enhancement, the surface concentrations of each of the substrates differ. To account for this variation, AFM images were collected for each sample and the nanoparticle surface concentrations (particles/μm^2) were measured.

Representative AFM images for samples prepared with 60- and 80-nm particles are shown in Figure 10. The images confirm that particles are present and randomly distributed on the surface, and that the sizes fall within the specified ±8% size range. While the particles appear larger than the vendor-specified sizes in the *x-y* plane, this is a manifestation of tip convolution effects,[59] and a detailed examination of the measured nanoparticle heights (data not shown) confirms the expected sizes. The SERS peak intensity for each of the prepared substrates was then divided by the nanoparticle coverage to determine a relative SERS signal per nanoparticle. These results are also reported in Table 1. As is evident, both 80- and 100-nm nanoparticles give the largest relative signal per particle.

The signal per nanoparticle, for each nanoparticle size, can clearly be affected by a difference in the number of scattering molecules due to the dependence of particle surface area on particle diameter. This difference must be factored out in order to more effectively compare the SERS enhancement as a function of each of the experimentally manipulated variables. Assuming the number of DSNB molecules per nanoparticle is proportional to nanoparticle surface area, the relative signal per particle can be divided by the nanoparticle surface area (nm^2/particle) to calculate the relative SERS enhancement factor (EF). This calculation gives the relative SERS EF per DSNB adsorbate.

The relative EFs calculated in this manner are reported in Table 1 for each set of nanoparticles. The EF reaches a maximum as the maximum of the SPR approaches the midpoint between the excitation source (633 nm) and the scattered band (690 nm). For the case of particles immobilized on a gold substrate via AET, as shown in Table 1, 60-nm nanoparticles result in the greatest EF. The UV-VIS absorption peak for this sample is located at 657 nm, close to the λ_{max} of the SPR value predicted to yield the greatest EF (i.e., 660 nm).

3.2 Effect of Gap Distance on SERS Enhancement Factor. To determine the influence of the gap distance on the EF, nanoparticles immobilized with AET and AUT on a gold substrate that have the same SPR λ_{max} must be compared. It follows, from Section 1.2, that 60-nm particles immobilized with AET and 80-nm particles immobilized with AUT, both on gold substrates, have similar values of λ_{max}, 657 nm and 652 nm, respectively. The relative signal per nanoparticle and the relative EF per DSNB molecule are given in Table 1 for each of these systems. The EF is much greater for the 60-nm nanoparticles bound with AET than for the 80-nm particles bound with AUT. The EFs are greater for every substrate tested that had similar extinction peaks but a smaller gap distance. This trend is easily visualized in Figure 11; at a given SPR, the EF is ~5 times greater for the 1.2-nm gap compared to the 2.3-nm gap. Thus, EFs are dependent upon the gap distance in addition to the SPR λ_{max}. We believe that this observation highlights the importance of the local field magnitude on surface enhancement. Earlier reports have found larger electric field magnitudes (i.e., "hot spots") between coupling bodies (i.e., particle-particle and particle-substrate), and that the magnitude of the field increases as the separation decreases.[60-62]

3.3 Effect of Substrate Material on SERS Enhancement Factor. Sections 3.1 and 3.2 show that the maximum EF is obtained for a sample with an SPR λ_{max} close to 660 nm when the substrate material and gap distance are held constant. Therefore, to determine the influence of the underlying substrate on EF, nanoparticles immobilized with an effectively constant gap distance and the same SPR λ_{max} must be contrasted. As shown in Section 1.3, 60-nm particles immobilized on gold and 80-nm particles immobilized on silver, both with AET, have similar values of λ_{max}, 657 nm and 663 nm, respectively. The relative signal per nanoparticle and the relative EF per DSNB molecule are given in Table 1 for each of these systems. The EFs are comparable for both substrates. Moreover, the EFs are found to be similar for every gold and silver substrate tested that had similar extinction peaks for a given gap distance. Thus, while the substrate material affects the surface plasmon, similar upper limits in EF can be attained as long as the nanoparticle sizes are selected to yield matching SPRs.

Conclusions

This paper demonstrates control over the SPR λ_{max}, and therefore, the SERS enhancement factor, for nanoparticles immobilized on a metal substrate. The absorption peak undergoes a red shift as the nanoparticle size increases and the gap distance decreases. Furthermore, a red shift was discovered for nanoparticles of the same size immobilized on a gold substrate compared to a silver substrate. This study also found that the SERS EF maximizes with the simultaneous minimization of gap distance and approach of the SPR λ_{max} to the midpoint between λ_{ex} and λ_{sc}. Thus, the SERS intensity can be optimized by varying the nanoparticle size, particle-substrate separation, and substrate material. These results lay the foundation necessary to design an optimized assay with the potential to measure SERS from a single nanoparticle in our SERS-based immunoassay without the need of a resonance Raman reporter molecule.

Acknowledgments

This work was supported through grants from DARPA-CEROS, NIH, and USDA-NADC and by the Institute for Combinatorial Discovery of Iowa State University. J. D. D. would like to gratefully acknowledge the support of the Mary K. Fassel and Velmer A. Fassel Fellowship. The Ames Laboratory is operated for the U.S. Department of Energy by Iowa State University under contract W-7405-eng-82.

References

(1) Rohr, T. E.; Cotton, T.; Fan, N.; Tarcha, P. J. *Anal. Biochem.* **1989**, *182*, 388-398.

(2) Dou, X.; Takama, T.; Yamaguchi, T.; Tamamoto, H.; Ozaki, Y. *Anal. Chem.* **1997**, *69*, 1492-1495.

(3) Ni, J.; Lipert, R. J.; Dawson, B.; Porter, M. D. *Anal. Chem.* **1999**, *71*, 4903-4908.

(4) Graham, D.; Mallinder, B. J.; Whitcombe, D.; Smith, W. E. *ChemPhysChem* **2001**, *12*, 746-748.

(5) Graham, D.; Mallinder, B. J.; Whitcombe, D.; Watson, N. D.; Smith, W. E. *Anal. Chem.* **2002**, *74*, 1069-1074.

(6) Cao, Y. C.; Jin, R.; Mirkin, C. A. *Science* **2002**, *297*, 1536-1540.

(7) Grubisha, D. S.; Lipert, R. J.; Park, H.-Y.; Driskell, J.; Porter, M. D. *Anal. Chem.* **2003**, *75*, 5936-5943.

(8) Mulvaney, S. P.; Musick, M. D.; Keating, C. D.; Natan, M. J. *Langmuir* **2003**, *19*, 4784-4790.

(9) Xu, S.; Ji, X.; Xu, W.; Li, X.; Wang, L.; Bai, Y.; Zhao, B.; Ozaki, Y. *Analyst* **2004**, *129*, 63-68.

(10) Faulds, K.; Smith, W. E.; Graham, D. *Anal. Chem.* **2004**, *76*, 412-417.

(11) Faulds, K.; Barbagallo, R. P.; Keer, J. T.; Smith, W. E.; Graham, D. *Analyst* **2004**, *129*, 567-568.

(12) Park, H.-Y.; Lipert, R. J.; Porter, M. D. *Proc. SPIE* 2004; 464-477.

(13) Driskell, J. D.; Kwarta, K. M.; Lipert, R. J.; Porter, M. D.; Neill, J. D.; Ridpath, J. F. *Anal. Chem.* **2005**, *77*, 6147-6154.

(14) Zhang, X.; Young, M. A.; Lyandres, O.; Duyne, R. P. V. *J. Am. Chem. Soc.* **2005**.

(15) Ansari, D. O.; Stuart, D. A.; Nie, S. *Proc. of SPIE* **2005**, *5699*, 82-90.

(16) Kneipp, K.; Kneipp, H.; Itzkan, I.; Dasari, R. R.; Feld, M. S. *J. Phys.: Condens. Matter* **2002**, *14*, R597-R624.

(17) Kerker, M.; Siiman, O.; Wang, D.-S. *J. Phys. Chem.* **1984**, *88*, 3168-3170.

(18) Kelly, K. L.; Coronado, E.; Zhao, L. L.; Schatz, G. C. *J. Phys. Chem. B* **2003**, *107*, 668-677.

(19) Weitz, D. A.; Garoff, S.; Gramila, T. J. *Opt. Lett.* **1982**, *7*, 168-170.

(20) Gupta, R.; Weimer, W. A. *Chem. Phys. Lett.* **2003**, *374*, 302-306.

(21) Kahl, M.; Voges, E. *Phys. Rev. B* **2000**, *61*, 14078-14088.

(22) Liao, P. F.; Stern, M. B. *Opt. Lett.* **1982**, *7*, 483-485.

(23) Haynes, C. L.; Duyne, R. P. V. *J. Phys. Chem. B* **2001**, *105*, 5599-5611.

(24) Haynes, C. L.; Duyne, R. P. V. *J. Phys. Chem. B* **2003**, *107*, 7426-7433.

(25) Felidj, N.; Aubard, J.; Levi, G.; Krenn, J. R.; Schider, G.; Leitner, A.; Aussenegg, F. R. *Phys. Rev. B* **2002**, *66*, 245407.

(26) Felidj, N.; Aubard, J.; Levi, G.; Krenn, J. R.; Hohenau, A.; Schider, G.; Leitner, A.; Aussenegg, F. R. *Appl. Phys. Lett.* **2003**, *82*, 3095-3097.

(27) Link, S.; El-Sayed, M. A. *J. Phys. Chem. B* **1999**, *103*, 8410-8426.

(28) Jensen, R. R.; Duval, M. L.; Kelly, K. L.; Lazarides, A. A.; Schatz, G. C.; Duyne, R. P. V. *J. Phys. Chem. B* **1999**, *103*, 9846-9853.

(29) McFarland, A. D.; Duyne, R. P. V. *Nano Lett.* **2003**, *3*, 1057-1062.

(30) Malinsky, M. D.; Kelly, K. L.; Schatz, G. C.; Duyne, R. P. V. *J. Am. Chem. Soc.* **2001**, *123*, 1471-1482.

(31) Jensen, T. R.; Schatz, G. C.; Duyne, R. P. V. *J. Phys. Chem. B* **1999**, *103*, 2394-2401.

(32) Wei, Q.-H.; Su, K.-H.; Durant, S.; Zhang, X. *Nano Lett.* **2004**, *4*, 1067-1071.

(33) Kim, K.; Yoon, J. K. *J. Phys. Chem. B* **2005**.

(34) Jiang, J.; Bosnick, K.; Maillard, M.; Brus, L. *J. Phys. Chem. B* **2003**, *107*, 9964-9972.

(35) Michaels, A. M.; Jiang, J.; Brus, L. *J. Phys. Chem. B* **2000**, *104*, 11965-11971.

(36) Xu, H.; Bjerneld, E. J.; Kall, M.; Borjesson, L. *Phys. Rev. Lett.* **1999**, *83*, 4357-4360.

(37) Keating, C. D.; Kovaleski, K. K.; Natan, M. J. *J. Phys. Chem. B* **1998**, *102*, 9414-9425.

(38) Reinhard, B. M.; Siu, M.; Agarwal, H.; Alivisatos, A. P.; Liphardt, J. *Nano Lett.* **2005**.

(39) Holland, W. R.; Hall, D. G. *Phys. Rev. B* **1983**, *21*, 7765-7768.

(40) Kume, T.; Nakagawa, N.; Hayashi, S.; Tamamoto, K. *Solid State Commun.* **1995**, *93*, 171-175.

(41) Shchegrov, A. V.; Novikov, I. V.; Maradudin, A. A. *Phys. Rev. Lett.* **1997**, *78*, 4269-4272.

(42) Zheng, J.; Zhou, Y.; Li, X.; Ji, Y.; Lu, T.; Gu, R. *Langmuir* **2003**, *19*, 632-636.

(43) Kim, K.; Lee, H. S. *J. Phys. Chem. B* **2005**.

(44) Orendorff, C. J.; Gole, A.; Sau, T. K.; Murphy, C. J. *Anal. Chem.* **2005**.

(45) Aravind, P. K.; Metiu, H. *Surf. Sci.* **1983**, *124*, 506-528.

(46) Wind, M. M.; Vlieger, P. A. B. J.; Bedeaux, D. *Physica* **1987**, *143 A*, 164-182.

(47) Okamoto, T.; Yamaguchi, I. *J. Phys. Chem. B* **2003**, *107*, 10321-10324.

(48) Wokaun, A.; Gordon, J. P.; Liao, P. F. *Phys. Rev. Lett.* **1982**, *48*, 957-960.

(49) Zeman, E. J.; Schatz, G. C. *J. Phys. Chem.* **1987**, *91*, 634-643.

(50) Creighton, J. A. In *Surface Enhanced Raman Scattering*; Chang, R. K., Furtak, T. E., Eds.; Plenum Press: New York, 1982, pp 315-337.

(51) It should be noted, however, that the dielectric function of the surrounding environment differs for that of the suspended particle (water) compared to that of the immobilized particle (air). If the ambient dielectric function was the same for both cases, immobilization would result in an even greater red shift than presented here.

(52) Widrig, C. A.; Chung, C.; Porter, M. D. *J. Electroanal. Chem.* **1991**, *310*, 35-359.

(53) It was determined that using more than 40 terms does not significantly alter the value for polarizability.

(54) Johnson, P. B.; Christy, R. W. *Phys. Rev. B* **1972**, *6*, 4370-4379.

(55) Kreibig, U.; Vollmer, M. *Optical Properties of Metal Clusters*; Springer-Verlag: Berlin, 1995.

(56) The extinction maxima on silver calculated with a gap of 1.2 nm are 617 and 663 nm, respectively, for 60- and 80-nm gold particles. This calculation exemplifies the extreme sensitivity of this system to nanoparticle-substrate separation.

(57) Oldenburg, S. J.; Jackson, J. B.; Westcott, S. L.; Halas, N. J. *Appl. Phys. Lett.* **1999**, *75*, 2897-2899.

(58) The laser focal volume was estimated as a cylinder with a diameter equal to that of the focused beam waist and a height equal to the focal depth.

(59) Montelius, L.; Tegenfeldt, J. O. *Appl. Phys. Lett.* **1993**, *62*, 2628-2630.

(60) Liver, N.; Nitzan, A.; Gersten, J. I. *Chem. Phys. Lett.* **1984**, *111*, 449-454.

(61) Zhang, P.; Haslett, T. L.; Douketis, C.; Moskovits, M. *Phys. Rev. B* **1998**, *57*, 15513-15518.

(62) Quinten, M. *Appl. Phys. B* **2001**, *73*, 245-255.

Figure Captions

Figure 1. The experimentally measured UV-VIS extinction spectra for different sizes of DSNB labeled gold nanoparticles suspended in 2 mM borate buffer (pH 8.5) containing 0.1% Triton X-100. Each spectrum is normalized with respect to its maximum extinction to account for differences in particle concentrations. The inset is a plot of the peak position as a function of particle diameter.

Figure 2. The experimentally measured *p*-polarized UV-VIS extinction spectra for different sizes of DSNB-labeled gold nanoparticles immobilized on an AET-modified gold substrate. Each spectrum is normalized with respect to its maximum extinction to account for substrate size and nanoparticle coverage variations. The inset is a plot of the peak position as a function of particle diameter.

Figure 3. The experimentally measured *s*-polarized UV-VIS extinction spectra for different sizes of DSNB-labeled gold nanoparticles immobilized on an AET-modified gold substrate.

Figure 4. The measured UV-VIS extinction spectra for 60-nm DSNB-labeled gold nanoparticles as a suspension and immobilized with AET and AUT on a gold substrate using unpolarized light. The dielectric function of the surrounding environment is that of water for the suspended particles and a mixture of an organic phase and air for the immobilized particles. Each spectrum is normalized with respect to its maximum extinction to account for substrate size and nanoparticle coverage variations.

Figure 5. The experimentally measured UV-VIS extinction spectra for 60-nm DSNB-labeled gold nanoparticles immobilized with AET on gold and silver substrates using unpolarized light. Each spectrum is normalized with respect to its maximum extinction to account for substrate size and nanoparticle coverage variations.

Figure 6. The calculated *p*-polarized UV-VIS extinction spectra for different sizes of DSNB-labeled gold nanoparticles, solved with a 1.2 nm gap distance between the nanoparticle and an underlying gold substrate. The inset compares the calculated to the experimental peak locations.

Figure 7. The calculated UV-VIS extinction spectra using unpolarized light for 60-nm DSNB-labeled gold nanoparticles immobilized with AET and AUT on a gold substrate.

Figure 8. The calculated UV-VIS extinction spectra using unpolarized light for 60-nm DSNB-labeled gold nanoparticles immobilized with AET on gold and silver substrates.

Figure 9. The SERS spectra for different sizes of DSNB-labeled gold nanoparticles immobilized on a gold substrate with AET. The spectra are offset for visualization.

Figure 10. AFM images (5 x 5 μm) of 60 nm (left) and 80 nm (right) gold nanoparticles immobilized on a gold substrate with AUT.

Figure 11. Plot of relative SERS enhancement factor as a function of surface plasmon resonance wavelength. The two sets of data (circles and squares) are for substrates created at two different gap distances. The vertical dashed lines represent λ_{ex} (left) and λ_{sc} (right).

Table 1. Comparisons of SPR λ_{max} and SERS EF for nanoparticles in close proximity to a metallic substrate, and the impact of changes in particle size, particle-substrate separation, and dielectric function of the substrate.

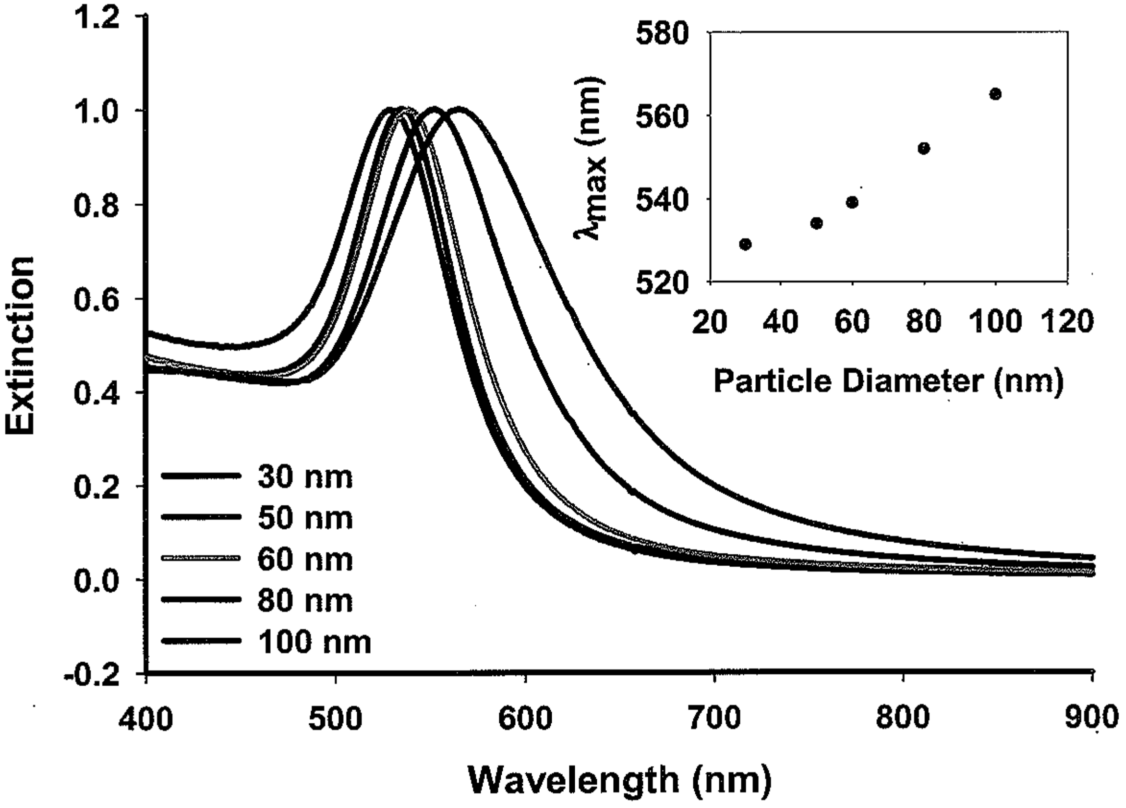
1.2
1.0
0.8
0.6
0.4
0.2
0.0
-0.2
Extinction
400
500
600
700
800
900
Wavelength (nm)
30 nm
50 nm
60 nm
80 nm
100 nm
580
560
540
520
λ_{max} (nm)
20
40
60
80
100
120
Particle Diameter (nm)

Figure 1

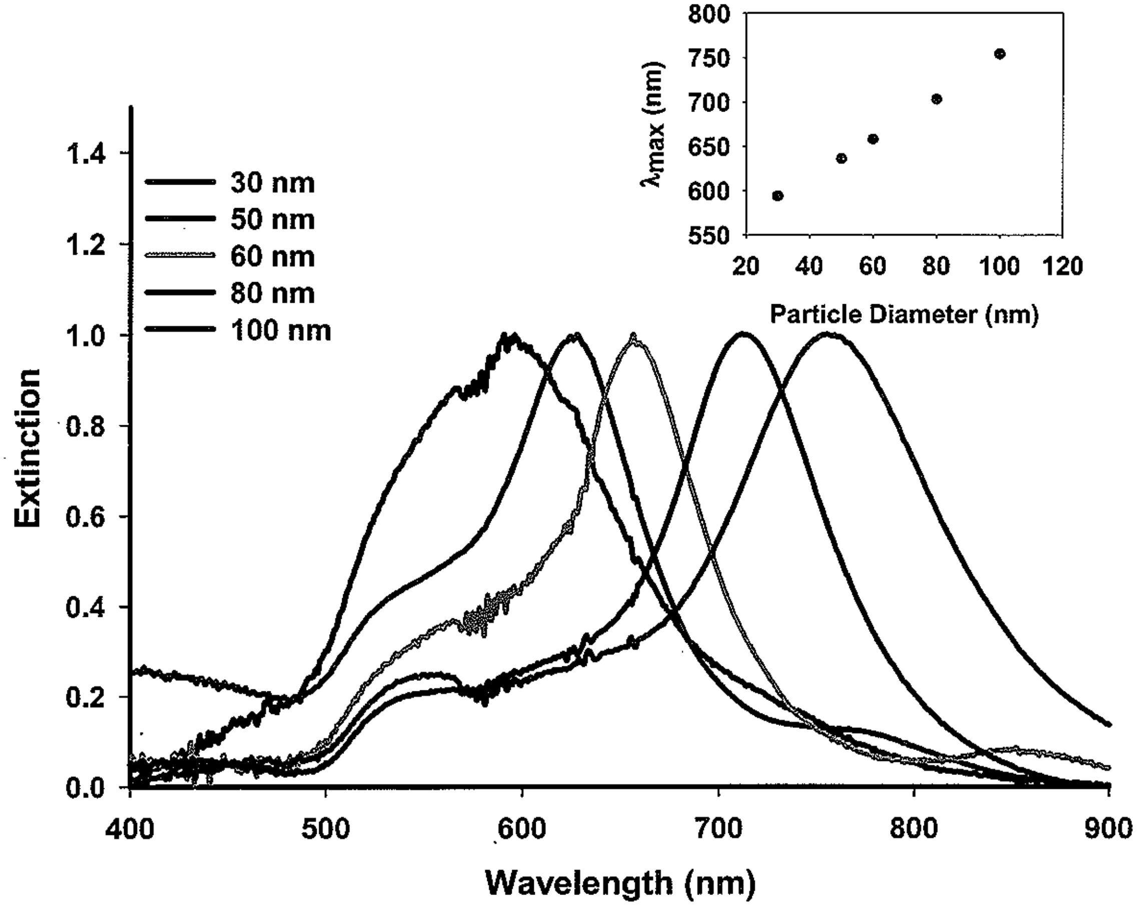
Extinction
1.4
1.2
1.0
0.8
0.6
0.4
0.2
0.0
400
500
600
700
800
900
Wavelength (nm)
30 nm
50 nm
60 nm
80 nm
100 nm
λmax (nm)
800
750
700
650
600
550
20
40
60
80
100
120
Particle Diameter (nm)

Figure 2

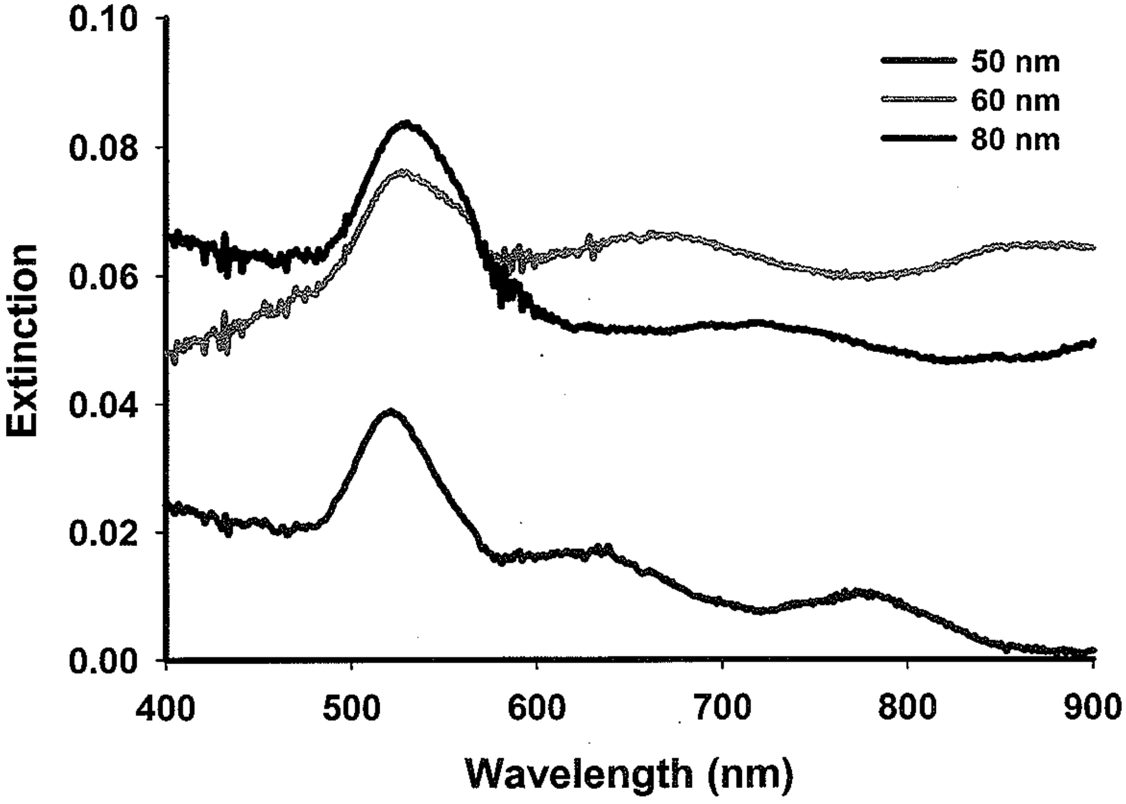
0.10
0.08
0.06
0.04
0.02
0.00
Extinction
400
500
600
700
800
900
Wavelength (nm)
50 nm
60 nm
80 nm

Figure 3

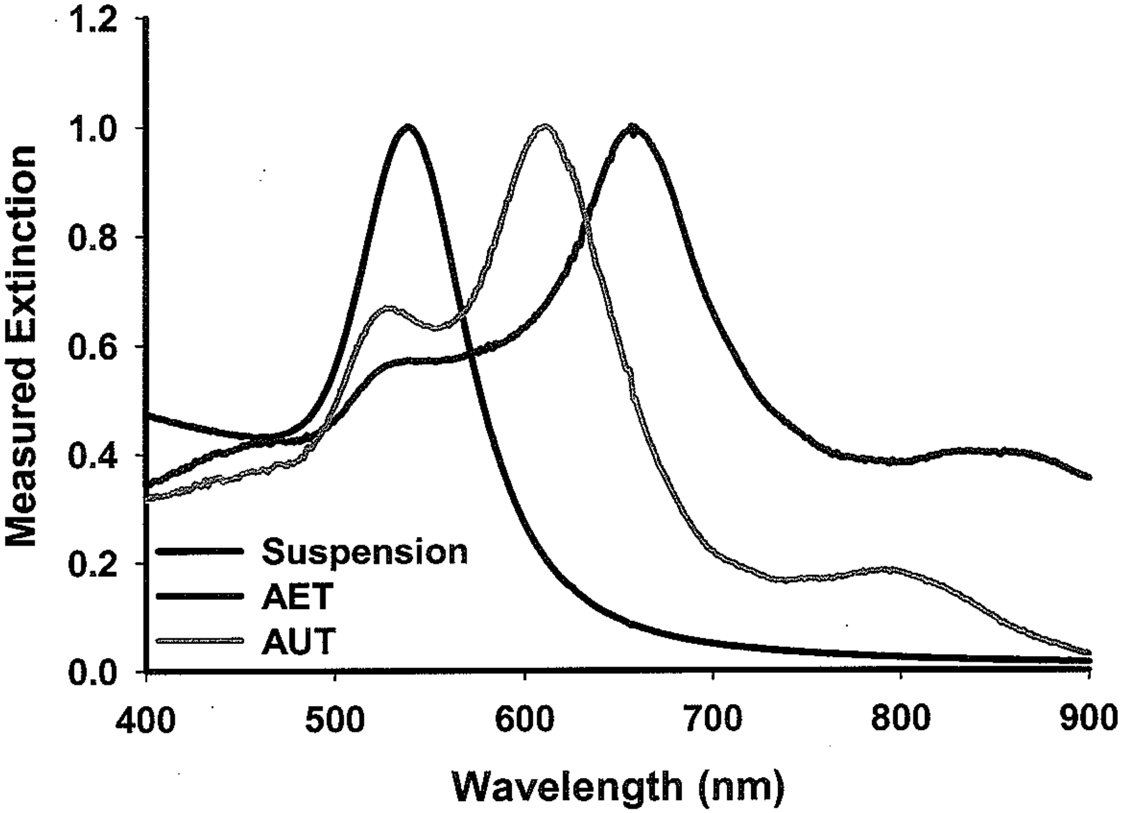
1.2
1.0
0.8
0.6
0.4
0.2
0.0
Measured Extinction
400
500
600
700
800
900
Wavelength (nm)
Suspension
AET
AUT

Figure 4

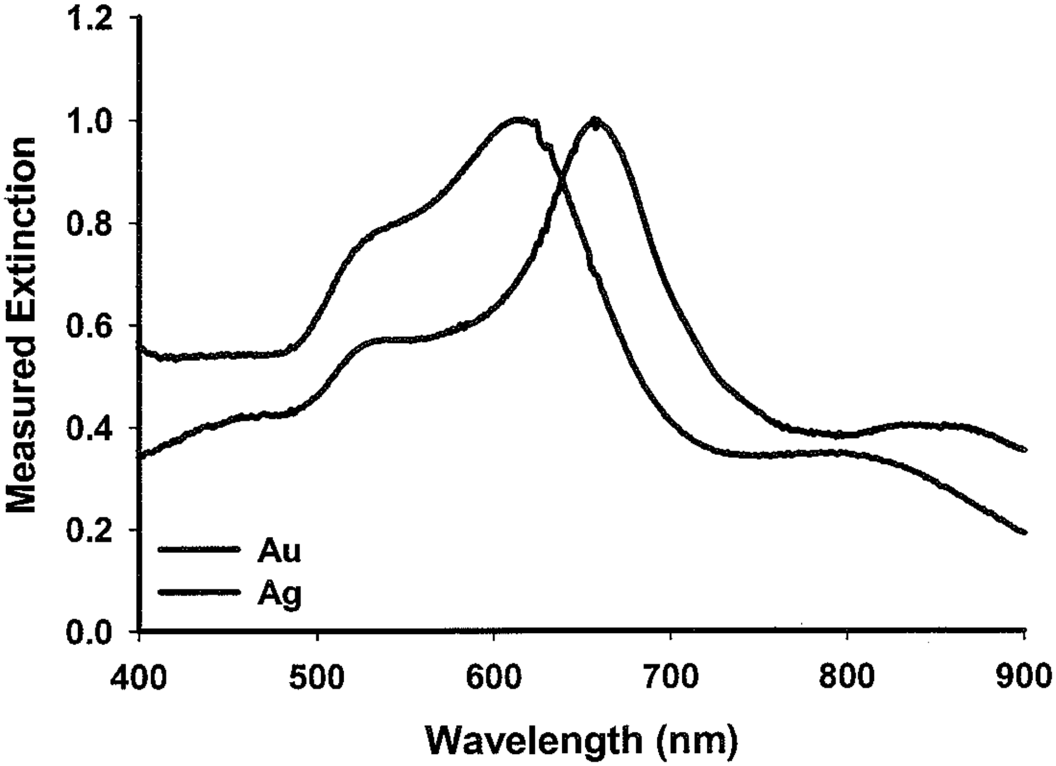
Measured Extinction
1.2
1.0
0.8
0.6
0.4
0.2
0.0
400
500
600
700
800
900
Wavelength (nm)
Au
Ag

Figure 5

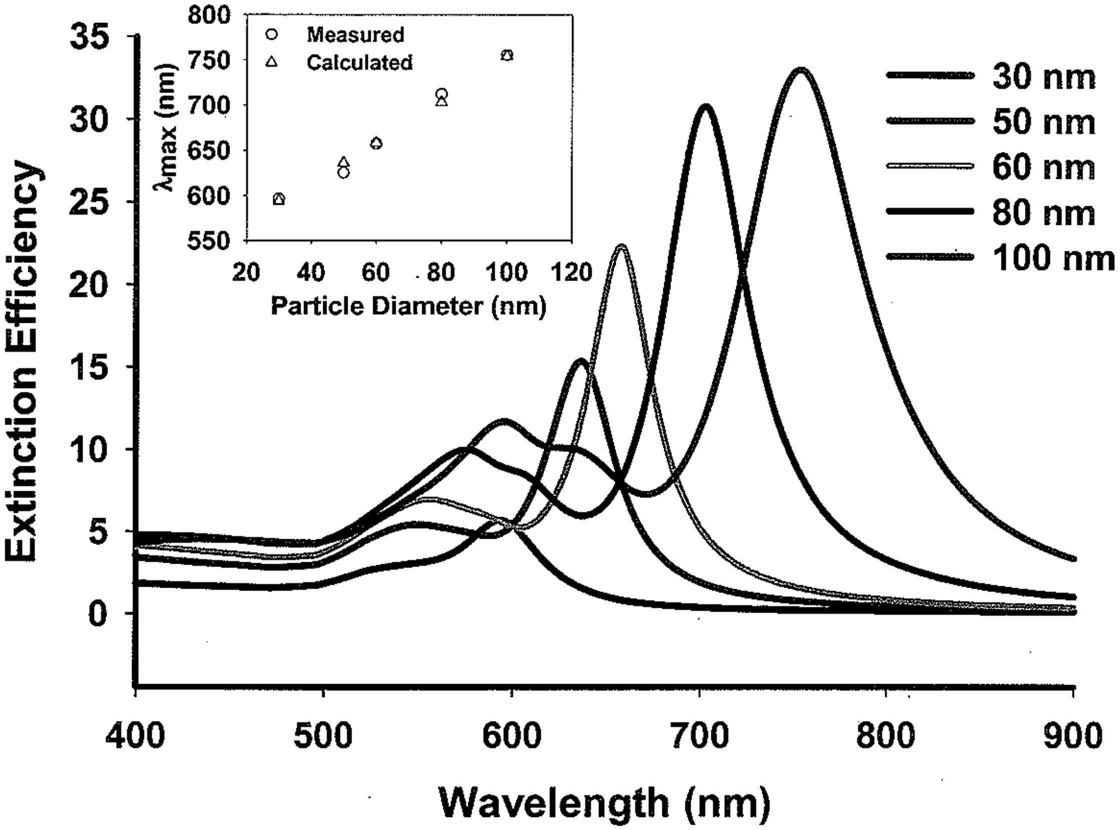
Extinction Efficiency
35
30
25
20
15
10
5
0
400
500
600
700
800
900
Wavelength (nm)
30 nm
50 nm
60 nm
80 nm
100 nm
λmax (nm)
800
750
700
650
600
550
20
40
60
80
100
120
Particle Diameter (nm)
○ Measured
△ Calculated

Figure 6

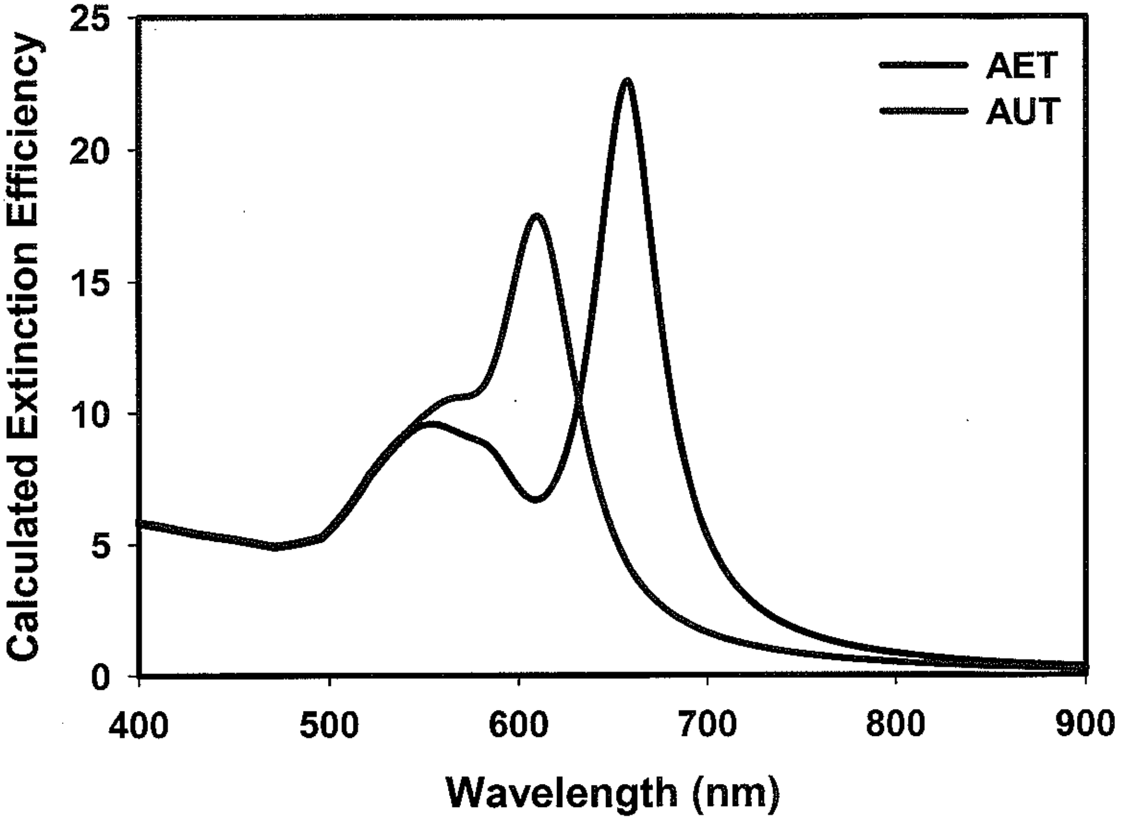

Calculated Extinction Efficiency
Wavelength (nm)
AET
AUT
0
5
10
15
20
25
400
500
600
700
800
900

Figure 7

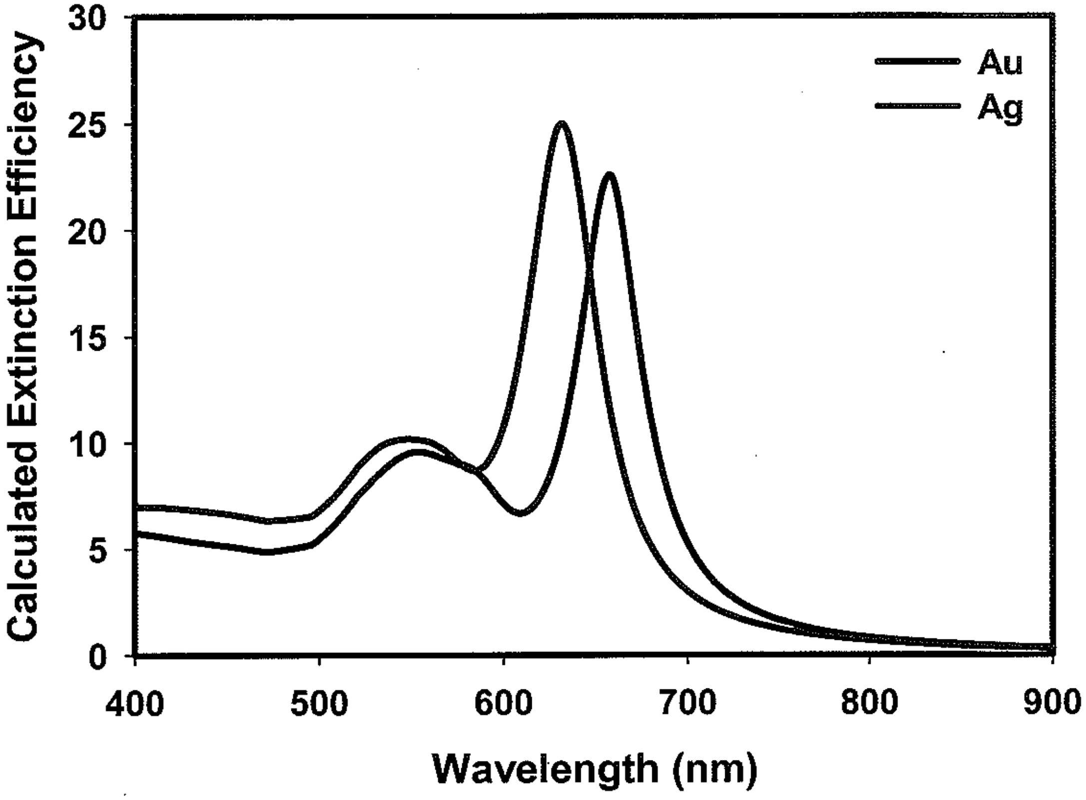
Calculated Extinction Efficiency
0
5
10
15
20
25
30
400
500
600
700
800
900
Wavelength (nm)
Au
Ag

Figure 8

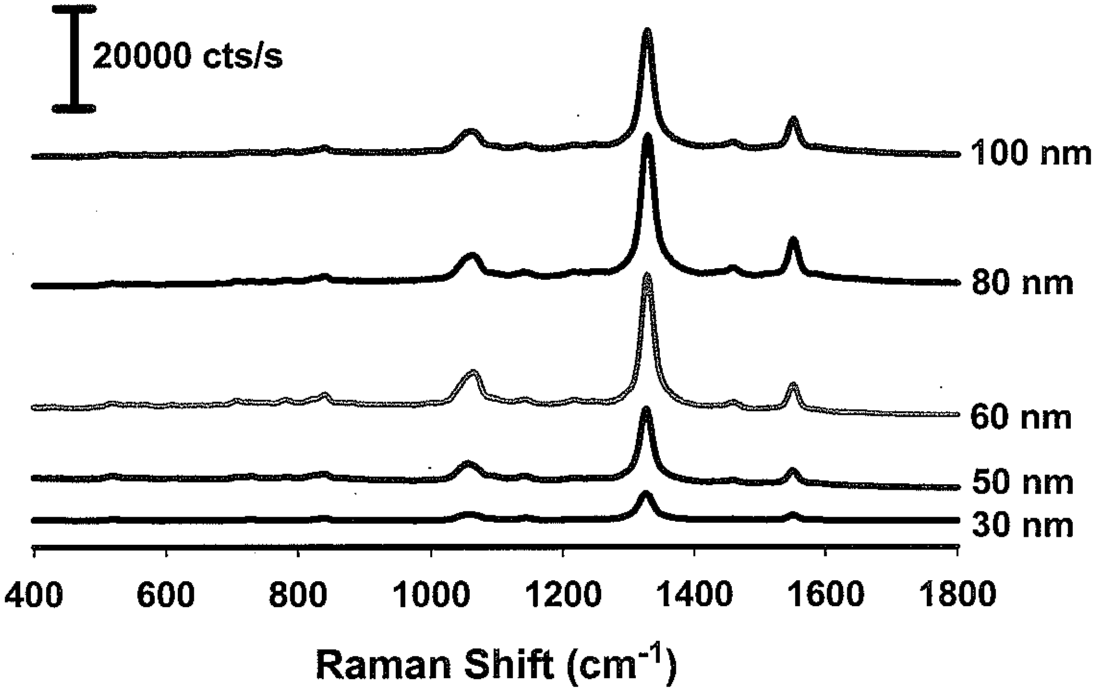
20000 cts/s
100 nm
80 nm
60 nm
50 nm
30 nm
400
600
800
1000
1200
1400
1600
1800
Raman Shift (cm^{-1})

Figure 9

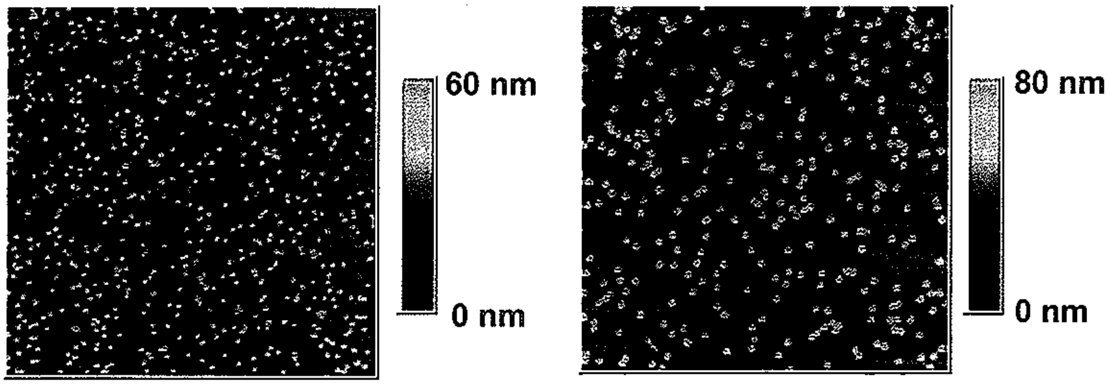

Figure 10

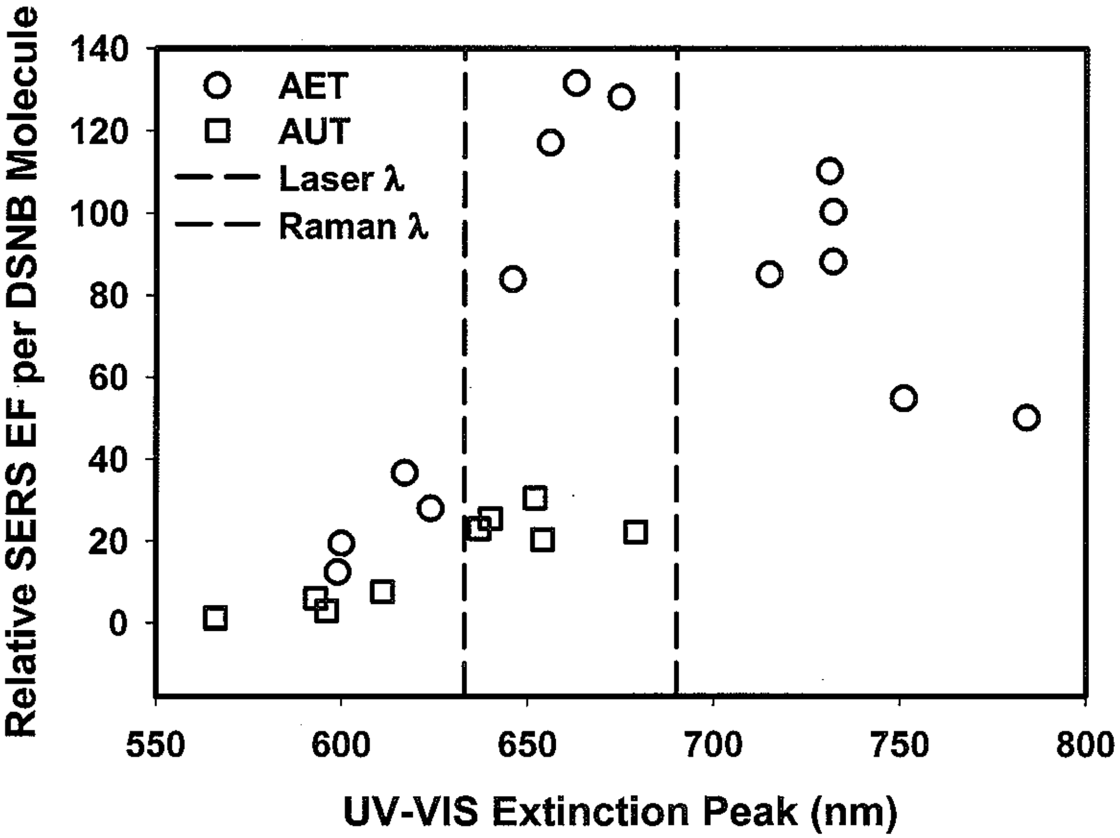
AET
AUT
Laser λ
Raman λ
Relative SERS EF per DSNB Molecule
140
120
100
80
60
40
20
0
550
600
650
700
750
800
UV-VIS Extinction Peak (nm)

Figure 11

Table 1

			SPR λ_{max} (nm)		Normalized SERS Signal	
Substrate	Gap (nm)	Particle Size (nm)	Measured	Calculated	Particle Density (cts*μm^2)/(s*particle)	DSNB Surface Concentration (cts*μm^2)/(s*nm^2)
Gold	1.2	30	596	594	121 ± 4	0.043 ± 0.001
Gold	1.2	50	625	636	759 ± 46	0.10 ± 0.01
Gold	1.2	60	657	658	4572 ± 77	0.41 ± 0.07
Gold	1.2	80	712	703	5904 ± 354	0.29 ± 0.02
Gold	1.2	100	755	754	5939 ± 297	0.19 ± 0.01
Gold	2.3	30	566	561	10.5 ± 1.1	0.0037 ±0.0004
Gold	2.3	50	596	594	79 ± 4	0.010 ± 0.001
Gold	2.3	60	611	610	294 ± 15	0.026 ± 0.001
Gold	2.3	80	652	650	2116 ± 254	0.11 ± 0.01
Gold	2.3	100	679	698	2415 ± 121	0.077 ± 0.004
Silver	1.3	60	617	623	1436 ± 59	0.13 ± 0.01
Silver	1.3	80	663	668	9135 ± 457	0.45 ± 0.02

CHAPTER 4: CONTROL OF ANTIGEN MASS TRANSFER VIA CAPTURE SUBSTRATE ROTATION: AN ABSOLUTE METHOD FOR THE DETERMINATION OF VIRAL PATHOGEN CONCENTRATION AND REDUCTION OF HETEROGENEOUS IMMUNOASSAY INCUBATION TIMES

A manuscript submitted to *The Journal of Virological Methods*

Jeremy D. Driskell, Karen M. Kwarta, Robert J. Lipert and Marc D. Porter*
Iowa State University, Institute for Combinatorial Discovery, Department of Chemistry,
Ames Laboratory-U.S. DOE, Ames, IA 50011-3020

Ann Vorwald, John D. Neill and Julia F. Ridpath
Virus and Prion Diseases of Livestock Unit, National Animal Disease Center, United States
Department of Agriculture, Ames, IA 50010

Abstract

Immunosorbent assays are commonly employed as diagnostic tests in human healthcare and veterinary medicine and are strongly relevant to the methodologies for bioterrorism detection. However, immunoassays often require long incubation times, limiting sample throughput. As an approach to overcome this weakness, this paper examines the use of rotating capture substrates to increase the flux of antigen to the surface, thereby reducing the incubation time. To assess the capability of this approach, porcine parvovirus (PPV) was selectively extracted from a sample solution exposed to a gold substrate modified with a covalently immobilized layer of anti-PPV monoclonal antibodies. The captured PPV were then directly imaged and quantified by atomic force microscopy. Substrate rotation rates were systematically varied to control the flux of PPV to the capture surface. Analysis of the experimental results, in combination with established theory for rotation-induced flux, allows an accurate determination of PPV concentration. Furthermore, the relationship between the quantal concentration units of 50% tissue culture infective dose (TCID$_{50}$) and quantitative concentration units of viruses/mL can be calculated. The benefits of substrate rotation are demonstrated by comparing dose-response curves, established by exposing the capture platform to the sample solutions for 10 min at 25°C, for an immunoassay performed under stagnant conditions to one performed with substrate rotation at 800 rpm. The limit of detection (LOD) improved to 3.4 x 10^4 TCID$_{50}$/mL (~80 fM) by rotating the capture substrate at 800 rpm from an LOD of 3.2 x 10^5 TCID$_{50}$/mL (~800 fM) under stagnant conditions. The potential to broadly apply this technique to heterogeneous immunoassays is also briefly discussed.

Introduction

Immunoassay development continues to be one of the most active areas at the interface between the analytical and biological sciences.[1, 2] This situation results in large part from the ever-increasing demand for diagnostic tests in human healthcare and veterinary medicine that enhance throughput, simplify sample workup, reduce analysis time, and lower the level of detection. Advances to these ends will not only improve chances for early diagnosis and thereby increase the likelihood of successful treatment and recovery, but also reduce the potential spread of disease and decrease the length of possible hospitalization.[3] This same set of advances is central to addressing challenges in bioterrorism prevention.[4]

Recent breakthroughs in electrochemical, optical, magnetic, scanning probe microscopic, and several other detection modalities are poised to meet these needs.[5-16] These developments have pushed the limit of detection to femtomolar levels and lower, performances that translate to a response of only hundreds to thousands of analytes when dealing with the microliter sample volumes accessible with emerging microfluidic constructs. The challenge with such systems, however, is that when the mass transfer of analyte is governed solely by diffusion, incubation times of several hours may be required when analyzing biological samples. This situation arises because diffusion coefficients for proteins and other large biolytes can be a few orders of magnitude lower than those for small molecules. In fact, recent theoretical treatments argue that the time required for low-level (i.e., picomolar or less) detection is unacceptably long for assays which rely only on the diffusional transport of large biolytes to recognition elements immobilized on surfaces in a biochip format.[17] This treatment suggests that the detection levels reported for some assays may reflect a limitation in mass transfer and not necessarily signal transduction. The challenge then is to develop strategies that rapidly transport the antigen to the capture substrate in order to take advantage of the emerging breakthroughs which enable quantification of exceedingly low amounts of material. Moreover, the potential to capitalize on enhancements in the flux of antigen is supported by research that has repeatedly shown that the rate of heterogeneous antibody-antigen binding is limited by antigen mass transport rather than by binding kinetics (i.e., recognition rate).[18-22]

Several laboratories have examined methods aimed at decreasing incubation times by increasing the flux of analyte to the capture substrate. For example, electric fields have been shown to drive the rapid transport of single-stranded DNA across a 200-μm solution layer, completing a hybridization-based assay in less than 7 s.[23] The same general concept has been used to direct the transport of antigens in completing a heterogeneous immunoassay in ~1 min.[24] Another example employed fluid confinement concepts to limit the flow profile of the antigen to a thin layer above a capture antibody substrate; this strategy, consistent with earlier predictions by computational models,[25] reduced the incubation time fourfold over static conditions.[26] Elevations in temperature,[27] which result in a decrease in solution viscosity, have also been found to reduce incubation times.

The work presented in this paper utilizes the rotation of capture antibody substrates as a means to increase the flux of antigen to the surface. Rotation is a well characterized method of controlling flux to a surface, and has historical precedence in electrochemistry where rotating disk electrodes (RDE) are used to manipulate mass transport in studies of electrode reaction mechanisms. RDEs have also been employed in immunoassays during the amperometric detection step of redox probes that were generated by an enzymatic label in a sandwich-type assay.[28-30] To our knowledge, only one example has taken advantage of rotation as a means to increase the flux of antigen to the capture substrate, and thereby decrease incubation times.[31] However, the goal of that study was solely to control mass transport in order to develop an assay in which the quantitative detection of antigen binding was independent of sample volume. The initial aim of the work herein was to reduce incubation times for the ultra-low level detection of viruses; a goal that, as we will show, was achieved.

This paper also reports on another interesting finding that developed over the course of this work—rotation-induced flow facilitates the accurate determination of virus concentration without the use of standards. Typically, virus concentrations are estimated with quantal rather than quantitative techniques.[32] These techniques, which include infectious and hemagglutination titrations and plaque assays, approximate virus concentrations in units of 50% tissue culture infective dosage ($TCID_{50}$), hemagglutination units (HA), or plaque-forming units (PFU), respectively. While quantal techniques have proven highly effective, concentrations given as the number of virus particles per unit volume represent a more effective means for assessment of assay performance and, ultimately, diagnostic utility. The ability to quantitate the number of viruses per unit volume is also necessary in order to accurately determine the total nucleic acid or capsid protein content in a particle for determinations of virus structure.[33]

At present, transmission electron microscopy (TEM) is the standard for the measurement of virus concentration in terms of virus particles per unit volume.[33] This method requires drying a known volume of virus on a TEM grid, enumerating the viruses in a well defined area on the grid, and extrapolating this value to represent the number of viruses on the droplet-coated surface. However, the reliable implementation of this approach requires highly purified virus solutions, the accurate transfer of small sample volumes to the TEM grid, and may be affected by clumping and other artifacts induced by drying. The analysis of the images also assumes that the observed coverage of the virus is uniform across the dried sample which is difficult to assess and control. The combined weight of these factors severely limits the reliability of this method.[33]

We show that rotating capture antibody substrates markedly lower the time required for sample incubation, result in a uniform antigen distribution on the surface, eliminate the need for virus purification, and can be used to determine virus concentration as viruses per unit volume. This quantitative technique can then be used to determine the relationship between the quantal units per unit volume (i.e., $TCID_{50}$, HA, and PFU) and viruses per unit volume.

Evaluation of our approach was performed with the capture of porcine parvovirus (PPV) (~25-nm diameter) on a rotating capture substrate. The capture substrate, which has been previously constructed in our laboratory,[9, 34] has an anti-PPV monoclonal antibody (mAb) covalently coupled to a gold surface through a gold-bound thiolate formed from dithiobis(succinimidyl propionate). The capture substrate is then inverted, attached to a rotating rod, and submerged in sample solution. After extraction of the PPV from sample solution, the viruses are enumerated utilizing an atomic force microscope (AFM). The capability of AFM as an analytical tool for imaging nanometer-sized objects, such as viruses, has recently been demonstrated.[12, 34, 35] Direct readout of antigen binding (i.e., label-free detection) eliminates any potential complications of modeling antigen binding that may occur due to labeling; however, many other readout methods (e.g., electrochemical, optical, magnetic, etc.) could be used. The experiments described herein were designed to examine the effect of substrate rotation rate and sample incubation time on the amount of virus bound to the capture platform as well as to quantitatively compare immunoassay performance with rotation to immunoassay performance under stagnant conditions. The findings of these experiments are discussed in light of theoretical expectations derived from established RDE theory.

Theory

The flux of material delivered to a rotating, planar substrate is well understood and can be quantitatively formulated for systems which meet the following criteria: 1) the bulk concentration of analyte in the sample solution is constant over the course of the experiment; and 2) the rate of the reaction at the substrate surface is mass transport limited (rather than kinetically limited). With these boundary conditions, theoretical treatments have been developed to quantitatively describe the mass transfer of analyte to an electrode surface for a wide range of electrochemical processes.[36] The same theory can be applied to a heterogeneous immunoassay provided that: 1) binding sites on the capture substrate are not saturated with antigen; 2) bulk antigen concentration in the sample solution does not vary during the time of incubation; and 3) antibody-antigen binding step is much faster than the delivery of antigen to the substrate. As we will show, the resulting theory allows the quantity of extracted antigen to be predicted, highlighting not only the importance of the antigen diffusion coefficient but also accentuating the need for increased mass transport for large molecules.

Using these boundary conditions, the diffusional-flux of antigen to the sensing surface (J_{diff}) and the accumulated surface concentration (Γ_a) over time can both be calculated by modified forms of the Cottrell equation,[37, 38] and are given by Equations 1 and 2, respectively

$$J_{Diff} = \frac{2}{\pi} D^{1/2} C_b t^{-1/2} \tag{1}$$

$$\Gamma_a = \frac{2}{\pi} D^{1/2} C_b t^{1/2} \tag{2}$$

where D is the diffusion coefficient of the antigen, C_b is the bulk antigen concentration, and t is time.

Equations 1 and 2 detail the temporal evolution of the antigen delivery rate and accumulation on a capture antibody substrate. Both Equations 1 and 2 also indicate that the delivery and accumulation of antigen at the surface of a capture substrate are directly proportional to $D^{1/2}$. This dependence indicates that a 100-fold difference in the diffusion coefficient of the antigen translates to a 10-fold difference in antigen accumulation. Moreover, Equation 2 shows that accumulation increases with $t^{1/2}$.

Figure 1 plots the accumulation of antigen ($C_b = 1.00 \times 10^8$ antigen/mL) at a surface as a function of time for two different diffusion coefficients, one typical of small molecules ($D = 1.00 \times 10^{-5}$ cm^2/s) and the other serving as an example of a large analyte ($D = 1.75 \times 10^{-7}$ cm^2/s). It is evident that Γ_a increases much faster for the small molecule compared to the large molecule. This plot illustrates the significance of incubation time prior to readout and emphasizes the need for increased mass transport in the case of a large analyte.

As noted earlier, a rotating disk configuration is an effective means in which to manipulate the rate of antigen binding because the hydrodynamic conditions that control the flux of material to a planar substrate are well understood and can be quantitatively formulated. Figure 2 depicts the key concepts of the system hydrodynamics, which involve convective mass transfer to establish steady-state conditions. As such, a rotating rod stirs the bulk solution at a carefully controlled and constant rate while delivering it to the surface of the disk at a quantifiable rate. Rotation also sets up a stagnant layer of solution at the disk surface, commonly referred to as the diffusion layer, in which an analyte must diffusively pass through to reach the disk. The convective-flux induced by rotation can be formulated by starting with Equation 3[37, 38]

$$J_{conv} = \frac{D}{\delta} C_b \tag{3}$$

where δ is the diffusion layer thickness at the surface created by rotation. Importantly, the diffusion layer thickness is controlled by rotation rate; larger rotation rates decrease the thickness, increasing the flux of the analyte. The thickness of the diffusion layer at the surface of a disk as a function of rotation velocity, as developed in a model by Levich,[39] is given by

$$\delta = 1.61 V^{1/6} D^{1/3} \omega^{-1/2} \tag{4}$$

where δ is in units of cm, D is in units of cm^2/s, V represents the kinematic viscosity of the sample solution (cm^2/s), and ω is the angular rotation rate of the substrate (radians/s). Equations 3 and 4 can be combined to provide an expanded description of antigen flux to the substrate for the steady-state case imposed by substrate rotation. This step yields

$$J_{conv} = \frac{D^{2/3} C_b}{1.61 V^{1/6}} \omega^{1/2} \tag{5}$$

Ultimately, the surface concentration of antigen on the capture substrate can be formulated by multiplying the total flux by the incubation time to give

$$\Gamma_a = \frac{2}{\pi} D^{1/2} C_b t^{1/2} + \frac{D^{2/3} C_b}{1.61 V^{1/6}} t \omega^{1/2} \tag{6}$$

The first term in Equation 6 accounts for the antigen accumulation in the absence of a steady-state delivery of solution (i.e., no rotation), but is quickly dominated by the second term once steady-state is obtained (i.e., rotation).

Equation 6 shows that for a given sample, the number of antigens bound to the capture substrate is dependent only upon incubation time and rotation rate. It is important to note that because of the boundary conditions imposed earlier, Γ_a in this expression is independent of sample volume. Additionally, Figure 1 demonstrates that the acquisition of both large and small antigens at the surface is markedly enhanced by substrate rotation (500 rpm) compared to antigen accumulation relying completely on diffusion. In both cases, the improvements are directly proportional to $\omega^{1/2}$.

For the purposes of our heterogeneous immunoassay, mass transport of the viral antigen to the capture surface is enhanced as the rotation rate increases and the diffusion layer decreases in thickness. Thus, it is theoretically possible to maintain or even increase Γ_a, while reducing the incubation time by increasing the rotation rate. This relationship suggests that the time required to carry out immunoassays previously performed under stagnant conditions, can be immensely reduced without sacrificing, and possibly lowering, the limit of detection. Furthermore, if D is known and the incubation time and rotation rate are controlled, it is possible to quantitate the antigen concentration, C_b, without the use of standards by measuring Γ_a, for systems described by Equation 6.

Experimental

Reagents. Octadecanethiol (ODT), dithiobis(succinimidyl propionate) (DSP), and phosphate buffered saline (PBS) packs (10 mM) were purchased from Sigma. Borate buffer packs (50 mM) were acquired from Pierce. Contrad 70 (Micro, Cole-Parmer) was used for cleaning glass substrates and two-part epoxy (Epoxy Technology) was employed to construct template stripped gold. All buffers were passed through a 0.22-μm syringe filter (Costar) before use. Poly(dimethyl siloxane) (PDMS) was obtained from Dow Corning.

Anti-PPV monoclonal antibodies (1 mg/mL), supplied by National Animal Disease Center (NADC; Ames, IA), were purified with a protein G column (Pro-Chem) and stored in 10 mM PBS. Aliquots of purified PPV, suspended in 10 mM PBS, were also provided by NADC. Detailed procedures for the generation of both the antibodies and the virus have been previously reported.[40] The PPV concentration of the stock solution was determined from titrations to be 3.2 x 10^9 $TCID_{50}$/mL using the Reed-Muench method.[41] All dilutions of the PPV stock solution were made with 10 mM PBS.

Capture Substrate Preparation/Immunoassay Protocol. Template stripped gold (TSG)[42] served as the base for fabrication of the capture substrate, noting that its low roughness factor (0.6 nm) facilitated the enumeration of PPV (hydrated diameter of ~25 nm) by AFM.[9, 12, 34] To prepare TSG, 250 nm of gold (99.9% purity) were resistively evaporated onto a 4-in p-type silicon [111] wafer (University Wafer) at a rate of 0.1 nm/s by using an Edwards 306A resistive evaporator. Next, 1 x 1 cm glass squares, cut from microscope slides (Fisher Scientific), were ultrasonically bathed in diluted Contrad 70, deionized water, and ethanol, each for 30 min. Epoxy cement was applied to one side of the clean glass chips, which were then affixed to the gold-coated silicon wafer and cured at 150° C for ~100 min. After curing, the glass chips were carefully detached from the wafer, a process that exposes a smooth gold surface.

TSG was exposed to an ODT-saturated PDMS stamp with a 4-mm hole cut in its center for ~30 s. The TSG was then rinsed with ethanol and dried under a stream of high purity nitrogen.[43-45] This procedure forms an ODT-derived monolayer on the outer portion of the TSG, which provides a circular hydrophobic barrier to localize reagents on the center of the substrate in subsequent steps and minimize both reagent and sample consumption. Next, the ODT-inked substrate was submerged in a 0.1 mM ethanolic DSP solution for ~12 h, rinsed with ethanol, and dried under a stream of high purity nitrogen. This process forms a DSP-based adlayer in the center of the substrate, which was not exposed to ODT in the stamping process.

Anti-PPV mAbs (20 μL), diluted to100 μg/mL in 50 mM borate buffer (pH 8.5), were pipetted onto the center of the substrate and allowed to react for 8 h in a humidity chamber at room temperature. During this step, a capture antibody layer is formed due to the amide linkage that arises from the covalent coupling of the primary amines on the mAbs to the terminal succinimidyl ester of the DSP-derived monolayer.[46-48] The substrate was immersed in 10 mM PBS (2.5 mL) three times to remove unreacted mAbs. After rinsing, the back of the capture substrate was quickly dried and attached to an RDE with double-sided tape while maintaining a thin layer of buffer on the topside of the substrate in order to ensure continual hydration of the mAbs. The RDE-mounted substrate was then loaded into a Pine analytical rotator (AFMSRX) and lowered to immerse the capture substrate in a 1.0-mL sample containing PPV. The rotation rate of the capture substrate and the incubation time with the PPV samples were varied. All sample volumes were held constant at 1.0 mL and all incubations were performed at room temperature. After incubation, the substrate was rinsed three times with 2.5 mL of PBS, exposed to a gentle flow of deionized water to remove residual salts (in order to facilitate AFM imaging), dried with a stream of high purity nitrogen, and imaged with AFM.

Instrumentation. (i) Rotator and Rotating Rod. The capture substrates were rotated with an AFMSRX analytical rotator from Pine Instrument Company. The rotator has an accuracy of 1% between 0 and 10,000 rpm. The slew rate of the motor is ~300,000 rpm/s; therefore, the desired rotation rate is effectively attained instantaneously for the rotation rates (50-1200 rpm) and incubation times (10-30 min) used in these experiments.

The capture substrate, as prepared above, is attached to an E2M single-piece RDE (Pine Instrument Company) by double sided tape (3M). This electrode readily mates with the AFMSRX rotator, having one end of the rod with a diameter of 6 mm that is clamped into the rotator and the other end of the rod (12-mm diameter) that not only fits into a sample well (17-mm diameter), but also closely matches the 1 x 1 cm capture substrate.

(ii) Atomic Force Microscopy (AFM). A MultiMode NanoScope IIIa SFM (Digital Instruments), equipped with a 150-μm scanner, was used to image viruses bound to the capture substrates. The AFM was operated in TappingMode under ambient conditions. An Ultrasharp cantilever/tip (MikroMasch) with a length of 120-130 μm, a width of 32-38 μm, a thickness of 3.5-4.5 μm, a resonant frequency of 265-400 kHz, and a spring constant of 20-75 N/m was used to image the substrates. The setpoint oscillation was set to 80% of the free oscillation amplitude and 25 μm^2 images were recorded at a scan rate of 1.5 Hz. The viruses in each topographic image were enumerated manually with a height scale of 20 nm using a pen style colony counter (Sigma).

Data Analysis. Experimental counts of bound PPV/25 μm^2 were plotted versus the substrate rotation rate. The error in the measurements were assumed to follow a Poisson distribution predicted by counting statistics[49] since the measured error was smaller than predicted, and is represented by the plotted error bars. Equations describing these curves were determined using the curve-fitting software provided with SigmaPlot 8.0, which relies on the Marquardt-Levenberg algorithm.[50] The fits were performed with the default parameters of 100 iterations (maximum), a step size of 100, and a tolerance of 0.0001. The curves were fit with weight $1/y^2$ to account for differences in the uncertainty of each data point.[49] The coefficient of determination (r^2 value) was used to measure the fit of the calculated equation to the experimental data.

Results and Discussion

The principal goal of this work was to reduce the required incubation time for immunoassays by substrate rotation while maintaining satisfactory performance (e.g., detection limit). A key step towards achieving this goal is understanding how best to implement rotation to control flux. The following sections therefore describe a detailed investigation of the relationship between capture substrate rotation rate and incubation time on PPV binding. First, experimental results are compared to theoretical predictions in order to substantiate the claim of controlled flux. Through curve fitting, it is possible to predict the PPV binding results for a given set of experimental conditions as well as extract the absolute solution concentration of virus in units of PPV/mL. Finally, the advantages of rotating a capture substrate are demonstrated by constructing a dose-response curve with and without substrate rotation.

Control of Antigen Extraction via Substrate Rotation and Incubation Time. Capture substrates were exposed to sample solutions of PPV (3.2×10^6 $TCID_{50}$/mL) with varying rotation rates and incubation times. The substrates were then imaged using AFM to visualize and enumerate captured PPV. A 5 x 5 μm scan size was selected to image the substrates because it balances the merits of imaging as large of an area as possible, while still providing sufficient resolution to confidently identify individual PPV particles when collecting 512 data points per line scan. A partial set of the AFM findings is presented in Figure 3. As evident, PPV appears as a spherical object with a height of ~18 nm (topography cross-sections not shown). The height (*z*-direction) of the imaged PPV is consistent for all the particles but is slightly smaller than expected. This difference is a result from the dehydration of the ~25-nm viral particles on the substrate after drying. Note as well that the lateral size of the PPV varies in the *x-y* plane from image to image. This lateral variation is an artifact of tip convolution effects[51] and the use of different tips to image different samples. Importantly, the consistency in height allows for identification and enumeration of captured PPV.

The AFM images in Figure 3 illustrate the effect of substrate rotation rate and sample incubation time on the number of viruses captured. The three images in Figure 3A present the findings for a 10-min incubation in PPV for a stationary capture substrate and for substrates rotated at 100 and 400 rpm. Rotation clearly yields a significant increase in the number of viruses bound to the substrate. Moreover, a larger rotation rate results in a rise in the number of bound viruses. A similar trend is evident in the images in Figure 3B for an incubation time of 30 min. Not surprisingly, when comparing images at the two different incubation times but same rotation rate, the longer incubation time leads to increased binding.

Figure 4 plots the observed surface concentration of bound viruses (normalized to an area of 25 μm^2) versus rotation rate for both 10- and 30-min incubation times. Rotation rates up to 1200 rpm were tested. These plots, as expected, demonstrate that both incubation time and rotation rate can be used to control the number of viruses binding to the capture substrate. Interestingly, the plots appear to approach different limiting values of Γ_a. If given sufficient time, both curves would reach the same value for Γ_a. However, the 30-min incubation plot would reach saturation at a slower rotation rate. A more detailed discussion of the shape of these profiles is given in the next section.

Relating $\mathbf{TCID_{50}}$ and Virus Concentration. A fit of the data plotted in Figure 4 to Equation 6, in addition to an implicit validation of the boundary conditions imposed for its derivation, will allow accurate predictions to be made regarding the impact on the assay with respect to changes in incubation time and rotation rate. The first boundary condition, the surface is not saturated with captured antigens, is validated by the AFM findings (Figure 3). Theoretically, a jamming limit treatment[52] indicates that ~3 x 10^4 PPV can fit in a 25-μm^2 area. However, as shown by Figure 4, no more than ~800 PPV were found in any 5 x 5 μm AFM image. The number of captured viruses is therefore only ~3% of that for a saturated substrate. The second boundary condition requires that the loss of PPV from solution during the incubation step does not alter the bulk virus concentration. To evaluate if this assumption holds, a 3.2 x 10^6 $TCID_{50}$/mL solution of PPV (1.0 mL) was exposed to a rotating capture substrate (1200 rpm) for 10 min. This substrate was then replaced by a second rotating capture substrate (1200 rpm) and exposed to the same PPV sample for 10 min. Both substrates were then imaged with AFM to determine if the number of captured PPV on the second substrate differed from that of the first. A difference would point to a change in the bulk concentration of PPV as a consequence of extraction by the first substrate, and potentially invalidate the second assumption. A representative AFM image of each substrate is given in Figure 5. The first substrate captured 346±8 PPV/25 μm^2 and the second substrate bound 341±16 PPV/25 μm^2. This result therefore supports the assumption that the bulk PPV concentration is not reduced during the time of incubation.[53] The third boundary condition, which pertains to the diffusion limited reaction rate for antigen-antibody binding, has been shown in multiple studies[18-22] and is most likely applicable in our system. As a result of validating the first two assumptions, demonstrating a close fit of the two profiles in Figure 4 to Equation 6 would strongly argue that the third assumption also holds.

The two sets of experimental data plotted in Figure 4 were fit to Equation 7 by using the Marquardt-Levenberg algorithm,[50] noting that the a-parameter represents the first term on the right side of Equation 6 and the b-parameter stands for all remaining variables in the second term of the same equation.

$$\Gamma_a = a + b\omega^{1/2} \tag{7}$$

The best fit curves for 10- and 30-min incubation with the sample solutions are given by Equations 8 and 9, respectively,

$$\Gamma_a = 25 + 9.9\omega^{1/2} \tag{8}$$

$$\Gamma_a = 49 + 26\omega^{1/2} \tag{9}$$

where Γ_a is in units of PPV/25 μm^2 and ω is in units of rpm. Importantly, the calculated curves reasonably follow the experimental data ($r^2 = 0.9952$ for 10 min, $r^2 = 0.9873$ for 30 min), confirming the dependence of the bound PPV on the square root of rotation rate. Additionally, the best fit determination of parameter b for the 30-min incubation data is approximately threefold greater than that for the 10-min incubation; this difference is consistent with the value of b being directly proportional to time. The a term, determined from the best fits, is proportional to $t^{1/2}$ but contains greater error since it is based only on two data points. This portion of the experiment is also complicated by the fact that immersion of the substrate disrupts the existence of a quiet solution. Taken together, the fit of the experimental data to Equation 6 strongly supports the validity of the third boundary condition which stipulates that the rate of the binding reaction must be mass transfer limited for the range of applied rotation rates. These results provide yet another example of a heterogeneous immunoassay that is controlled by mass transfer rather than the rate of antibody-antigen recognition.

The strong correlation between the experimental data and best fit curves provides an alternative means for a determination of the relationship between the infective titration parameter ($TCID_{50}$/mL) and absolute PPV concentration (PPV/mL) by evaluating the second term in Equation 6. All of the parameters in the second term, with the exception of C_b (PPV/mL), are known and the b value (Equation 7) is measured for both 10- and 30-min incubations. For the system presented, D_a is 1.75×10^{-7} cm^2/s (estimated using a hydrated radius of 12.5 nm via the Stokes-Einstein equation[54]), V is 1.004×10^{-2} cm^2/s at 25°C, and t is 10 or 30 min. Evaluation of Equation 6, in light of the known parameters and the experimentally determined value of b, yields a bulk concentration of PPV of 4.3×10^9 and 4.9×10^9 PPV/mL for the 30 and 10 min incubation time plots, respectively.

As a means to validate the PPV concentration determined from the rotation study, experiments using exhaustive binding of PPV from a known sample volume to capture substrates were performed. These studies exposed a small volume sample of PPV (20 μL) to a capture substrate. After ~12 h of incubation under stagnant conditions, the sample solution was carefully removed from the substrate and dispensed onto a second substrate for another 12-h incubation. This process was repeated five times using five fresh capture substrates. All substrates were then imaged and the number of viruses bound in a 25-μm^2 area for five different locations on each sample was enumerated. The average number of PPV bound in the imaged area was then extrapolated to delineate the number bound in the entire 4.0-mm diameter address on the capture substrate. The results from each substrate were added to determine the total number of PPV present in the 20 μL of sample solution.

This experiment was performed twice. The first attempt, as shown by the set of AFM images in Figure 6, yielded 187±15 PPV/25 μm^2 on the first substrate, 3±1 PPV/25 μm^2 on the second substrate, and no detectable PPV on all subsequent substrates. The second study captured 177±15 PPV/25 μm^2 on the first substrate, 6±2 PPV/25 μm^2 on the second substrate, and no detectable PPV on all subsequent substrates. The two exhaustive binding studies yielded PPV concentrations of $4.4 \pm 0.4 \times 10^9$ and $4.7 \pm 0.4 \times 10^9$ PPV/mL. These results are remarkably similar to the values of C_b calculated from the rotating substrate study, substantiating that the substrate rotation technique can be used as an absolute method for virus concentration determination.

The results from the substrate rotation study and exhaustive binding study indicate that the PPV concentration is between 4.3×10^9 and 4.9×10^9 PPV/mL. Since the specified concentration of PPV equaled 3.2×10^6 $TCID_{50}$/mL, 1 $TCID_{50}$/mL corresponds to 1300 to 1500 viruses/mL for PPV. $TCID_{50}$ is a measure of virus concentration based on the cytopathogenicity of a virus. However, different viruses have different inherent abilities infect and kill cells, and therefore the number of viruses that will cause cell death is specific for each virus.[33] Thus, the numerical quantities of two different viruses can not be directly correlated by using values of $TCID_{50}$/mL and a comparison of analytical figures of merit between methodologies is difficult unless the same virus is used. We believe that the above approach, which establishes the first conversion (to our knowledge) between the quantal numeric of infective dose units and viral concentration in units of viruses/mL for PPV, will serve as a much needed means to broadly perform such determinations.

Dose-Response Curves and Reductions in Incubation Time. Dose-response curves were constructed by exposing capture substrates to varying concentrations of PPV diluted in 10 mM PBS. Two sets of PPV binding experiments were carried out: one without substrate rotation and the other while the substrate was rotated at 800 rpm. All incubation times were held constant at 10 min, with the number of PPV bound to each substrate enumerated by AFM. Figure 7 plots the results of this study.

As is evident, the immunoassay performed with substrate rotation is much more sensitive than that relying solely on analyte diffusion. Only a few virus-sized objects are found in the 25-μm^2 images of blanks. The low responses from the blanks, which is expected in view of the use of purified antigen solutions and monoclonal antibodies, are attributed to debris with a size comparable to PPV and/or to a small amount of contamination from transfer pipettes. Based on these results, the limit of detection, which is defined as the concentration yielding a signal equal to the blank signal plus three times its standard deviation, is 3.2×10^5 $TCID_{50}$/mL without rotation and 3.4×10^4 $TCID_{50}$/mL with rotation at 800 rpm. If we use the average of the two conversion factors determined earlier, these results correspond to a limit of detection of 4.9×10^7 PPV/mL (~80 fM) with rotation and 4.6×10^8 PPV/mL (~800 fM) without rotation.

There is one other interesting, but not yet understood, observation from the plots in Figure 7. The response is linear for the immunoassay performed without rotation throughout the concentration range tested, while that with rotation is linear in the lower concentration range but begins to negatively deviate at high concentrations. Linearity is expected in both cases in accordance with Equation 6, and we are currently working to identify experiments that may provide insight into the observed deviation.

Finally, the overall approach to this assay has a strongly predictive value in that the experimental conditions can be tailored via Equation 6 to obtain the desired result. If, for example, all the known parameters for the PPV assay are incorporated into Equation 6, we can write,

$$\Gamma_a = C_b\left(1.6x10^{-9}t^{1/2} + 2.0x10^{-10}t\omega^{1/2}\right) \qquad (10)$$

where Γ_a is in PPV/25 μm^2, t is in minutes, C_b is in PPV/mL, and ω is in rpm. Equation 10 provides the flexibility to calculate: (1) the necessary rotation rate to detect a given C_b in a predetermined incubation time; (2) the limit of detection, C_b, at a fixed rotation rate and incubation time; or (3) the time required to detect a desired C_b with a set rotation rate. We believe that the predictive nature of this system is on par with the importance of its ability to convert from $TCID_{50}$/mL to PPV/mL and to rapidly detect exceedingly low levels of PPV.

Conclusions

Substrate rotation can be used to increase antigen flux to the capture surface in a heterogeneous immunoassay. The flux of the antigen can be controlled and employed to predict and design optimized immunoassays. Substrate rotation led to an improvement in the analytical performance of the presented AFM-based immunoassay as well as a decrease in incubation times. Additionally, due to the predictive nature of the system, it was possible to determine the concentration of PPV in an unknown sample solution without the use of standards and to develop an approach to convert quantal metrics to actual antigen concentrations. Experiments to apply this concept to more challenging sample types and matrices are planned.

Acknowledgments

The authors would like to thank A. J. Bergren for helpful discussions regarding the theory. This work was supported through a grant from USDA-NADC and by the Institute for Combinatorial Discovery of Iowa State University. J. D. D. would like to gratefully acknowledge the support of the Mary K. Fassel and Velmer A. Fassel Fellowship. K. M. K. would like to recognize the gracious support of a Dow Chemical Fellowship. The Ames Laboratory is operated for the U.S. Department of Energy by Iowa State University under contract W-7405-eng-82.

References

(1) Diamandis, E. P.; Christopoulos, T. K. In *Immunoassay*; Diamandis, E. P., Christopoulos, T. K., Eds.; Academic Press: San Diego, CA, 1996, pp 1-3.

(2) White, S. R.; Chiu, N. H. L.; Christopoulos, T. K. *Methods* **2000**, *22*, 24-32.

(3) Sokoll, L. J.; Chan, K. W. *Anal. Chem.* **1999**, *71*, 356R-362R.

(4) Chomel, B. B. *J. Vet. Med. Educ.* **2003**, *30*, 145-147.

(5) Ferguson, J. A.; Steemers, F. J.; Walt, D. R. *Anal. Chem.* **2000**, *72*, 5618-5624.

(6) Cao, Y. C.; Jin, R.; Mirkin, C. A. *Science* **2002**, *297*, 1536-1540.

(7) Grubisha, D. S.; Lipert, R. J.; Park, H.-Y.; Driskell, J.; Porter, M. D. *Anal. Chem.* **2003**, *75*, 5936-5943.

(8) Donaldson, K. A.; Kramer, M. F.; Lim, D. V. *Biosensors and Bioelectronics* **2004,** *20*, 322-327.

(9) Driskell, J. D.; Kwarta, K. M.; Lipert, R. J.; Porter, M. D.; Neill, J. D.; Ridpath, J. F. *Anal. Chem.* **2005**, *77*, 6147-6154.

(10) Wang, H.; Branton, D. *Nature Biotechnol.* **2001**, *19*, 622-623.

(11) Richardson, J.; Hawkins, P.; Luxton, R. *Biosensors & Bioelectronics* **2001,** *16*, 989-993.

(12) Nettikadan, S. R.; Johnson, J. C.; Mosher, C.; Henderson, E. *Biochem. Biophys. Res. Commun.* **2003,** *311*, 540-545.

(13) Kjeldsberg, E. *J. Virol. Meth.* **1986,** *14*, 321-333.

(14) Zheng, Y. Z.; Hyatt, A.; Wang, L.-F.; Eaton, B. T.; Greenfield, P. F.; Reid, S. *J. Virol. Meth.* **1999,** *80*, 1-9.

(15) Llic, B.; Yang, Y.; Craighead, H. G. *Appl. Phys. Lett.* **2004,** *85*, 2604-2606.

(16) Cousino, M. A.; Jarbawi, T. B.; Halsall, H. B.; Heineman, W. R. *Anal. Chem.* **1997,** *69*, 544A-549A.

(17) Sheehan, P. E.; Whitman, L. J. *Nano Lett.* **2005,** *5*, 803-807.

(18) Frackelton, A. R.; Weltman, J. K. *J. Immunol.* **1980,** *124*, 2048-2054.

(19) Stenberg, M.; Nygren, H. *J. Theor. Biol.* **1985,** *113*, 589-597.

(20) Stenberg, M.; Stiblert, L.; Nygren, H. *J. Theor. Biol.* **1986,** *120*, 129-140.

(21) Nygren, H.; Werthen, M.; Stenberg, M. *J. Immunol. Meth.* **1987**, *101*, 63-71.

(22) Myszka, D. G.; Morton, T. A.; Doyle, M. L.; Chaiken, I. M. *Biophys. Chem.* **1997,** *64*, 127-137.

(23) Heller, M. J.; Forster, A. H.; Tu, E. *Electrophoresis* **2000,** *21*, 157-164.

(24) Ewalt, K. L.; Haigis, R. W.; Rooney, R.; Ackley, D.; Krihak, M. *Anal. Biochem.* **2001**, *289*, 162-172.

(25) Glaser, R. W. *Anal. Biochem.* **1993**, *213*, 152-161.

(26) Hofmann, O.; Voirin, G.; Niedermann, P.; Manz, A. *Anal. Chem.* **2002**, *74*, 5243-5250.

(27) Johnstone, R. W.; Andrew, S. M.; Hogarth, M. P.; Pietersz, G. A.; McKenzie, I. F. C. *Mol. Immunol.* **1990**, *27*, 327-333.

(28) Wijayawardhana, C. A.; Purushothama, S.; Cousino, M. A.; Halsall, H. B.; Heineman, W. R. *J. Electroanal. Chem.* **1999**, *468*, 2-8.

(29) Salinas, E.; Torriero, A. A. J.; Sanz, M. I.; Battaglini, F.; Raba, J. *Talanta* **2005**, *66*, 92-102.

(30) Messina, G. A.; Torriero, A. A. J.; DeVito, I. E.; Olsina, R. A.; Raba, J. *Anal. Biochem.* **2005**, *337*, 195-202.

(31) Huet, D.; Gyss, C.; Bourdillon, C. *J. Immunol. Meth.* **1990**, *135*, 33-41.

(32) Murphy, F. A.; Gibbs, E. P. J.; Horzinek, M. C.; Studdert, M. J. *Veterinary Virology*, 3 ed.; Academic Press: San Diego, 1999.

(33) Wagner, E. K.; Hewlett, M. J. *Basic Virology*; Blackwell Sciences, Inc.: Malden, MA, 1999.

(34) Kwarta, K. M.; Driskell, J. D.; Neill, J.; Ridpath, J.; Porter, M. D. *Manuscript in preparation*.

(35) Kuznetsov, Y. G.; Malkin, A. J.; Lucas, R. W.; Plomp, M.; McPherson, A. *J. Gen. Virol.* **2001**, *82*, 2025-2034.

(36) Opekar, F.; Beran, P. *J. Electroanal. Chem.* **1976**, *69*, 1-105.

(37) Bard, A. J.; Faulkner, L. R. *Electrochemical Methods Fundamentals and Applications*, 2 ed.; John Wiley & Sons: New York, 2001.

(38) Rieger, P. H. *Electrochemistry*, 2 ed.; Chapman & Hall: New York, 1994.

(39) Levich, V. G. *Convective Diffusion in Liquids*, 2 ed.; Prentice-Hall: Englewood Cliffs, N.J., 1962.

(40) Mengeling, W. L.; Ridpath, J. F.; Vorwald, A. C. *J. Gen. Virol.* **1988**, *69*, 825-837.

(41) Reed, L. J.; Muench, H. *Am. J. Hyg.* **1938**, *27*, 493-497.

(42) Stamou, D.; Gourdon, D.; Liley, M.; Burnham, N. A.; Kuik, A.; Vogel, H.; Duschl, C. *Langmuir* **1997**, *13*, 2425-2428.

(43) Kumar, A.; Whitesides, G. M. *Appl. Phys. Lett.* **1993**, *63*, 2002-2004.

(44) Chen, C. S.; Mrksich, M.; Huang, S.; Whitesides, G. M.; Ingber, D. E. *Biotechnol. Prog.* **1998**, *14*, 356-363.

(45) Libioulle, L.; Bietsch, A.; Schmid, H.; Michel, B.; Delamarche, E. *Langmuir* **1999**, *15*, 300-304.

(46) Wagner, P.; Hegner, M.; Kernen, P.; Zaugg, F.; Semenza, G. *Biophys. J.* **1996**, *70*, 2052-2066.

(47) Jones, V. W.; Kenseth, J. R.; Porter, M. D.; Mosher, C. L.; Henderson, E. *Anal. Chem.* **1998**, *70*, 1233-1241.

(48) Duhachek, S. D.; Kenseth, J. R.; Casale, G. P.; Small, G. J.; Porter, M. D.; Jankowiak, R. *Anal. Chem.* **2000**, *72*, 3709-3716.

(49) Bevington, P. R. *Data Reduction and Error Analysis for the Physical Sciences*; McGraw-Hill: New York, 1969.

(50) SigmaPlot, 8.0 ed.; SPSS, Inc.: Chicago, IL, 2002.

(51) Montelius, L.; Tegenfeldt, J. O. *Appl. Phys. Lett.* **1993**, *62*, 2628-2630.

(52) Evans, J. W. *Rev. Mod. Phys.* **1993**, *65*, 1281-1329.

(53) Note: Later experiments captured as many as 800 PPV/25 μm^2. While those experiments extracted significantly more PPV than the ~340 PPV/25 μm^2 in these experiments, only ~8% of the PPV in the sample was extracted and therefore did not significantly alter the bulk concentration.

(54) Berry, R. S.; Rice, S. A.; Ross, J. *Physical Chemistry*; John Wiley & Sons: New York, 1980.

Figure Captions

Figure 1. Calculated antigen surface concentration accumulated as a function of time, antigen diffusion coefficient, and substrate rotation.

Figure 2. Schematic of solution flow in the presence of a rotating capture rod.

Figure 3. AFM micrographs (5 x 5 μm) of PPV bound to capture substrates with an incubation time of (A) 10 and (B) 30 min. The capture substrate was either held stationary, or rotated at 100 or 400 rpm.

Figure 4. The number of PPV bound to the capture substrates at varying rotation rates is plotted. Each plot is constructed from the average of 2-3 substrates at each rotation rate. Five AFM images from each capture substrate were then collected. The error bars represent the error introduced using Poisson statistics and the solid lines are weighted fits of the experimental data to Equation 7 (see text for details on data analysis).

Figure 5. AFM micrographs of successive exposure of two capture substrates (1200 rpm, 10 min incubation) to the same 3.2 x 10^6 HA/mL PPV sample solution. The first substrate (left) was exposed to the original sample and captured 346±8 PPV/25 μm^2. The second substrate (right) was exposed to the same PPV sample solution and bound 341±16 PPV/25 μm^2.

Figure 6. Exhaustive binding of 20 µL of PPV (3.2 x 10^6 HA/mL). The same sample was exposed to substrate A for ~12 h followed by subsequent exposure to substrate B and C for ~12 h each under stagnant conditions.

Figure 7. Dose-response curves for immunoassays performed under stagnant conditions and with capture substrate rotation at 800 rpm. The sample volume was 1.0 mL and the incubation time was 10 min. Each data point is the average signal measured from five different locations on the same sample substrate and the standard deviations are represented by the error bars.

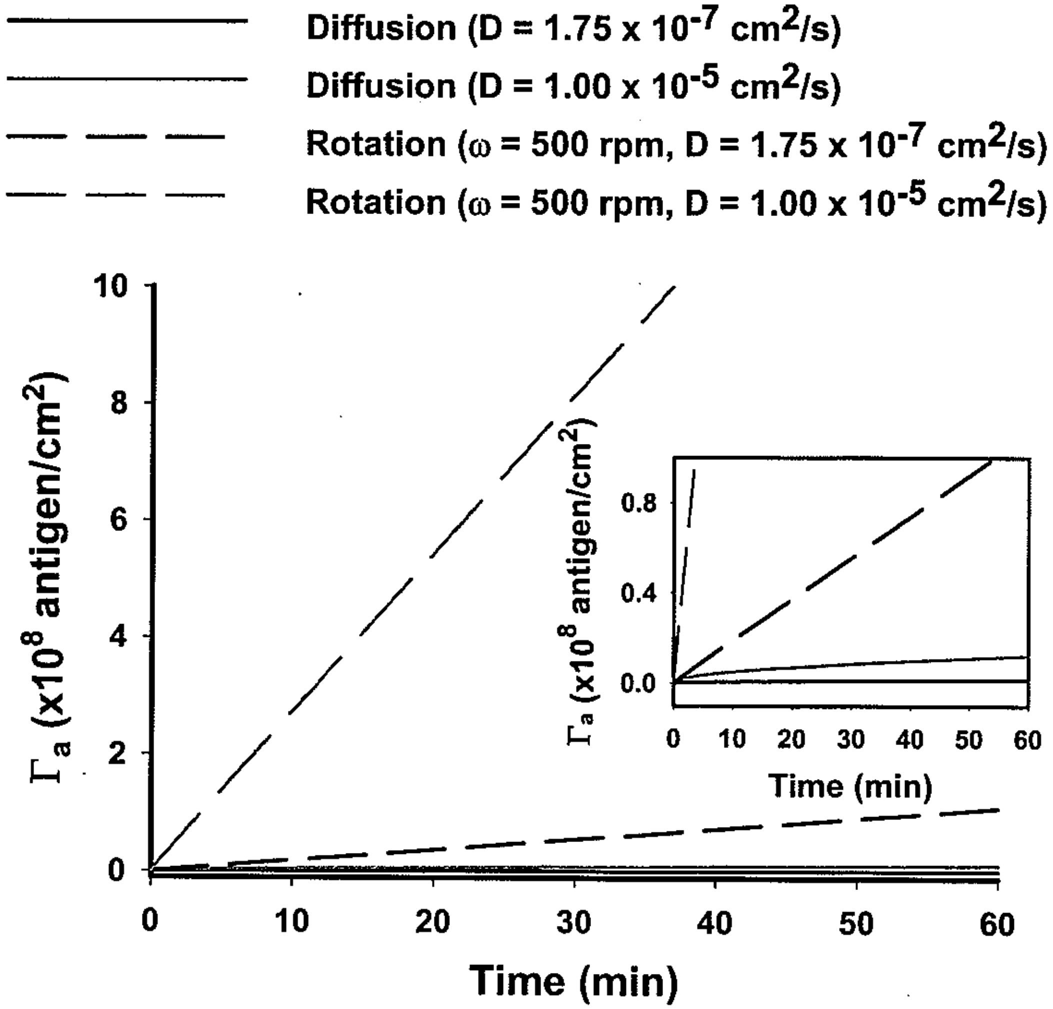
Diffusion (D = 1.75 x 10-7 cm2/s)
Diffusion (D = 1.00 x 10-5 cm2/s)
Rotation (ω = 500 rpm, D = 1.75 x 10-7 cm2/s)
Rotation (ω = 500 rpm, D = 1.00 x 10-5 cm2/s)
Γa (x108 antigen/cm2)
0
2
4
6
8
10
0
10
20
30
40
50
60
Time (min)
0.0
0.4
0.8
Γa (x108 antigen/cm2)
0
10
20
30
40
50
60
Time (min)

Figure 1

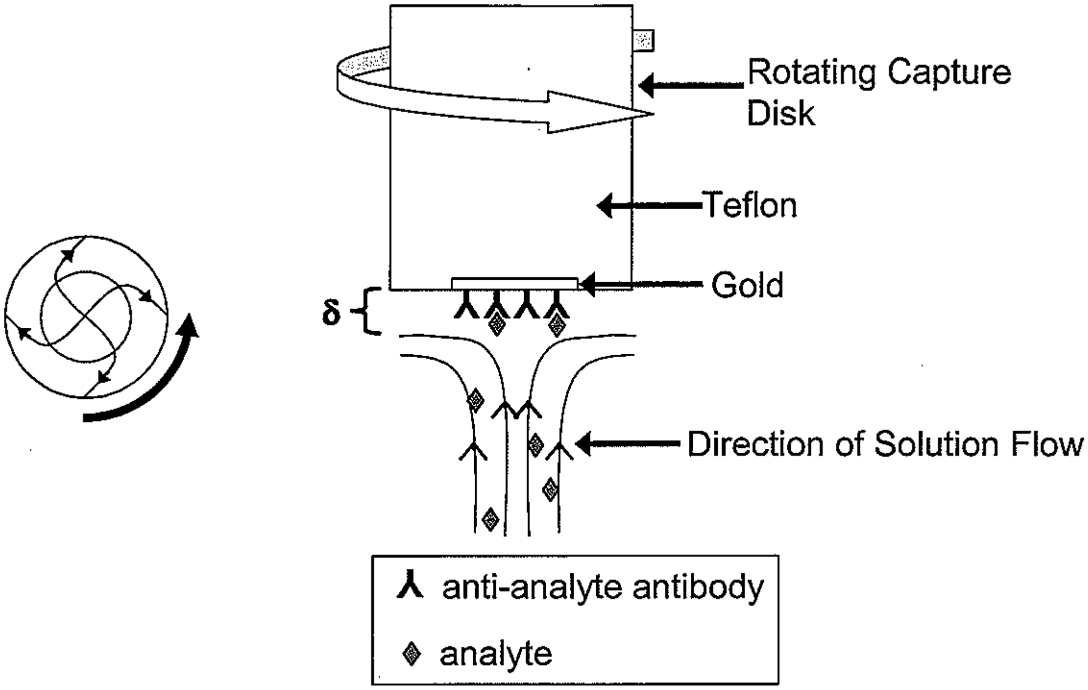
Rotating Capture Disk
Teflon
Gold
δ
Direction of Solution Flow
anti-analyte antibody
analyte

Figure 2

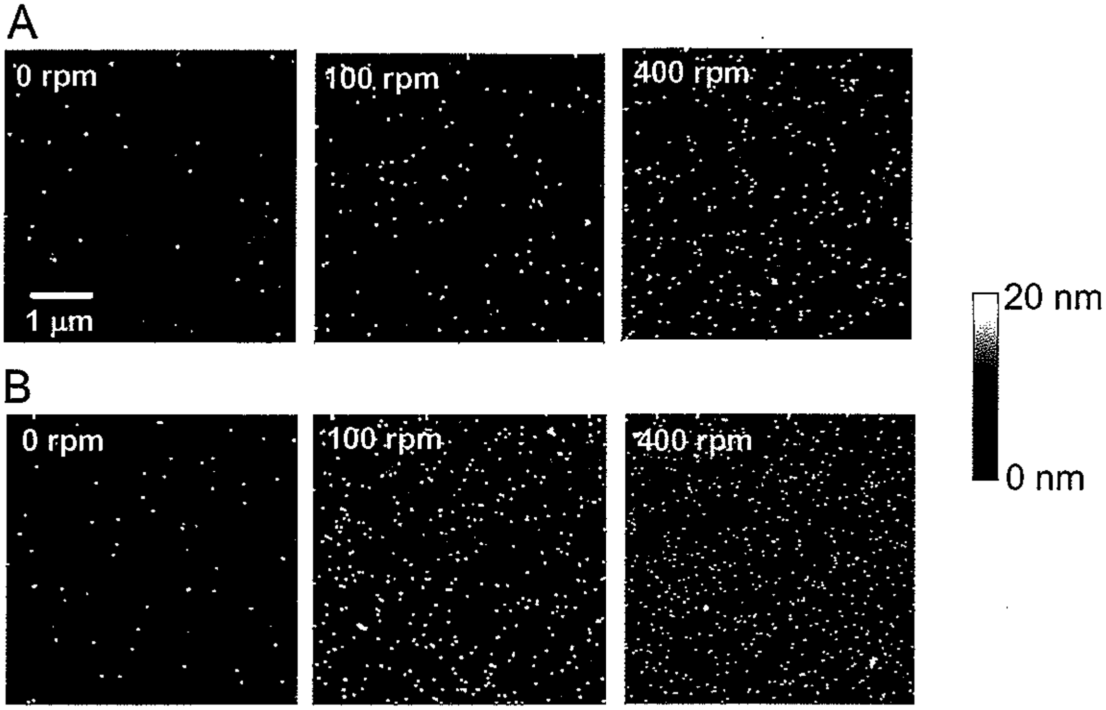

Figure 3

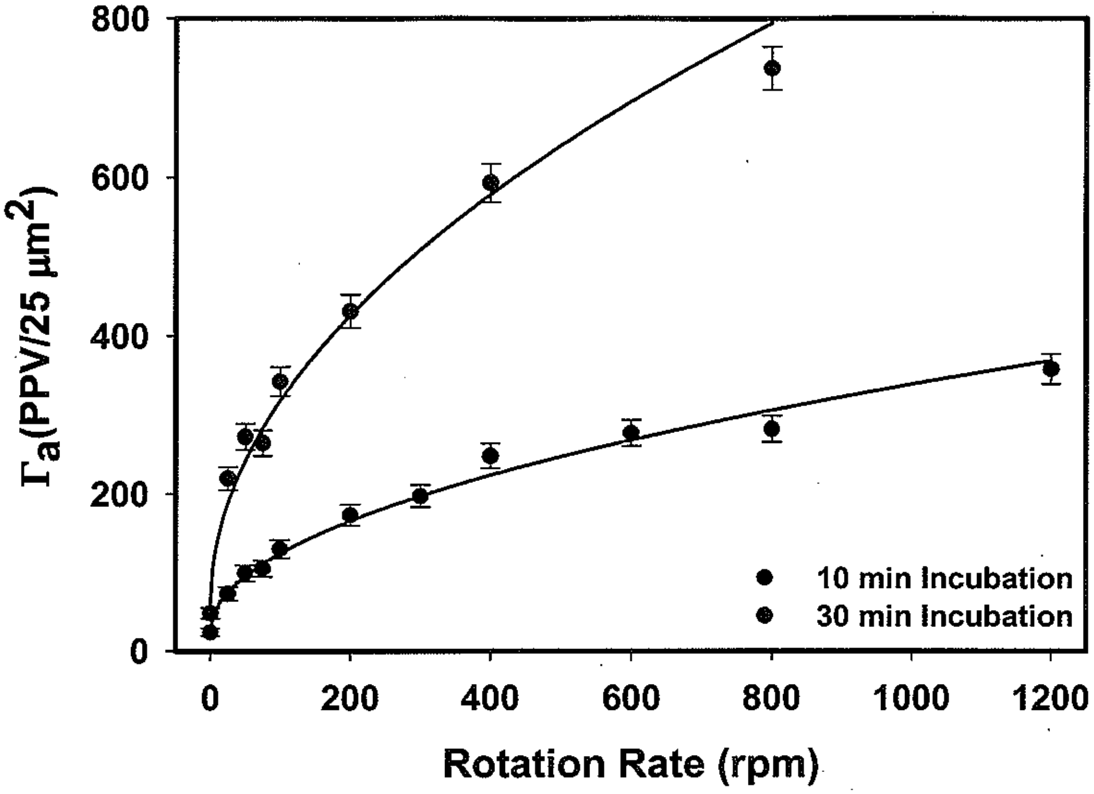

800
600
400
200
0
Γ_a(PPV/25 μm^2)
0
200
400
600
800
1000
1200
Rotation Rate (rpm)
● 10 min Incubation
● 30 min Incubation

Figure 4

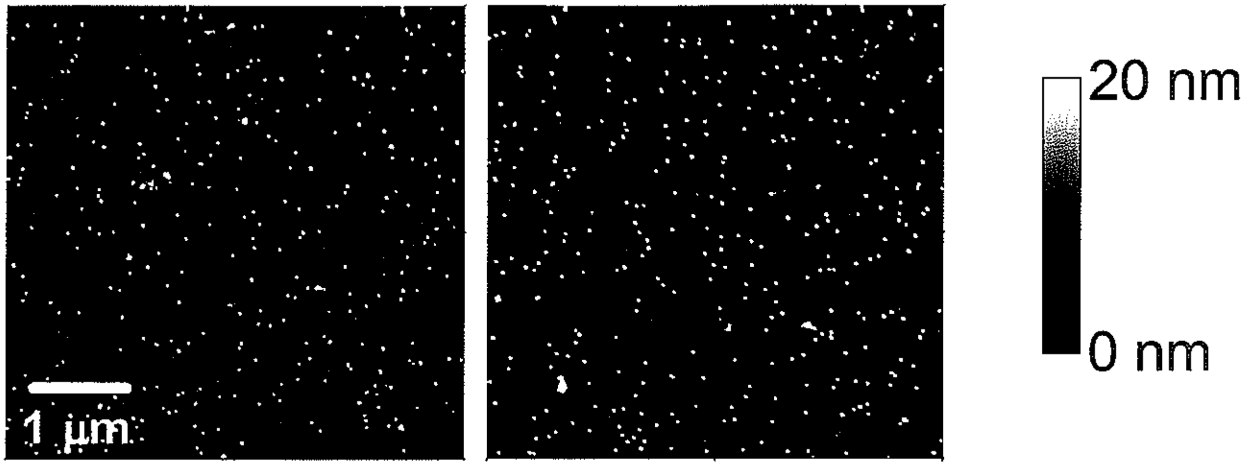

Figure 5

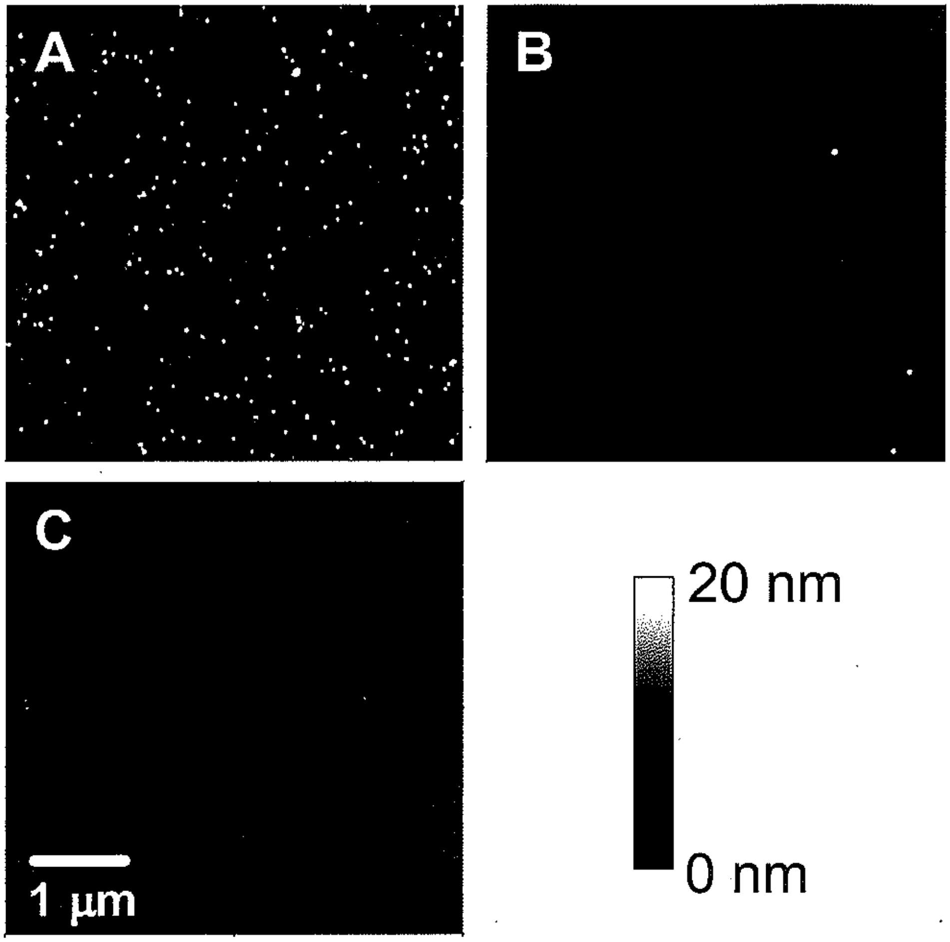

Figure 6

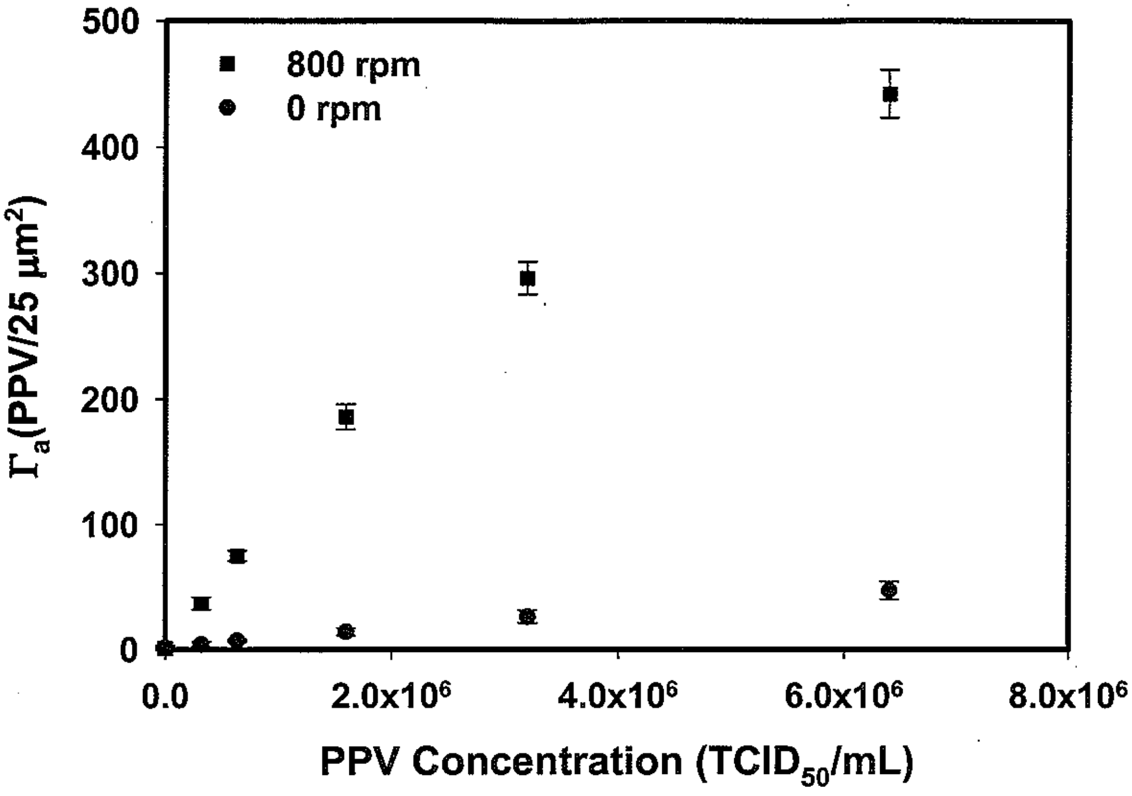

800 rpm
0 rpm
Γ_a(PPV/25 μm^2)
0
100
200
300
400
500
0.0
2.0x10^6
4.0x10^6
6.0x10^6
8.0x10^6
PPV Concentration (TCID$_{50}$/mL)

Figure 7

CHAPTER 5: SENSITIVE AND RAPID SURFACE-ENHANCED RAMAN SCATTERING IMMUNOASSAYS UTILIZING A ROTATED CAPTURE SUBSTRATE

A manuscript in preparation for submission to *Analytical Chemistry*

Jeremy D. Driskell, Jill M. Uhlenkamp, Robert J. Lipert and Marc D. Porter
Iowa State University, Institute for Combinatorial Discovery, Departments of Chemistry and of Chemical and Biological Engineering, and Ames Laboratory-U.S. DOE, Ames, IA 50011-3020

Abstract

A rapid, sensitive immunosorbent assay has been developed to meet the increasing demands in the medical and bioterrorism prevention arenas. The immunoassay couples the specificity of antibody-antigen interactions with the ultra-high sensitivity of surface-enhanced Raman scattering detection in a sandwich format. As a means to overcome the long incubation times often required for heterogeneous immunoassays, this paper introduces the concept of a rotating capture substrate to increase antigen and label flux to the solid phase surface, thereby reducing assay times. To investigate this strategy, polyclonal anti-rabbit IgG was immobilized on a gold capture substrate via a thiolate coupling agent. The capture substrate, capable of controlled rotation, was then immersed in a sample solution containing rabbit IgG, which served as a model analyte. After binding the target IgG, the substrates were immersed and rotated in an extrinsic Raman label (ERL) labeling solution, which is

composed of gold nanoparticles (60 nm) coated with an aromatic moiety as the Raman scatterer and an antibody as the biospecific recognition element. The effect of substrate rotation on both the antigen binding and ERL labeling steps was investigated. Implementation of optimized rotation conditions resulted in the reduction of assay times from 24 h to 25 min and a tenfold improvement in the limit of detection. The developed protocol was also applied to the detection of rabbit IgG suspended in goat serum, which served for assessment of performance in a biological matrix.

Introduction

Immunoassays have an important niche in the diagnostic laboratories of human and veterinary medicine and in efforts focused on bioterrorism prevention.[1-4] Even with the success and widespread use of these tests, improvements in sensitivity, specificity, speed, cost, and throughput are continuously sought to meet increasingly stringent demands. This paper seeks to provide improvements in the sensitivity and speed offered by many of the methodologies for heterogeneous assays.

Heterogeneous immunoassays require the delivery of antigen to a solid capture substrate, and typically rely solely on diffusion as the mode of mass transport. The challenge with such systems, however, is that long incubation times are required because large biological targets (e.g., proteins, viruses, and bacteria) have small diffusion coefficients.[5] This limitation is amplified for sandwich-type assays since a diffusion-based labeling step that utilizes a tagged antibody is needed in order to identify and quantify the surface-bound antigen.

Along these lines, a number of approaches have been investigated to increase the flux of the antigen or label as a means to reduce incubations times, capitalizing on the fact that antibody-antigen binding is often limited by mass transport rather than by binding kinetics (i.e., recognition rate).[6-10] Electric fields, for example, have been used to drive the transport of charged species, and have been employed to reduce the binding time for DNA hybridization assays[11] as well as for proteins in heterogeneous immunoassays to only a few minutes.[12] Paramagnetic labels have also been shown to bind to surface-bound antigen in a solid-phase immunoassay in less than 3 min using a magnetic field to aid in transport, whereas overnight incubations were required in the absence of a magnetic field.[13] In addition, the confinement of flowing sample solution to a thin layer above a capture antibody substrate has been found to decrease the binding time to 25% of that required for static incubation.[14] Another report has demonstrated that an equivalent level of antigen binding can be achieved in less time for assays conducted at elevated temperatures as compared to room temperature.[15]

Rotation, the focus of this paper, is an established method for controlling flux to a surface, and has long been exploited in investigations of electrochemical mechanisms by manipulation of the rate of mass transport.[16-18] We recently reported on an extension of this concept by introducing capture substrate rotation as a means to controllably increase antigen flux and therefore markedly reduce binding time.[19] That work utilized substrate rotation only in the antigen binding step. It also relied on atomic force microscopy for the direct enumeration of captured viruses, a readout technique that is more readily adaptable to imaging objects the size of viruses but not proteins.[20-24] In this earlier report, we showed that the accumulation of bound antigen, represented by its surface concentration Γ_a, during this first step is given by[19]

$$\Gamma_a = \frac{2}{\pi} D^{1/2} C_b t^{1/2} + \frac{D^{2/3} C_b}{1.61 V^{1/6}} t \omega^{1/2} \qquad (1)$$

where D is the antigen diffusion coefficient, C_b is the bulk concentration of the antigen, t is the incubation time, V is kinematic viscosity of the solution, and ω is the rotation rate. The first term on the right hand side of the equation represents the contribution of diffusional mass transfer, whereas the second term defines the role of substrate rotation. Equation 1 explicitly shows that antigen binding can be manipulated by varying t and ω.

There are a few precedents on the use of rotation in sandwich-type heterogeneous immunoassays.[25-28] Earlier work[25] used rotation as an effective means to control antigen flux to a capture substrate, targeting the development of an assay that was independent of sample volume rather than enhancements in mass transfer. Other laboratories took a different tactic by employing rotation during the amperometric detection step of an enzymatically generated redox probe.[26-28] The work herein describes a rotation-based method designed to reduce both the antigen and label binding times that can be universally applied to any sandwich-type immunoassay.

A plethora of readout methods have been created for heterogeneous immunoassays. More routine techniques for quantification include scintillation counting,[29] fluorescence,[30-32] chemiluminescence,[33] electrochemical,[34] and enzymatic methods.[2, 35] Other strategies, such as surface plasmon resonance,[36-41] surface-enhanced Raman scattering,[35, 42-56] quantum dots,[57-60] and microcantilevers,[61, 62] have shown great promise for increasing throughput and improving sensitivity, but are in earlier stages of development. Again, we believe that the approach detailed in this report can be readily adapted for use with all of these techniques.

As a proving ground for the merits of rotation in a sandwich immunoassay, this paper utilizes a SERS-based labeling scheme previously developed in our laboratory for readout.[44-46] Our approach employs extrinsic Raman labels (ERLs) to identify and quantify antigens in a sandwich immunoassay format. ERLs consist of gold nanoparticles coated with an intrinsically strong Raman scatterer as the spectroscopic tag and an antibody as the molecular recognition element. Previous studies resulted in the detection of as few as ~60 binding events using 30-nm-diameter gold nanoparticles, which for an assay of prostate specific antigen in human serum yielded a limit of detection of ~30 fM. [45] We more recently demonstrated the detection of single-digit binding events with the use of larger nanoparticles as a means to optimize surface plasmon coupling with the underlying gold substrate at the wavelength of the excitation source.[63]

While this intriguing readout strategy is proving to be extremely sensitive, there are several challenges to advancing its range and scope. One of the major obstacles rests with the long incubation times required by both the antigen-capture and -labeling steps, which becomes even more acute upon recognition that the large size and mass of the ERLs translate to even lower levels of diffusional mass transfer than the more typical labels (e.g., fluorescently or enzymatically tagged antibodies) in a sandwich-type assay. An estimate based only on particle size via the Stokes-Einstein equation[64] yields a diffusion coefficient for an ERL with a 60-nm gold core which is roughly tenfold smaller than that of a fluorescently labeled antibody. The labeling step with ERLs is therefore five times slower than that for a fluorescently tagged antibody.[65] By capitalizing on the second term in

Equation 1, it is possible to improve flux via substrate rotation in order to overcome diffusional limitations in both the antigen-capture and –labeling step imposed by small diffusion coefficients.

A general schematic of the assay is presented in Figure 1. One end of a rotating rod is coated with gold and modified with dithiobis(succinimidyl propionate) (DSP). Next, an antibody, which for the purposes of this work is anti-rabbit IgG, is covalently immobilized onto the surface via succinimidyl ester chemistry to the DSP-modified surface and the resulting capture surface is lowered into a sample solution. The rod is then rotated at a controlled rate, and if present, rabbit IgG is extracted onto the capture substrate. After a rinsing step, the capture substrate is subsequently immersed in a solution of ERLs and again rotated at a controlled rate. The analyte, rabbit IgG, is subsequently quantified by the spectral intensity of the Raman scatterer used to prepare the ERLs.

The goal of this work is to show that, like the antigen capture step, the ERL labeling step is also governed by Equation 1, and that rotation is applicable to assays carried out in a representative biological matrix (i.e., goat serum) as an effective means of reducing the binding time. The following sections detail studies on the effect of capture substrate rotation with respect to the antigen and ERL binding time and the limit of detection. We conclude with the implementation of rotation in an assay for rabbit IgG from goat serum in which the assay time is reduced from ~24 h to ~25 min and the limit of detection is improved by a factor of ten compared to the assay performed under static conditions.

Experimental

Reagents. Gold nanoparticles [60-nm diameter (<8% variation in diameter), 2.6 x 10^{10} particles/mL] were purchased from Ted Pella. Octadecanethiol (ODT), dithiobis(succinimidyl propionate) (DSP), and phosphate buffered saline (PBS) packs (10 mM, pH 7.2) were attained from Sigma. SuperBlock and BupH Borate Buffer Packs (50 mM, pH 8.5) were obtained from Pierce. The synthesis of DSNB was achieved following a previously published procedure.[45] All buffers were purified by passage through a 0.22-μm syringe filter (Costar). Contrad 70 (Decon Labs), a mild detergent, was used to clean the glass substrates. Poly(dimethyl siloxane) (PDMS) was acquired from Dow Corning and used to fabricate microcontact printing stamps.

Goat anti-rabbit IgG polyclonal antibody was purchased from US Biological. The antibody was purified by immunoaffinity chromatography and supplied as 0.5 mg/mL in PBS (pH 7.2) containing 0.01% sodium azide and 40% glycerol. Experiments show that the performance of the assay varies slightly with each batch of the antibody. Whole molecule rabbit IgG, also acquired from US Biological, was purified by Protein A affinity chromatography and stored at 10 mg/mL in PBS (pH 7.2). Unless otherwise noted, rabbit IgG was diluted with 10 mM PBS. Normal goat serum was obtained from Pierce and, where noted, served as a representative biological matrix for rabbit IgG dilution. This serum has a protein concentration of 60 mg/mL and a pH of 7.2.

ERL Preparation. ERLs are designed to provide a strong Raman signal and selective recognition by, in this case, immunospecificity. As such, DSNB was chosen as the Raman reporter molecule because of the intrinsically strong Raman scattering cross section of its symmetric nitro stretch, its ability to chemisorb to gold nanoparticles through its disulfide moiety, and its capacity to covalently conjugate antibodies via its succinimidyl ester. This design minimizes the distance between the Raman scatterer and the nanoparticle, yielding a large surface enhancement. This component of the label design is of particular importance because recent reports have proposed that enhancements undergo a sharp decrease (d^{-12})[66] as the distance (*d*) between the particle surface and scattering mode increases.

The ERLs are constructed by first adjusting the pH of a 1.0-mL suspension of 60-nm colloidal gold to 8.5 by adding 40.0 µL of 50 mM borate buffer. This pH was chosen to deprotonate the amines of the antibody added in subsequent steps, which promotes the reaction with the succinimidyl ester of DSNB and stabilizes the nanoparticle suspension upon conjugation with the antibody. Next, 10.0 µL of 1-mM DSNB, dissolved in acetonitrile, was added to the nanoparticle suspension and mixed for ~12 h to form a DSNB-derived coating on the gold surface. This step was followed by the addition of 20 µg of antibody (40.0 µL at 0.5 mg/mL) to the colloidal suspension. The antibody was reacted for ~8 h with the DSNB-modified nanoparticles. As detailed previously,[46] this concentration of antibody was necessary to fully coat the nanoparticles and maintain a stable suspension upon the addition of salt.

To block any unreacted succinimidyl ester groups, 100 µL of 10% BSA in 2 mM borate buffer was added to the nanoparticle solution for ~12 h. To remove excess DSNB, antibody, and other residual materials, the suspension was then centrifuged at 2000*g* for 10 min. After decanting the supernatant, the nanoparticles were resusupended in 1.0 mL of 2 mM borate buffer containing 1% BSA. This washing cycle was repeated twice to thoroughly clean the suspension. To achieve physiological conditions, concentrated NaCl was added to the ERLs to yield a final salt concentration of 150 mM. As a final step, the suspension was passed through a 0.22-μm syringe filter to remove any large aggregates.

Capture Substrate Preparation. Glass microscope slides (Fisher Scientific) were cut into 1 x 1 cm squares, and ultrasonically bathed in 10% Contrad 70, deionized water, and ethanol, each for 30 min. The glass was dried and 15 nm of chromium and 250 nm of gold were resistively evaporated onto the glass chips with an Edwards 306A evaporator, both at a rate of 0.1 nm/s at a chamber pressure less than 7.5×10^{-7} Torr. Upon removal from the evaporator, each substrate was addressed by exposure for ~30 s to an ODT-saturated PDMS stamp that had a 4.0-mm hole cut in its center. The substrates were then rinsed with ethanol and dried with a stream of high-purity nitrogen. This stamping procedure is a convenient method of forming a hydrophobic barrier on the outer portion of the substrate that defines a sample address as a means to localize aqueous reagents in the center of the substrate and minimize sample and label consumption. Next, the substrates were immersed in a 0.1 mM ethanolic solution of DSP for 8 h in order to form a DSP-derived monolayer on the gold portion of the substrate not inked with ODT. The substrates were then removed from the DSP solution, rinsed with ethanol, and dried with a stream of high-purity nitrogen.

Anti-rabbit IgG was immobilized on the substrates by pipetting 20.0 μL of 100 μg/mL solution of the antibody (diluted in 50 mM borate buffer) onto the DSP-modified region. After allowing 8 h for antibody coupling,[21, 67, 68] the substrates were rinsed three times with 2 mL of 10 mM PBS. The construction of the capture antibody substrates was completed by pipetting SuperBlock blocking buffer (20.0 μL) onto the capture substrate in order to block any unreacted succinimidyl ester. The capture substrates were then rinsed with 10 mM PBS after 12 h of exposure to the blocking buffer.[46]

Immunoassay Protocol. The capture substrates were exposed to sample solutions (PBS or goat serum) containing varied levels of rabbit IgG. The assays performed under stagnant conditions (i.e., no rotation) exposed 20.0 μL of sample to the capture substrate for 10 min or 12 h in a humidity chamber. Assays in which the capture substrate was rotated (800 rpm) required 1.5 mL of sample to effectively submerge the substrate and permit controlled stirring; these assays employed a 10-min incubation time.

After incubation, all samples were rinsed three times in 2 mL of 2 mM borate buffer (pH 8.5) containing 1% BSA and 150 mM NaCl. The capture substrates were then exposed to 20.0 μL of ERLs for 10 min or 12 h without rotation or 1.5 mL of ERLs for 10 or 15 min with rotation at either 800 or 1200 rpm. After incubation, the substrates were rinsed with 2 mM borate buffer (1% BSA, 150 mM NaCl, pH 8.5) and dried under a stream of high-purity nitrogen. The SERS spectra were then collected.

Instrumentation. (i) Rotator and Rotating Rod. The capture substrate, as prepared above, is attached to the end of a 17-cm stainless steel rod by double sided tape (3M). The diameter of the rod is 6 mm, which readily mates with an AFMSRX rotator (Pine Instrument Company). The substrate is then lowered into a sample or labeling well (17-mm diameter) and rotated at a controlled rate with the AFMSRX analytical rotator. The rotator has an accuracy of 1% between 0 and 10,000 rpm. The slew rate of the motor is ~300,000 rpm/s; therefore, the desired rotation rate is effectively attained instantaneously for the rotation rates (800 or 1200 rpm) and incubation times (10 or 15 min) used in these experiments.

(ii) SERS Measurements. Raman spectra were collected with a NanoRaman I (Concurrent Analytical) fiber-optic Raman system. The excitation source is a 30-mW, 632.8-nm He-Ne laser. The spectrograph consists of an f/2.0 Czerny-Turner imaging spectrometer (resolution of 6-8 cm^{-1}) and a thermoelectrically cooled (0°C) CCD (Kodak 0401E). The probe objective (numerical aperture 0.68) focuses the laser to a 25-µm diameter spot on the substrate surface. The same objective is used to collect the scattered Raman radiation. All spectra were acquired with a 1-s integration time.

Results and Discussion

Control Studies. Initial experiments to detect rabbit IgG using the SERS-based assays were performed by following our earlier protocol, which serve as a comparative standard[46] and a control in each experiment to account for differences in performance due to variations with different batches of vendor supplied antibodies. This comparative protocol called for a 12-h incubation of the capture substrate with a 20.0 µL sample of rabbit IgG, followed by a 12-h incubation in 20.0 µL of the ERL labeling solution. Both steps were performed in stagnant solution. The Raman spectra for varied concentrations of rabbit IgG, including a blank solution, are presented in Figure 2. All these spectra contain features characteristic of the DSNB-based Raman reporter molecule, and are diagnostic of the presence of the DSNB-modified ERLs.[45] The dominant feature in the spectra is the symmetric nitro stretch ($\nu_s(NO_2)$) at 1336 cm^{-1}, which will be used for quantification of assay performance. Other prominent features include the nitro scissoring vibration at 851 cm^{-1}, an aromatic ring mode at 1566 cm^{-1}, and a succinimidyl N-C-O stretch that overlaps with other aromatic ring modes at 1079 cm^{-1}.

Figure 2 also shows that the intensity of the Raman spectra varies proportionally with the concentration of rabbit IgG. This dependence is summarized by a plot of the intensity of $\nu_s(NO_2)$ versus the rabbit IgG concentration to yield one of the two dose-response curves shown in Figure 3. Each data point is the mean intensity of $\nu_s(NO_2)$ measured from five locations on a single sample and the error bars represent the standard deviation in signal. Sample-to-sample variations were less than 10%. As is evident from the spectrum in Figure 2, there is a small but readily detectable signal for the blank resulting from nonspecific binding of the ERLs. Moreover, the response of the blank is slightly less than that for the 1 ng/mL sample, demonstrating the limitation on detection is dictated by nonspecific adsorption. Formally, the limit of detection, which is defined as the concentration which results in a signal equal to that of the blank plus three times its standard deviation, is ~1 ng/mL.

To demonstrate the importance of incubation time on assay performance, an immunoassay for rabbit IgG was performed under static conditions allowing the substrate to incubate with the sample for only 10 min and the ERL solutions for only 10 min. Although not shown, the spectroscopic intensities are much weaker than those obtained for the 12-h incubations. The resulting dose-response curve is also shown in Figure 3. An antigen concentration dependent response is observed, however, compared to the assay with 12-h incubations the sensitivity is markedly decreased. While the signals for specific binding are significantly reduced for short ERL incubation times, importantly, the nonspecific binding also decreases. Thus, there is only a tenfold loss in the limit of detection with the shorter binding times. Other studies (data not shown) have concluded that for these incubation times, equilibration is not reached; these combined data emphasize the importance of incubation time and the need for increasing antigen and label flux to the sample surface.

In an effort to shorten the time required for the immunoassay, the influence of substrate rotation on the antigen binding step was investigated. To test this, an immunoassay was performed in which the capture substrate was rotated at 800 rpm for 10 min in the sample solution. According to Equation 1, these conditions result in a fivefold increase in impingement (1.9×10^{11} IgG/cm^2) compared to that under stagnant binding (3.7×10^{10} IgG/cm^2). Following sample extraction, ERLs were allowed to react with the samples for 12 h in quiet solution. Due to lower ERL concentrations and a smaller value for D, ERL impingement is estimated to be only 1.8×10^9 ERL/cm^2. Based on these calculations, and the fact that equilibrium is approached but not achieved, labeling is the limiting step and it is expected that results will be similar to those of the comparative assay. Thus, any changes in the resulting spectral intensities would be a direct result of an ineffective antigen binding step. The dose-response curve for this assay is shown in Figure 4, along with the results for the control assay (i.e., no rotation). Analysis of the dose-response curves reveals that no significant changes in the intensities occur as a result of substrate rotation during the sample incubation step; thus, rotation-induced flux is an effective means of ERL delivery. This assay also resulted in a detection limit of ~1 ng/mL. Therefore, the time required to detect rabbit IgG can be reduced from ~24 to ~12 h without a loss in the limit of detection simply by implementing rotation to increase antigen flux to the capture surface.

Rotation Studies. Similar studies were performed to investigate the effect of substrate rotation on ERL binding. Two conditions were tested; first, rabbit IgG was allowed to bind to the capture substrate for 12 h without rotation prior to capture substrate rotation at 800 rpm for 10 min in an ERL solution. The second assay utilized substrate rotation (800 rpm, 10 min) to capture the antigen and was followed by rotation (800 rpm, 10 min) in ERLs. It was hypothesized that the results of these assays should be similar since the previous study showed that the signal is dictated by the labeling step. The dose-response curves obtained under these conditions are given in Figure 5, along with a control curve for comparison.

Several important conclusions can be drawn from these experiments. First, as predicted, equivalent dose-response curves can be constructed with substrate rotation in the labeling solution regardless of the manner in which the antigen is bound. This provides further support for the conclusion drawn from the first set of experiments studying the influence of rotation on antigen binding. The second noteworthy observation from Figure 5 is that smaller signals are obtained when ERLs bind under the rotation conditions selected. However, first approximations via Equation 1 estimate the ERL impingement to be three times greater than ERL labeling in quiet solution. Additionally, the nonspecific binding of the ERLs is significantly lower for the assays utilizing rotation to bind the label. In fact, the blank signal due to nonspecific binding diminishes disproportionately to the decrease in specific binding as a result of substrate rotation, and a detection limit of ~1 ng/mL was obtained for these assays as well. The origin of this disproportional binding is speculated to result from additional forces imposed by rotation that remove nonspecifically bound ERLs, and studies are in progress to understand and capitalize on this finding to further lower the levels of detection.

There are several possible origins for the decreased specific ERL binding when rotation is employed. One possibility is that harsher conditions imposed during rotation in the ERLs, compared to stagnant conditions, removes bound antigen from the capture substrate. Another potential reason is that the rotation rate and incubation time under which these ERL incubations were performed are not delivering as many labels to the surface as can be achieved via diffusion for 12 h, contrary to initial projections (i.e., Γ_a in Equation 1 may be lower than predicted). The value for D of the ERL was crudely approximated by the Stokes-Einstein equation[64] in which mass in not a factor and radius is difficult to predict. Additionally, C_b was taken to be that provided by the vendor, but it is qualitatively known that some of the labels are lost during the centrifugation/resuspension cleaning steps, which would serve to lower C_b. Thus, it is probable that D is much smaller than estimated. Collectively, these details explain any discrepancies that yield an overestimation of ERL impingement.

To test the effect of substrate rotation on bound antigen, several capture substrates were prepared and each exposed to 100 ng/mL rabbit IgG (20.0 μL) for 12 h. One substrate was subsequently exposed to 20.0 μL of ERLs for 12 h under stagnant conditions while another was rotated at 800 rpm for 10 min in ERLs to serve as controls. A third substrate was rotated in 2 mM borate buffer (1% BSA, 150 mM) at 800 rpm for 10 min, to mimic rotation in ERLs, and then exposed to 20 μL of ERLs without rotation. Blank studies were also performed under each of these conditions. The resulting SERS signals are shown in Figure 6.

The signal obtained for the capture substrate rotated in buffer prior to labeling with ERLs under static conditions was similar to that for the substrate labeled without rotation. Moreover, the substrate exposed to ERLs with rotation gave a less intense signal. These data suggest that the bound antigen is unaffected by solution flow during a rotation step and another mechanism is responsible for the lower signal observed when labeling is performed with substrate rotation. It is also important to note that the blank signals in these assays are consistent with previous results, and much less nonspecific binding arises as a result of rotation in the labeling solution.

The rotation rate was increased and the incubation time was lengthened to increase the impingement of the ERLs on the substrate in an effort to reach the signals achieved without rotation. Substrates exposed to 100 ng/mL rabbit IgG (20 μL) for 12 h were then incubated with ERLs for 12 h under stagnant conditions, or rotated in an ERL solution for 10 min at 800 rpm, 10 min at 1200 rpm, or 15 min at 800 rpm. Control substrates were exposed to 10 mM PBS in place of the rabbit IgG and then incubated with ERLs under the conditions outlined above. The measured intensities of the symmetric nitro stretch for each substrate are plotted in Figure 7. While this set of experiments was performed with a new batch of antibodies and the signal for the 100 ng/mL control (i.e., stagnant incubation) is lower than that obtained in earlier studies, as is evident, the signal obtained for the 100 ng/mL sample of IgG increases as the rotation rate increases from 800 to 1200 rpm and as the incubation time increases from 10 to 15 min. This discrepancy in signal from earlier studies is attributed to differences in antibody performance.

Detailed analysis of these results supports the hypothesis that lower signals are recorded for ERL labeling with rotation as a result of fewer labels impinging the surface as compared to labeling under stagnant conditions for 12 h. First, rotation-induced flux, and therefore Γ_a, is directly proportional to time while it is only proportional to the square root of rotation rate. Thus, the signal is expected to increase more for a 50% increase in incubation time compared to a 50% increase in rotation rate. This general trend was experimentally followed, however, at 1200 rpm vortexing of the ERL solution resulted from the experimental setup. Therefore, a more detailed quantitative analysis was not possible since the non-laminar flow profile is not accounted for in the rotation-induced flux theory.

Nevertheless, these data support the conclusion that ERL impingement is governed by Equation 1.

This reasoning suggests that it is possible to reach the signal levels achieved without rotation by increasing the impingement of the ERLs on the substrate. Per Equation 1, increases can be realized by further increasing the rotation rate, the incubation time, the ERL concentration, or any combination of these. Evaluation of the blank signal in Figure 7 also shows that the nonspecific binding is still lower than with diffusion as long as labeling is performed with rotation regardless of rotation rate or incubation time. Therefore, the limit of detection could be tremendously improved compared to the control assay while reducing the assay time from ~24 h to ~ 30 min.

An optimized assay was performed by identifying an appropriate rotation rate, incubation time, and ERL concentration and evaluated against a control assay. A rotation rate of 800 rpm was selected to maintain laminar conditions and the incubation time was held at 15 min. Larger signals could be realized with a longer incubation time; however, in light of the overall goal of decreasing the assay time, other means of obtaining signal equivalent to the control assay is preferred. Therefore, the concentration of ERLs was increased from 5.2×10^{10} ERLs/mL, the concentration used in the control assays, to 10.4×10^{10} ERLs/mL in an effort to increase the number of labels impinging the surface-bound antigen. The results of this assay, and those of a control assay, are shown in Figure 8.

There are several noteworthy observations from the two curves. First, at the higher concentrations tested, larger signals are obtained for substrates rotated in the ERL labeling solution. For the assay without rotation in ERLs, fewer labels impinge the surface to tag the bound antigens. Rotation increases the number of ERLs impinging the surface and therefore leads to higher SERS intensities. At the lower range of rabbit IgG concentrations, similar signals are observed for the case of static and convective labeling. Both of these conditions result in excess ERLs impinging the surface and fully labeling the captured antigen. Lastly, less nonspecific binding occurs for the substrates that are rotated in the ERL solution. This results in a detection limit of ~10 ng/mL for the assay without rotation and ~1 ng/mL for the assay performed with rotation. The detection limits were found to vary for each batch of antibody received from the vendor, but this tenfold improvement in detection limit was consistent.

Biological Matrix. Detection of a protein in a PBS matrix is only realistic if the sample has been heavily purified. Ideally, an assay for a protein could be performed directly on a blood serum sample, which contains large levels of nontargeted proteins that may degrade performance because of nonspecific adsorption. Therefore, an assay for rabbit IgG suspended in goat serum was performed in order to mimic a biological matrix. Following the standard assay protocol, sample substrates were exposed to either 20.0 μL of 100 ng/mL rabbit IgG diluted in goat serum or 20.0 μL of blank goat serum for 12 h followed by incubation with 20.0 μL of ERLs (5.2×10^{10} ERLs/mL) for 12 h. For comparison, capture substrates were rotated at 800 rpm for 10 min in the serum-based sample and blank solutions and then rotated at 800 rpm for 15 min in ERLs (10.4×10^{10} ERLs/mL).

The results are presented in Figure 9. Similar signals were obtained for the 100 ng/mL samples diluted in goat serum and for the 100 ng/mL samples diluted in a clean PBS solution. Like the assay in PBS, the signal for the rotated sample is slightly larger than that for the sample statically incubated. The nonspecific binding is again found to be less for the rotated sample, however, the serum blank yields a larger amount of nonspecific binding than the PBS blank, which results in a detection limit for rabbit IgG in a serum matrix of ~10 ng/mL with rotation and ~30 ng/mL without rotation. While preliminary in that more effort could be placed on finding a more effective blocking agent, these data demonstrate that substrate rotation can be successfully applied to real sample matrices for the reduction of assay time and lowering of detection limit.

Conclusions

This is the first report on the combination of rotation-induced flux and SERS readout in a sandwich-type immunoassay format. Systematic studies of the influence of rotation on antigen and label binding led to an optimized immunoassay yielding a tenfold decrease in the limit of detection (i.e., ~10 ng/mL to ~1 ng/mL) and a reduction in the assay time from 24 h to 25 min compared to a static immunoassay. Additionally, rotation-induced flux was effectively applied to samples in a serum matrix. We are beginning further investigation into the mechanism of nonspecific binding. We found that labeling under convective conditions reduces nonspecific binding, the factor responsible for restrictions on the lowest level of detection. Insights into the role of rotation rate, incubation time, and label concentration on nonspecific binding have the potential to significantly improve the limit of detection for all immunoassays.

Acknowledgements

This work was supported through a grant from USDA-NADC and by the Institute for Combinatorial Discovery of Iowa State University. J. D. D. would like to gratefully acknowledge the support of the Mary K. Fassel and Velmer A. Fassel Fellowship. The Ames

Laboratory is operated for the U.S. Department of Energy by Iowa State University under contract W-7405-eng-82.

References

(1) Chomel, B. B. *J. Vet. Med. Educ.* **2003**, *30*, 145-147.

(2) Diamandis, E. P.; Christopoulos, T. K. In *Immunoassay*; Diamandis, E. P., Christopoulos, T. K., Eds.; Academic Press: San Diego, CA, 1996, pp 1-3.

(3) Sokoll, L. J.; Chan, K. W. *Anal. Chem.* **1999**, *71*, 356R-362R.

(4) White, S. R.; Chiu, N. H. L.; Christopoulos, T. K. *Methods* **2000**, *22*, 24-32.

(5) Sheehan, P. E.; Whitman, L. J. *Nano Lett.* **2005**, *5*, 803-807.

(6) Frackelton, A. R.; Weltman, J. K. *J. Immunol.* **1980**, *124*, 2048-2054.

(7) Stenberg, M.; Nygren, H. *J. Theor. Biol.* **1985**, *113*, 589-597.

(8) Stenberg, M.; Stiblert, L.; Nygren, H. *J. Theor. Biol.* **1986**, *120*, 129-140.

(9) Nygren, H.; Werthen, M.; Stenberg, M. *J. Immunol. Meth.* **1987**, *101*, 63-71.

(10) Myszka, D. G.; Morton, T. A.; Doyle, M. L.; Chaiken, I. M. *Biophys. Chem.* **1997**, *64*, 127-137.

(11) Heller, M. J.; Forster, A. H.; Tu, E. *Electrophoresis* **2000**, *21*, 157-164.

(12) Ewalt, K. L.; Haigis, R. W.; Rooney, R.; Ackley, D.; Krihak, M. *Anal. Biochem.* **2001**, *289*, 162-172.

(13) Luxton, R.; Badesha, J.; Kiely, J.; Hawkins, P. *Anal. Chem.* **2004**, *76*, 1715-1719.

(14) Glaser, R. W. *Anal. Biochem.* **1993**, *213*, 152-161.

(15) Johnstone, R. W.; Andrew, S. M.; Hogarth, M. P.; Pietersz, G. A.; McKenzie, I. F. C. *Mol. Immunol.* **1990**, *27*, 327-333.

(16) Opekar, F.; Beran, P. *J. Electroanal. Chem.* **1976**, *69*, 1-105.

(17) Bard, A. J.; Faulkner, L. R. *Electrochemical Methods Fundamentals and Applications*, 2 ed.; John Wiley & Sons: New York, 2001.

(18) Rieger, P. H. *Electrochemistry*, 2 ed.; Chapman & Hall: New York, 1994.

(19) Driskell, J. D.; Kwarta, K. M.; Lipert, R. J.; Porter, M. D.; Vorwald, A.; Neill, J. D.; Ridpath, J. F. *submitted to J. Virol. Meth.* **2006**.

(20) Takano, H.; Kenseth, J. R.; Wong, S.-S.; O'Brien, J. C.; Porter, M. D. *Chem. Rev.* **1999**, *99*, 2845-2890.

(21) Jones, V. W.; Kenseth, J. R.; Porter, M. D.; Mosher, C. L.; Henderson, E. *Anal. Chem.* **1998**, *70*, 1233-1241.

(22) Browning-Kelley, M. E.; Wadu-Mesthrige, K.; Hari, V.; Liu, G. Y. *Langmuir* **1997**, *13*, 343-350.

(23) Dong, Y.; Shannon, C. *Anal. Chem.* **2000**, *72*, 2371-2376.

(24) Nettikadan, S. R.; Johnson, J. C.; Mosher, C.; Henderson, E. *Biochem. Biophys. Res. Comm.* **2003**, *311*, 540-545.

(25) Huet, D.; Gyss, C.; Bourdillon, C. *J. Immunol. Meth.* **1990**, *135*, 33-41.

(26) Wijayawardhana, C. A.; Purushothama, S.; Cousino, M. A.; Halsall, H. B.; Heineman, W. R. *J. Electroanal. Chem.* **1999**, *468*, 2-8.

(27) Salinas, E.; Torriero, A. A. J.; Sanz, M. I.; Battaglini, F.; Raba, J. *Talanta* **2005**, *66*, 92-102.

(28) Messina, G. A.; Torriero, A. A. J.; DeVito, I. E.; Olsina, R. A.; Raba, J. *Anal. Biochem.* **2005**, *337*, 195-202.

(29) Gutcho, S.; Mansbach, L. *Clin. Chem.* **1977**, *23*, 1609-1614.

(30) Donaldson, K. A.; Kramer, M. F.; Lim, D. V. *Biosens. Bioelectron.* **2004**, *20*, 322-327.

(31) Vuori, J.; Rasi, S.; Takala, T.; Vaananen, K. *Clin. Chem.* **1991**, *37*, 2087-2092.

(32) Xu, Y.-Y.; Pettersson, K.; Blomberg, K.; Hemmila, I.; Mikola, H.; Lovgren, T. *Clin. Chem.* **1992**, *38*, 2038-2043.

(33) Brown, C. R.; Higgins, K. W.; Frazer, K.; Schoelz, L. K.; Dyminski, J. W.; Marinkovich, V. A.; Miller, S. P.; Burd, J. F. *Clin. Chem.* **1985**, *31*, 1500-1505.

(34) Hayes, F. J.; Halsall, H. B.; Heineman, W. R. *Anal. Chem.* **1994**, *66*, 1860-1865.

(35) Butler, J. E. *J. Immunoassay* **2000**, *21*, 165-209.

(36) Smith, E. A.; Corn, R. M. *Appl. Spectrosc.* **2003**, *57*, 320A-332A.

(37) Mullett, W. M.; Lai, E. P. C.; Yeung, J. M. *Methods* **2000**, *22*, 77-91.

(38) Lyon, L. A.; Musick, M. D.; Natan, M. J. *Anal. Chem.* **1998**, *70*, 5177-5183.

(39) Nelson, B. P.; Grimsrud, T. E.; Liles, M. R.; Goodman, R. M.; Corn, R. M. *Anal. Chem.* **2001**, *73*, 1-7.

(40) Miyashita, M.; Shimada, T.; Miyagawa, H.; Akamatsu, M. *Anal. Bioanal. Chem.* **2005**, *381*, 667-673.

(41) Gobi, K. V.; Kataoka, C.; Miura, N. *Sensor Actuat B* **2005**, *108*, 784-790.

(42) Rohr, T. E.; Cotton, T.; Fan, N.; Tarcha, P. J. *Anal. Biochem.* **1989**, *182*, 388-398.

(43) Dou, X.; Takama, T.; Yamaguchi, T.; Tamamoto, H.; Ozaki, Y. *Anal. Chem.* **1997**, *69*, 1492-1495.

(44) Ni, J.; Lipert, R. J.; Dawson, B.; Porter, M. D. *Anal. Chem.* **1999**, *71*, 4903-4908.

(45) Grubisha, D. S.; Lipert, R. J.; Park, H.-Y.; Driskell, J.; Porter, M. D. *Anal. Chem.* **2003**, *75*, 5936-5943.

(46) Driskell, J. D.; Kwarta, K. M.; Lipert, R. J.; Porter, M. D.; Neill, J. D.; Ridpath, J. F. *Anal. Chem.* **2005**, *77*, 6147-6154.

(47) Xu, S.; Ji, X.; Xu, W.; Li, X.; Wang, L.; Bai, Y.; Zhao, B.; Ozaki, Y. *Analyst* **2004**, *129*, 63-68.

(48) Mulvaney, S. P.; Musick, M. D.; Keating, C. D.; Natan, M. J. *Langmuir* **2003**, *19*, 4784-4790.

(49) Zhang, X.; Young, M. A.; Lyandres, O.; Duyne, R. P. V. *J. Am. Chem. Soc.* **2005**.

(50) Ansari, D. O.; Stuart, D. A.; Nie, S. *Proc. of SPIE* **2005**, *5699*, 82-90.

(51) Cao, Y. C.; Jin, R.; Mirkin, C. A. *Science* **2002**, *297*, 1536-1540.

(52) Graham, D.; Mallinder, B. J.; Whitcombe, D.; Smith, W. E. *ChemPhysChem* **2001**, *12*, 746-748.

(53) Graham, D.; Mallinder, B. J.; Whitcombe, D.; Watson, N. D.; Smith, W. E. *Anal. Chem.* **2002**, *74*, 1069-1074.

(54) Faulds, K.; Smith, W. E.; Graham, D. *Anal. Chem.* **2004**, *76*, 412-417.

(55) Faulds, K.; Barbagallo, R. P.; Keer, J. T.; Smith, W. E.; Graham, D. *Analyst* **2004**, *129*, 567-568.

(56) Cui, Y.; Ren, B.; Yao, J.-L.; Gu, R.-A.; Tian, Z.-Q. *J. Phys. Chem. B* **2006**, *110*, 4002-4006.

(57) Sun, B.; Xie, W.; Yi, G.; Chen, D.; Zhou, Y.; Cheng, J. *J. Immunol. Meth.* **2001**, *249*, 85-89.

(58) Goldman, E. R.; Balighian, E. D.; Kuno, M. K.; Labrenz, S.; Tran, P. T.; Anderson, G. P.; Mauro, J. M.; Mattoussi, H. *Phys. Stat. Sol. B* **2002**, *229*, 407-414.

(59) Tran, P. T.; Goldman, E. R.; Anderson, G. P.; Mauro, J. M.; Mattoussi, H. *Phys. Stat. Sol. B* **2002,** *229*, 427-432.

(60) Chan, W. C. W.; Nie, S. *Science* **1998,** *281*, 2016-2018.

(61) Llic, B.; Yang, Y.; Craighead, H. G. *Appl. Phys. Lett.* **2004,** *85*, 2604-2606.

(62) Grogan, C.; Raiteri, R.; O'Connor, G. M.; Glynn, T. J.; Cunningham, V.; Kane, M.; Charlton, M.; Leech, D. *Biosens. Bioelectron.* **2002,** *17*, 201-207.

(63) Park, H.-Y.; Lipert, R. J.; Porter, M. D. *Proc. SPIE* 2004; 464-477.

(64) Berry, R. S.; Rice, S. A.; Ross, J. *Physical Chemistry*; John Wiley & Sons: New York, 1980.

(65) This estimation is based on Equation 1 given below.

(66) Kneipp, K.; Kneipp, H.; Itzkan, I.; Dasari, R. R.; Feld, M. S. *J. Phys.: Condens. Matter* **2002,** *14*, R597-R624.

(67) Wagner, P.; Hegner, M.; Kernen, P.; Zaugg, F.; Semenza, G. *Biophys. J.* **1996,** *70*, 2052-2066.

(68) Duhachek, S. D.; Kenseth, J. R.; Casale, G. P.; Small, G. J.; Porter, M. D.; Jankowiak, R. *Anal. Chem.* **2000,** *72*, 3709-3716.

Figure Captions

Figure 1. Schematic of analyte and ERL binding to a rotating capture substrate.

Figure 2. Results from the SERS-based immunoassay detection of rabbit IgG based on a 12-h sample incubation and a 12-h label incubation using stagnant solutions.

Figure 3. Dose-response curves for SERS-based detection of rabbit IgG with 12-h and 10-min incubation times under stagnant conditions for sample binding and ERL labeling. The SERS intensity is that of the $\nu_s(NO_2)$ at 1336 cm^{-1}. The dashed lines represent the lowest detectable signal (blank signal plus 3 times its standard deviation). The inset is the same data set zoomed at lower SERS intensities to showcase the response for the 10-min incubation.

Figure 4. Dose-response curves for the SERS-based detection of rabbit IgG comparing the results for stagnant antigen incubation (12 h) to substrate rotation (800 rpm, 10 min). The substrate was incubated with ERLs for 12 h under static conditions.cThe SERS intensity is that of the $\nu_s(NO_2)$ at 1336 cm^{-1}. The dashed lines represent the lowest detectable signal (blank signal plus 3 times its standard deviation) for each assay.

Figure 5. Dose-response curves for the SERS-based detection of rabbit IgG comparing the results for control conditions (see text), static antigen binding (12 h) with ERL rotation (800 rpm, 10 min), and antigen and ERL rotation (800 rpm, 10 min). The SERS intensity is that of

the $\nu_s(NO_2)$ at 1336 cm^{-1}. The dashed lines represent the lowest detectable signal (blank signal plus 3 times its standard deviation) for each assay.

Figure 6. The effect of rotation on rabbit IgG bound to the capture substrate. All sample incubations were performed under stagnant conditions for 12 h. The SERS intensity is that of the $\nu_s(NO_2)$ at 1336 cm^{-1}.

Figure 7. The effect of rotation rate and incubation time during the ERL labeling step on the SERS signal. All sample incubations were performed under stagnant conditions for 12 h. The SERS intensity is that of the $\nu_s(NO_2)$ at 1336 cm^{-1}.

Figure 8. Dose-response curves for the SERS-based detection of rabbit IgG comparing the results for a control assay requiring 24 h (12-h capture step and 12-h labeling step) to those obtained with optimized rotation (800 rpm) performed in 25 min (10-min capture step and 15-min labeling step). The SERS intensity is that of the $\nu_s(NO_2)$ at 1336 cm^{-1}. The dashed lines represent the lowest detectable signal (blank signal plus 3 times its standard deviation) for each assay.

Figure 9. The SERS intensities obtained for assays of rabbit IgG in a serum matrix. The samples were incubated for 12 h with the sample and ERLs under stagnant conditions or rotated at 800 rpm for 10 min in sample and for 15 min in ERLs. The SERS intensity is that of the $\nu_s(NO_2)$ at 1336 cm^{-1}.

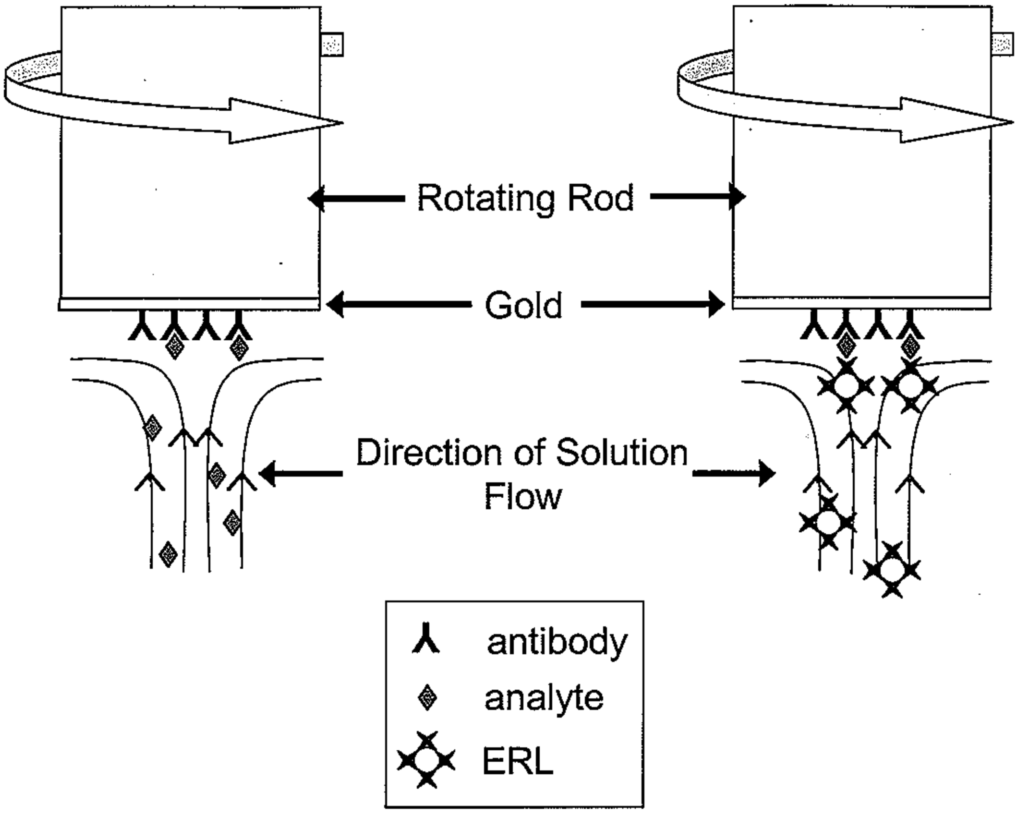
Rotating Rod
Gold
Direction of Solution Flow
antibody
analyte
ERL

Figure 1

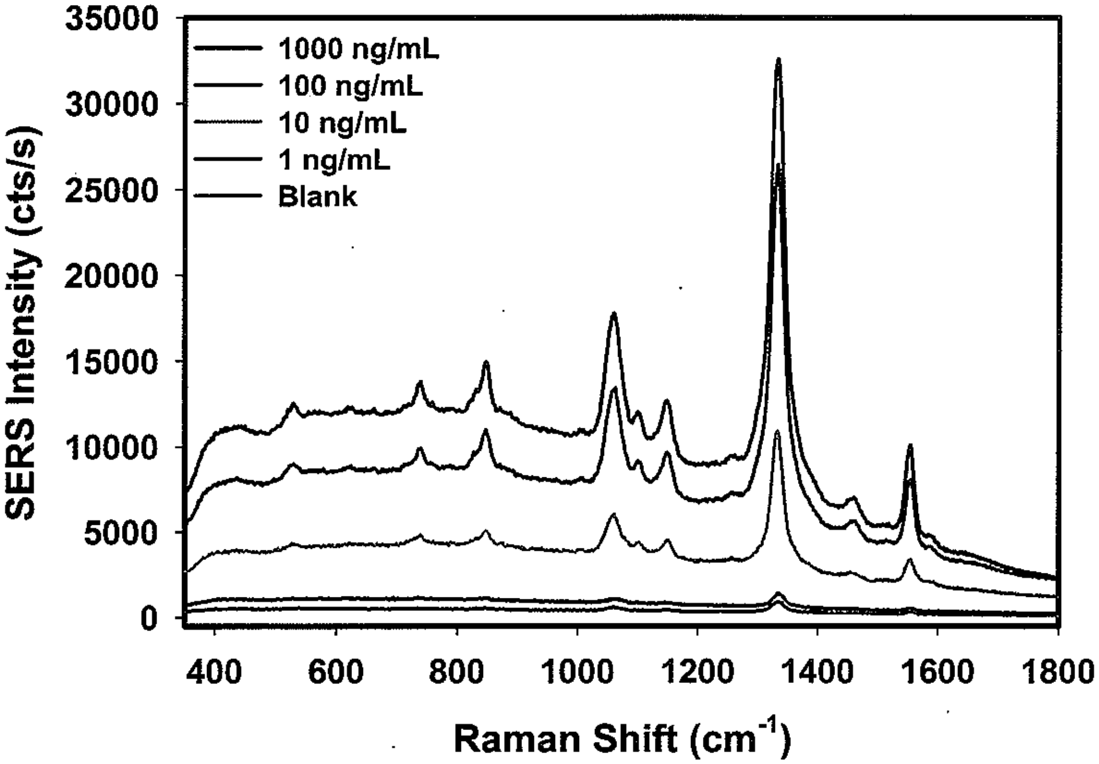
35000
30000
25000
20000
15000
10000
5000
0
SERS Intensity (cts/s)
1000 ng/mL
100 ng/mL
10 ng/mL
1 ng/mL
Blank
400
600
800
1000
1200
1400
1600
1800
Raman Shift (cm-1)

Figure 2

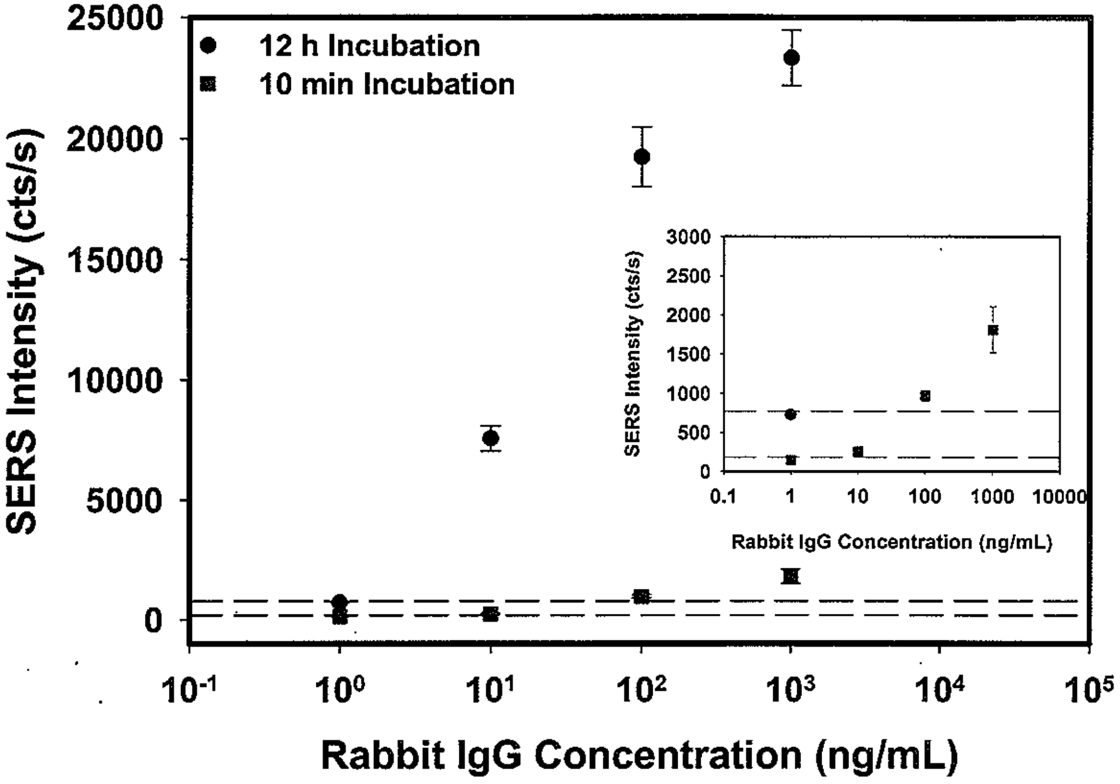
25000
20000
15000
10000
5000
0
SERS Intensity (cts/s)
● 12 h Incubation
▨ 10 min Incubation
10^{-1}
10^{0}
10^{1}
10^{2}
10^{3}
10^{4}
10^{5}
Rabbit IgG Concentration (ng/mL)
3000
2500
2000
1500
1000
500
0
SERS Intensity (cts/s)
0.1
1
10
100
1000
10000
Rabbit IgG Concentration (ng/mL)

Figure 3

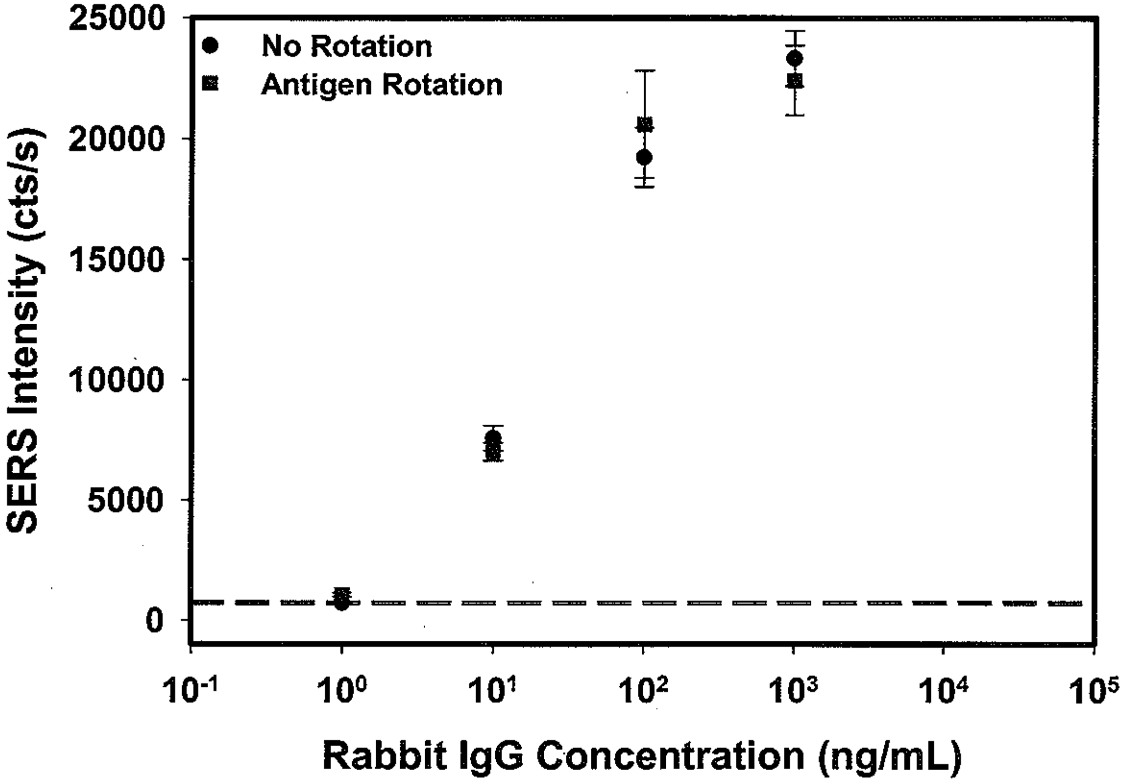

25000
20000
15000
10000
5000
0
SERS Intensity (cts/s)
● No Rotation
■ Antigen Rotation
10^{-1}
10^{0}
10^{1}
10^{2}
10^{3}
10^{4}
10^{5}
Rabbit IgG Concentration (ng/mL)

Figure 4

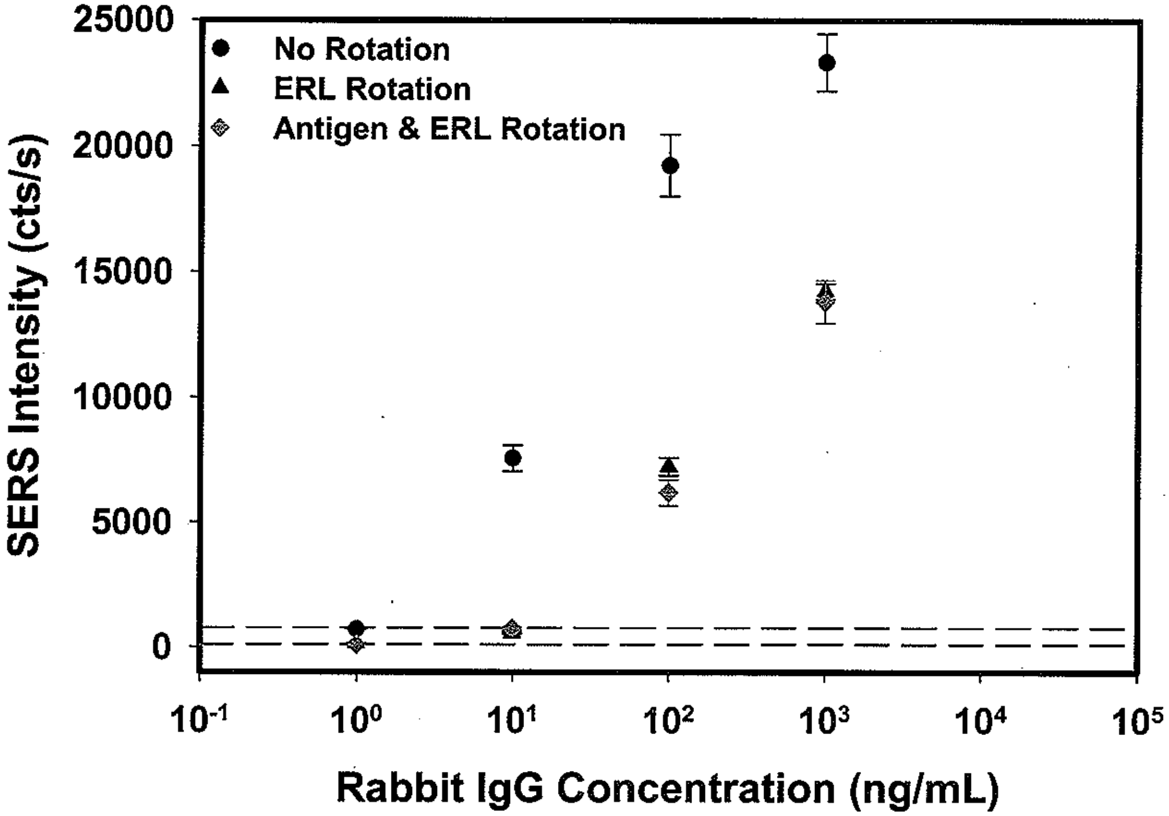
25000
20000
15000
10000
5000
0
SERS Intensity (cts/s)
● No Rotation
▲ ERL Rotation
◈ Antigen & ERL Rotation
10^{-1}
10^{0}
10^{1}
10^{2}
10^{3}
10^{4}
10^{5}
Rabbit IgG Concentration (ng/mL)

Figure 5

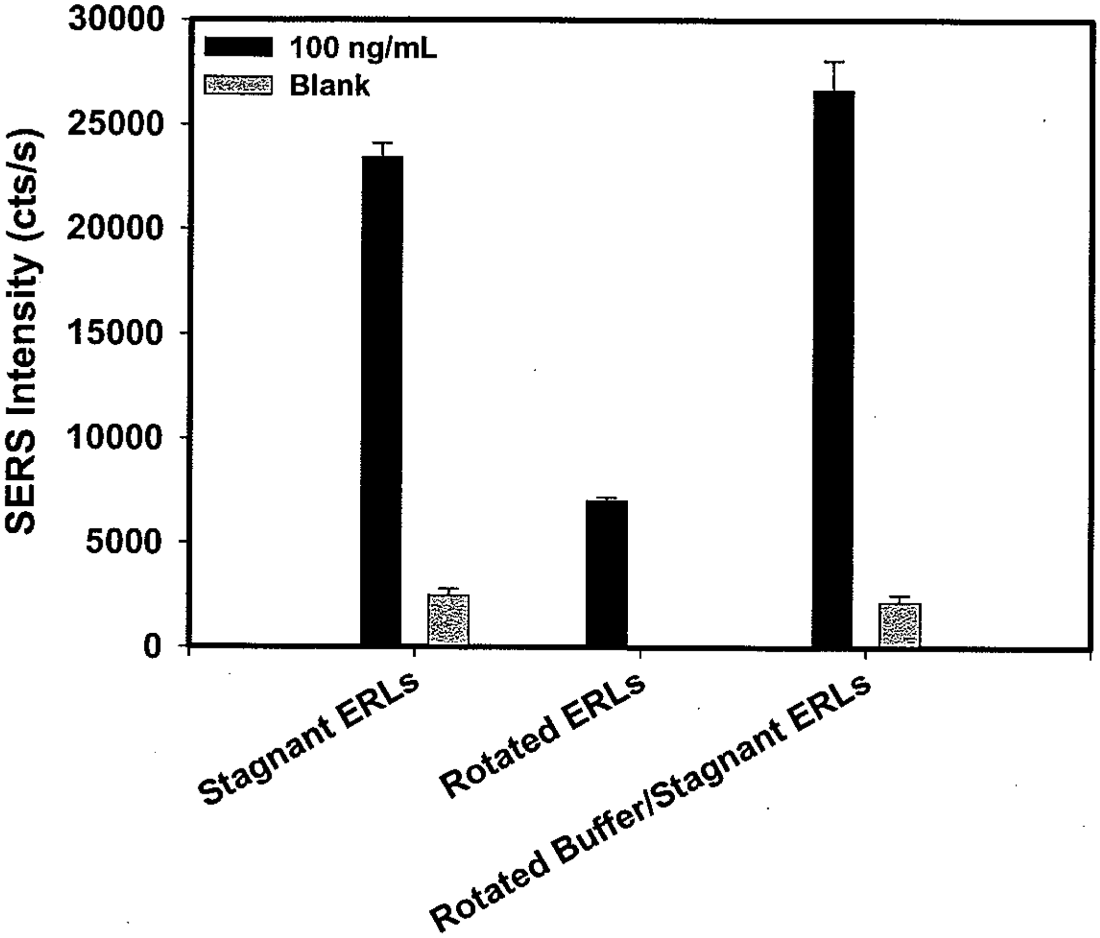

30000
25000
20000
15000
10000
5000
0
SERS Intensity (cts/s)
100 ng/mL
Blank
Stagnant ERLs
Rotated ERLs
Rotated Buffer/Stagnant ERLs

Figure 6

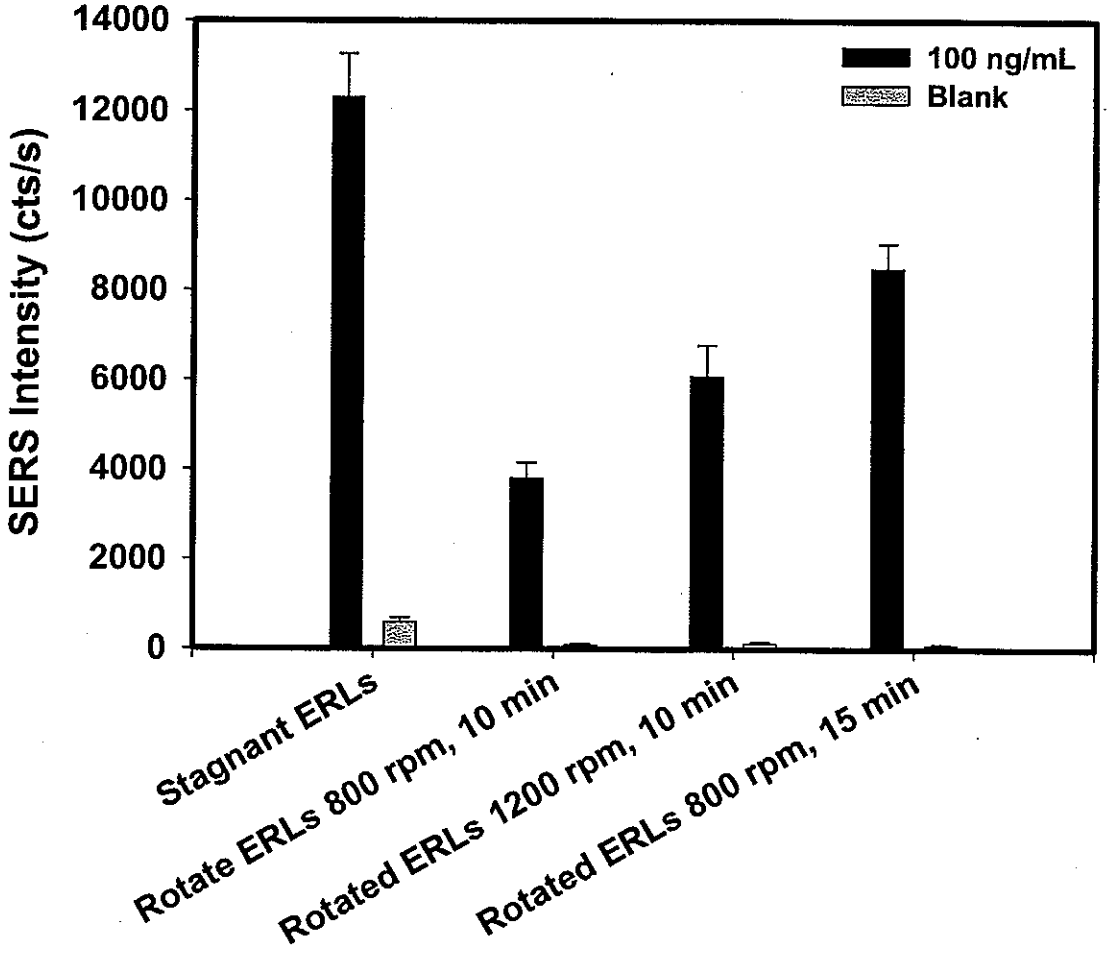

14000
12000
10000
8000
6000
4000
2000
0
SERS Intensity (cts/s)
100 ng/mL
Blank
Stagnant ERLs
Rotate ERLs 800 rpm, 10 min
Rotated ERLs 1200 rpm, 10 min
Rotated ERLs 800 rpm, 15 min

Figure 7

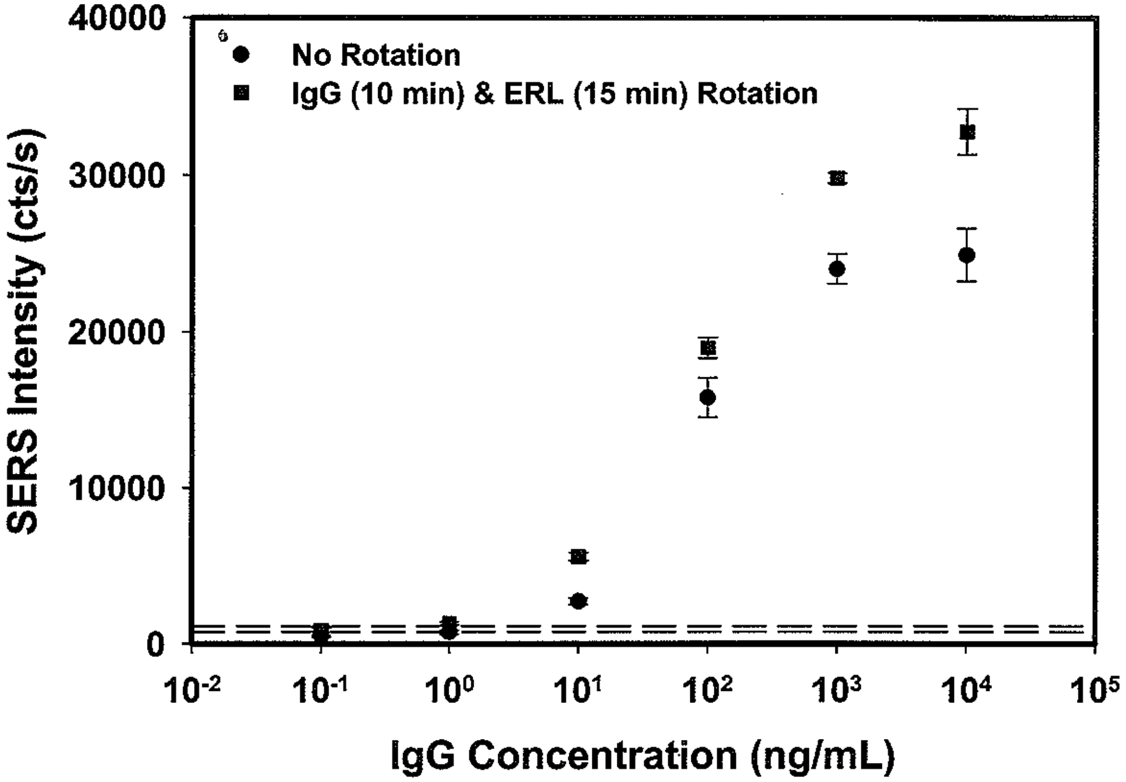

40000
30000
20000
10000
0
SERS Intensity (cts/s)
● No Rotation
■ IgG (10 min) & ERL (15 min) Rotation
10^{-2}
10^{-1}
10^{0}
10^{1}
10^{2}
10^{3}
10^{4}
10^{5}
IgG Concentration (ng/mL)

Figure 8

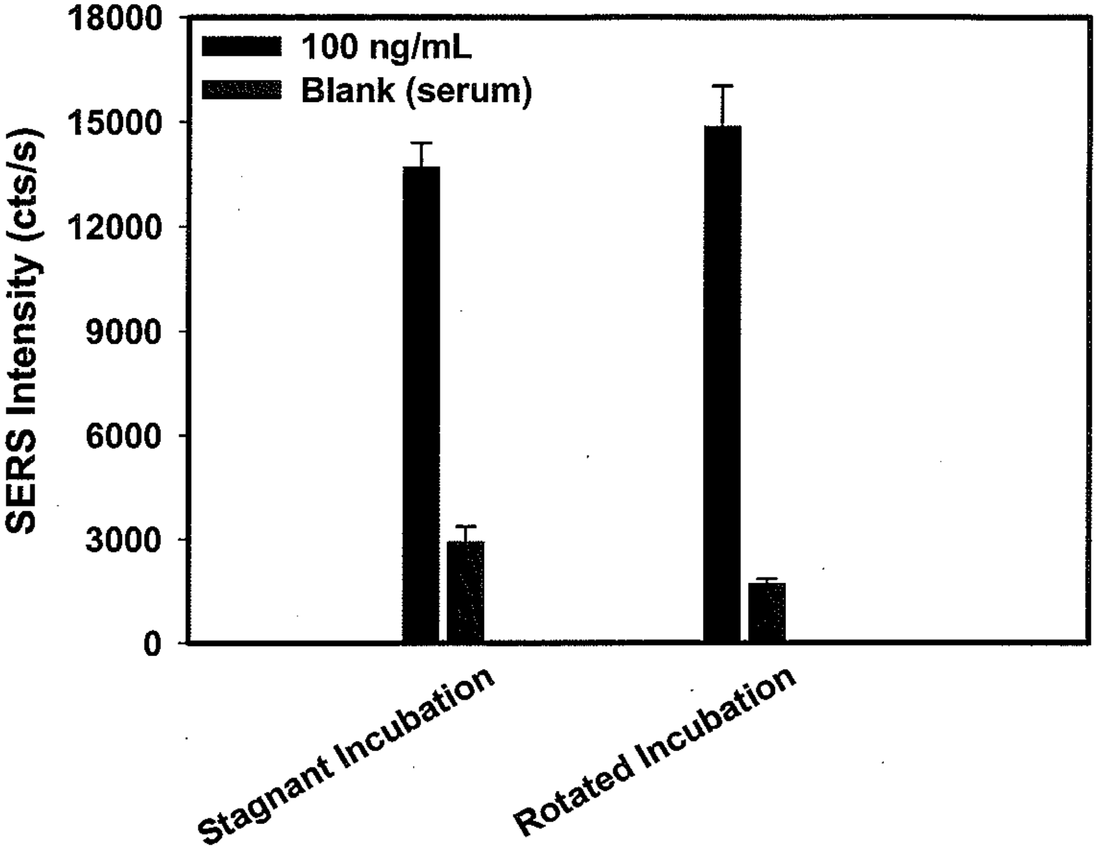
18000
15000
12000
9000
6000
3000
0
SERS Intensity (cts/s)
100 ng/mL
Blank (serum)
Stagnant Incubation
Rotated Incubation

Figure 9

CHAPTER 6: CONCLUSIONS AND PROSPECTS

General Conclusions

The ultimate goal of this dissertation has been to develop a highly sensitive, rapid diagnostic immunoassay relying on SERS for readout. This goal has been achieved through the combined works presented in Chapters 2-5. As part of this effort, Chapter 2 began by modifying a SERS-based immunoassay strategy previously developed within our group such that the assay protocol could be universally applied for the detection of many analytes. This detection scheme employed extrinsic Raman labels (ERLs) for the identification and quantification of analyte bound to an antibody-modified gold substrate. Chapter 2 reported the first demonstration of low level detection of an intact viral pathogen in a sandwich immunoassay format based on a SERS readout method. As a consequence of detailed investigations regarding solution pH, ionic strength, blocking buffers, and surfactants, this method resulted in a limit of detection of 10^6 $TCID_{50}$/mL, and is therefore competitive with other viral assay methods, such as fluorescence and microcantilevers, which have limits between 10^5 and 10^8 $TCID_{50}$/mL. This detection limit can be further conceived as the detection of only ~70 feline caliciviruses when considering the sample area interrogated by the laser spot. While respectable, lower detection levels are always desirable, and as presented in Chapter 1, it is possible to improve the sensitivity of this method by increasing the signal of the ERL or decreasing the nonspecific binding. Moreover, the incubation time for sampling and labeling required ~24 h while the readout was performed in 1 s. Thus, it was determined from Chapter 2 that efforts should be placed on reducing the incubation time in addition to improving the label intensity. These conclusions were the motivation for the investigation into the surface enhancement mechanism and the search for a methodology to reduce the assay time presented in Chapters 3-5.

In an effort to fully exploit the potential of SERS as a sensitive readout technique, experiments were carried out to further examine details related to the enhancement mechanism with respect to the possible plasmon coupling of the ERLs with the underlying gold substrate. The results of these studies were presented in Chapter 3. This paper found that the absorption peak undergoes a red shift as the nanoparticle size increases and the nanoparticle-substrate separation distance decreases. Furthermore, a red shift was discovered for nanoparticles of the same size immobilized on a gold substrate compared to a silver substrate. This study also found that the greatest SERS enhancement factor occurs for a substrate prepared with an SPR peak between the excitation and scattered wavelength, at ~660 nm. Thus, the SERS intensity can be optimized by varying the nanoparticle size, gap, and substrate material. This set of data is the first experimental evidence for the dependence of the SERS enhancement factor on the nanoparticle-substrate separation distance and the most convincing argument yet in support of theoretical prediction that the maximum enhancement occurs when $\lambda_{SPR} = (\lambda_{excitation} + \lambda_{scattering})/2$. These results lay the foundation necessary to design an optimized assay with the potential to measure SERS from a single ERL in our SERS-based immunoassay.

Chapter 4 explored the use of substrate rotation to increase antigen flux to the capture surface in a solid phase immunoassay. Initial investigations into rotation-induced flux utilized atomic force microscopy (AFM) for the label-free detection of porcine parvovirus (PPV) which isolates a single binding step for full characterization of the flux. The flux of the antigen was systematically controlled via rotation rate and incubation time and resulted in a standardless method for quantification utilizing well-established hydrodynamic flow theory. The developed theory was used to predict and design optimized immunoassays which led to an improvement in the analytical performance of the AFM-based immunoassay as well as a decrease in incubation times.

The technology developed in Chapter 4 for decreasing the binding time of the antigen binding step was extended in Chapter 5 to the labeling step for the SERS-based format. Systematic studies of the influence of rotation on antigen and label binding led to an optimized immunoassay yielding a tenfold decrease in the limit of detection (i.e., ~10 ng/mL to ~1 ng/mL) and a reduction in the assay time from 24 h to 25 min compared to a static immunoassay. The sensitivity of SERS-based readout, coupled with the short incubation times achieved with rotation, promises great potential for playing a significant role in the bioanalytical arena.

Prospects

There are several fundamental and practical challenges that must be addressed concerning the union of SERS detection and substrate rotation in order to increase the likelihood of receiving widespread attention. Even with the decreased assay time, throughput is limited by the current experimental setup since samples must be rotated serially. There are three approaches capable of realizing increased throughput. First, an array of rotating rods could be machined to have individual capture substrates in separate sample solutions. However, this would require bulky instrumentation and multiple sample solutions. Second, a capture substrate could be fabricated to contain an array of many antibodies for various target pathogens. This second approach, requiring a single sample solution and simple instrumentation, is more appealing, but presents challenges associated with preparing an array of compositionally unique elements. Nevertheless, experiments are underway to develop facile preparative techniques in order to apply substrate rotation to a multiplexed capture substrate. A more intriguing approach to increase throughput would be to take advantage of the narrow Raman band widths to facilitate simultaneous detection of multiple analytes without the hassle of capture substrate addressing. Presently, knowledge of unique labels is limited, however, and much more attention must be given to label identification. Regardless of which avenue leads to a successful multiplexed assay, coupled with the reduced assay times via substrate rotation, clinical sample throughput would greatly benefit from this exciting new technology.

One of the most stimulating insights into the mechanism of SERS enhancement presented in Chapter 3 was the discovery of an enhancement dependence on nanoparticle-substrate separation distance. It was concluded that larger enhancement factors are obtained as the gap distance is minimized. This finding has rather profound implications on substrate design and suggests the potential for increased signals. With the current design, the ERL is separated from the gold capture substrate by two antibodies, the analyte, and two organic monolayers. It is possible that replacing antibodies with much smaller biorecognition elements, such as aptamers, much larger signals could be realized. The findings from Chapter 3 also illustrate the need to consider the analyte size. Detection of larger analytes may benefit from the use of larger ERLs to maintain the optimum SPR due to an increased nanoparticle-substrate gap distance.

It is arguably more important to concentrate research efforts on decreasing the signal due to nonspecific binding than to raise the Raman signal with optimized surface enhancement. Currently the limit of detection in the SERS-based assay is dictated by the level of nonspecific binding. In Chapter 5 it was found that labeling under convective conditions reduces nonspecific binding. Further investigation into the role of rotation rate, incubation time, and label concentration on nonspecific binding are currently being pursed in our laboratory. These insights into the mechanism of nonspecific binding are not only valid for the SERS-based assay utilized throughout this dissertation, but have the potential to significantly improve the limit of detection for all sandwich-type immunoassays.